UNIVERSITÀ DEGLI STUDI DI PALERMO

Dottorato in Scienze della Terra e del Mare.
Dipartimento di Scienze della Terra e del Mare.
Settore Scientifico Disciplinare GEO/08

UV camera-based monitoring SO_2 flux of Mt. Etna

IL DOTTORE
Roberto D'Aleo

IL COORDINATORE
Prof Alessandro Aiuppa

IL TUTOR
Prof Alessandro Aiuppa

CICLO XXX
ANNO CONSEGUIMENTO TITOLO 2018

TABLE OF CONTENT

Abstract

The study of volcanic gas fluxes provides important information on magma dynamic inside a volcano. Measurements of volcanic gas emission rates, focused on SO_2, have started in the 1970s. Earlier remote sensing techniques, including the Correlation Spectrometry (COSPEC) and Differential Optical Absorption Spectroscopy (DOAS), have revolutionized our ability to measure volcanic gases, and have allowed retrieving the first accurate SO_2 flux time-series. These methods, however, have limited temporal and spatial resolution.

The advent of the UV camera technique has resulted in a major improvement of the temporal and spatial resolution of the volcanic gas flux datasets, promising a major advance in gas-based volcano monitoring. This methodology allows to measure SO_2 fluxes with a temporal resolution of ~1Hz, and thus to compare gas observations with geophysical parameters, filling the gap between these two branches of volcano science. The much improved temporal resolution of UV cameras allows to capture transient (tens of seconds) volcanic gas-driven phenomena, such as Strombolian explosions, and allows to monitor and eventually predict transition from quiescence to eruption.

In this PhD dissertation, I present SO_2 flux data collected with a permanent network of UV cameras deployed on Etna volcano. The presented results were obtained between 2014 and 2016, during which Etna experience a variety of eruptive activity styles. These allow us to study the ability of the camera network to characterize, and possibly anticipate, changes in the volcano's degassing behaviour from quiescence to eruption.

The 2014 SO_2 flux results are used to explore interconnections in the shallow plumbing system of Etna summit crater. Observations were carried out in summer 2014, a period encompassing two eruptive episodes of the New South East Crater (NSEC), and a fissure-fed eruption in the upper Valle del Bove. I demonstrate that vent-resolved SO_2 flux time-series can allow capturing shifts in activity from one vent to another, and contribute to our understanding of the Etna's shallow plumbing system structure. Results show that the fissural eruption contributed ~50,000 tons of SO_2, or ~30 % of the SO_2 emitted by the volcano during the eruptive interval (July 5th-August10th). Activity from this eruptive vent gradually vanished on August 10th, marking switch of degassing toward the NSEC. Onset

of degassing at the NSEC was precursory to explosive paroxysmal activity on August 11-15.

The 2015 SO_2 flux results are used to characterise a particularly violent paroxysmal sequence that took place at Etna on December, intermittently involving four of its summit craters, especially the Voragine (VOR) that had previously displayed no activity for several years. I characterize the volcano's degassing behaviour prior to, during and after this paroxysmal sequence, using a multidisciplinary approach that combines gas (SO_2: UV-Camera and OMI) and thermal (thermal cameras and MODIS) observations from both ground and space. I make use of the high spatial resolution of UV-cameras to resolve SO_2 emissions from the erupting VOR crater for the first time, and to characterize temporal switches in degassing activity from VOR to nearby craters, including the New Southeast Crater (NSEC). I demonstrate that on December 1, two days before the first paroxysm, degassing activity concentrated at VOR, whose SO_2 flux increased sizably, from 10 kg/s (end of November) up to 45.5 kg/s. Onset of paroxysmal activity at VOR on December 3-5 was marked by VOR SO_2 fluxes peaking at 54-103 kg/s, by a visible increase in satellite-derived thermal emissions (2000 MW vs. ~2-11 MW July-November 2015 average), and by a OMI-derived daily SO_2 mass release of 5400-10000 tons (500 tons average in the pre-eruptive period). A switch in volcanic activity from VOR to NSEC on December 6 was detected by increasing SO_2 fluxes at the latter crater (up to 40 kg/s), and by an exponential decay of SO_2 emissions from VOR. Taken together, observations allow to fully characterize the degassing (SO_2) budget for the entire paroxysmal sequence.

In 2016, Etna undertook a complex and time-variable eruptive sequence. A paroxysmal lava fountain sequence occurred at VOR in May, followed by mild strombolian activity during the summer and caldera-floor subsidence since September. These events were carefully monitored using the UV camera network. Based on these results, I propose that the rate of magma ascent and decompression modulate the rate of SO_2 flux variations, and our ability to capture a precursory gas variation prior to eruption. I find that rapid magma decompression prior to a lava fountain is associated with rapid) SO_2 flux variations occurring within timescales of a few hours, and thus difficult to detect/predict using the camera network. In contrast, slow moving magmas (leading to efficient gas-melt separation and resulting into more moderate strombolian explosions) are associated with precursory SO_2 variations more easily captured in the weeks prior to eruption onset.

In the last Chapter of this dissertation, I demonstrate the advantage of UV cameras, used in tandem with other instrumental techniques, in quantifying the flux of other volcanic gas

species than SO_2. More specifically, I used the UV camera to measure plume speed with high precision, which in combination with a Dial-Lidar allowed quantifying the volcanic CO_2 flux from Etna remotely (4 km distance) for the first time. Volcanic eruptions are often preceded by precursory increases in the volcanic carbon dioxide (CO_2) flux. Unfortunately, traditional techniques used to measure volcanic CO_2 require near-vent, in situ plume measurements that are potentially hazardous for operators and expose instruments to extreme conditions. To overcome these limitations, the project BRIDGE (BRIDging the gap between Gas Emissions and geophysical observations at active volcanoes) received funding from the European Research Council, with the objective to develop a new generation of volcanic gas sensing instruments, including a novel DIAL-Lidar (Differential Absorption Light Detection and Ranging) for remote (e.g., distal) CO_2 observations. In Chapter 7, I report on the results of a field campaign carried out at Mt. Etna from 28 July 2016 to 1 August 2016, during which I used the UV camera in tandem with this novel DIAL-Lidar that retrieved spatially and temporally resolved profiles of excess CO_2 concentrations inside the volcanic plume. By vertically scanning the volcanic plume at different elevation angles and distances, an excess CO_2 concentration of tens of ppm (up to 30% above the atmospheric background of 400 ppm) was resolved from up to a 4 km distance from the plume itself. From this, and using the camera-based plume speed records, the first remotely sensed volcanic CO_2 flux estimation from Etna's northeast crater was derived at ≈2850–3900 tons/day. This Lidar-based CO_2 flux is in fair agreement with that (≈2750 tons/day) obtained using conventional techniques requiring the in situ measurement of volcanic gas composition.

In summary, the results presented here confirm the versatility and utility of UV cameras in volcano monitoring, and for better understanding degassing dynamics at open-vent volcanoes.

Chapter 1
Introduction

Volcanic gas composition and fluxes can provide important information on magma dynamics inside a volcano, and can therefore provide key information to understand the transition from quiescence to eruptive activity. The solubility of gas in a magma is strongly correlated, among other factors, by pressure (Oppenheimer et al., 2014) and hence on depth of magma storage. During magma ascent and decompression, the solubility of volatiles decrease, leading to gas exsolution. Modelling (Moretti and Papale 2004) and petrological (Métrich el., 2010) show, in particular, that SO_2 exsolution from a rising magma batch starts at pressure of <100MPa, that corresponds at a depth of ~ <3 km.

The most evident expression of magma degassing into the atmosphere is the volcanic plume, an air-dominated heterogeneous system containing volcanogenic gases, aerosols and ash particles (Oppenheimer, 2003). At open-vent volcanoes, the plume accounts for the majority of the energy and mass daily output during quiescent activity (Allard, 1997).

Several studies (e.g., Caltabiano et al., 2004; Galle et al., 2003; Edmond et al., 2003) linked SO_2 flux variation to volcanic activity, showing that an increase in the SO_2 flux output often precedes, from days to months, volcanic eruptions. This behaviour has led the SO_2 flux to be used as important parameter in volcano monitoring (Wallace 2001). Studies have been largely focused on sulphur dioxide because this gas is relatively straightforward to remotely sense in volcanic plumes, due to its strong UV absorption bands and low ambient concentrations (McGonigle et al., 2017). Remote sensing techniques have increasingly been used over the last decades in volcanic SO_2 plume measurement, significantly broadening the ability of volcanic gas geochemistry to contribute to volcanic hazard assessment (Oppenheimer, 2010). For instance, spectroscopic-sensing of volcanic SO_2 effectively contributed to identifying Pinatubo's re-awakening in 1991 (Daag et al. 1996; Hoff 1992).

This PhD is focused on the study of the SO_2 degassing behaviour of Mt. Etna, a basaltic volcano in southern Italy (Bonaccorso et al., 2004), and one of the most active (Allard 1991) and well monitored volcano in the world. Mt. Etna volcano contributes time-averaged SO_2 flux emissions of 2 Mt/a corresponding to about 10-15% of global volcanogenic budgets.

The SO_2 flux brings important information on how the volcano works, helping to understand the shallow magma dynamics and its use for volcano monitoring (Allard et al., 2006).

Since the 1970s, COSPEC (Moffat and Millan, 1971; Stoiber et al., 1983; William-Jones et al., 2000) and more recently DOAS (McGonigle, 2007) have been the most widely used techniques for ground-based SO_2 flux monitoring. These are applied by scanning across the plume cross section (McGonigle et al., 2003), or traversing beneath the plume with a vehicle, boat, aircraft, or an unmanned aerial vehicle (McGonigle et al., 2008). Today, the scanning DOAS technique is widespread in numerous volcano observatory worldwide to retrieve SO_2 flux time series (Hidalgo et al. 2015) - due to its technical features, it is used as technique for permanent monitoring of gas flux (Salerno et al., 2009; Galle et al., 2010). Notwithstanding its benefits, the DOAS technique is limited by relatively low temporal resolution, since a scan or traverse requires several minutes to be accomplished, hampering measurement of impulsive gas release processes, such as explosions, and resolving transition from quiescence to eruptive activity. The DOAS-derived fluxes also have limited spatial resolution that do not allow resolving closely spaced gas emissions sources (e.g., simultaneously degassing vents).

The advent of the UV camera technique (Mori and Burton 2009) has brought a new tool to study fast occurring degassing process, such as puffing and Strombolian explosions (Tamburello et al., 2012). These require high time and spatial resolution to be studied. The UV Camera technique allows to measure volcanic SO_2 fluxes at a sampling rate of ~1Hz, and to compare gas data with geophysical datasets, such as seismic tremor, VLP and infrasound. Moreover, it is possible to retrieve from the same images the plume gas velocity. Taking advantage on these UV camera features, it is also possible to use in combination with other instrument, such as Multi component GAS analyser (MultiGas), in order retrieve gas fluxes for other species CO_2 flux at high temporal resolution.

In this PhD dissertation, I report on SO_2 flux collected with one of the first permanent network of UV cameras installed on an active volcano. This network has been realised in the context of the Europe Research Council-funded project Bridge (www.bridge.unipa.it). I discuss three years of data collected from 2014 to 2016, a period during which several eruptions occurred, characterized by different eruptive styles. This helps studying the Etna's degassing behaviour in different volcano contexts, and testing the permanent UV camera network for monitoring the volcano's activity. After introducing background on methodology and study area in Chapters 2 and 3, I summarise separately the dataset acquired in the three measurement years.

The 2014 results, which are detailed in Chapter 4, demonstrate that high-rate UV camera-based SO_2 flux data, in combination with geophysical signals, pave the way to measuring rapid activity switches from one vent to another, e.g., between the Northeast crater, the New Southeast craters and effusive vents in the Upper Valle del Bove scar. These results bring implications for the shallow structure of the plumbing system, supporting the idea that different vents share a single magma source and are interconnected at shallow depth.

In 2015, the UV camera results (discussed in Chapter 5) allowed characterising for the first time the degassing budget of a paroxysmal sequence from Voragine crater time, including calculation of the volume of the gas output and of the degassing magma volume producing the eruption. Inter-comparison with independent data shows that, during the eruption, more magma was erupted than contained by the degassed SO_2, suggesting that the paroxysms were fed by interaction between degassed, shallowly stored magma in the conduit and rapidly ascending new (volatile-rich) magma.

In 2016, a variety of eruptive styles was observed, from a paroxysmal lava fountain at Voragine crater in May, and a Strombolian sequence in August. Our data (Chapter 6) show contrasting SO_2 degassing behaviour between the two periods. It is concluded that rapid magma decompression prior to a lava fountain is associated with rapid SO_2 flux variations within timescales of hours prior/during the vent, while slow magma ascent (leading to gas-melt separation and then strombolian explosions) are associated with precursory SO_2 variations more easily captured weeks prior to eruption onset.

The results presented here confirm the value of permanent SO_2 camera networks for interpreting, and possibly predicting, volcano behaviour. UV cameras are a new tool in the armoury of volcanologist, and permanent camera networks should be installed in as many volcanoes as possible in the near future to assist volcanic hazard assessment in nearly real-time.

Chapter 2
Methods

The SO_2 flux dataset I report on in this PhD dissertation derives from a network of two stand-alone SO_2 camera systems, recently deployed on the flanks of Mt. Etna volcano within the context of the FP7-ERC-funded Project *BRIDGE* (http://www.bridge.unipa.it/).

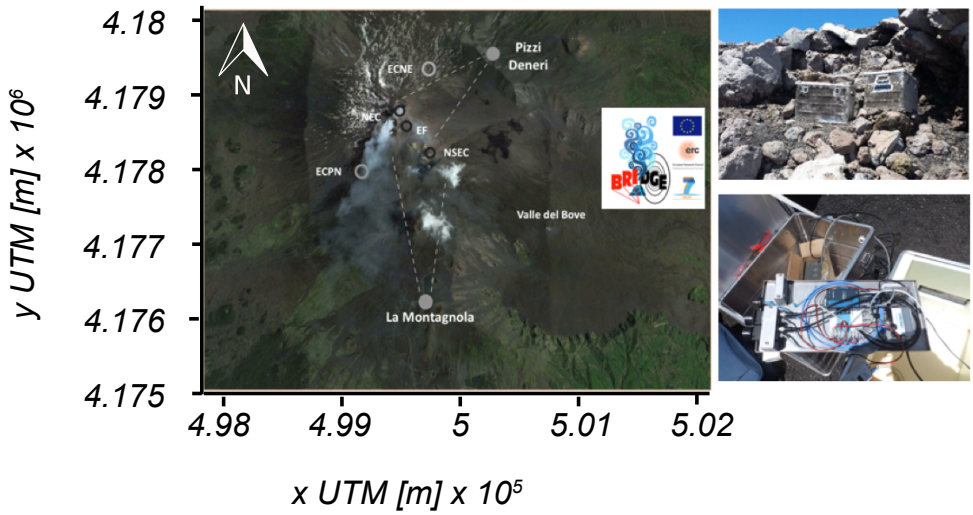

Figure 1 map and field of view of the bridge uv network stations. On the right an example of uv4 station, located at pizzi deneri

These permanent, fully autonomous SO_2 cameras were installed at La Montagnola (UV3), 3.5 km from the New South East Crater (NSEC), and at Pizzi Deneri (UV4), 2 km from the North East Crater (NEC) (Fig. 1). The UV3 SO_2 camera system is designed to separately resolve degassing activity from the NSE and the Central Craters (CCs), while UV4 can also fully capture degassing from the NEC (Fig. 1). Both UV systems are based on the dual UV camera principle, as I detail in the following section. UV3 runs 5 hours each day in a laboratory hut operate by INGV-OE, while UV4 is powered by batteries and runs 5 hours a day during the summer period only.

2.1 The dual UV camera technique: hardware

A dual UV camera system employs two digital cameras, each of model JAI CM 140 GR, with 10-bit digitization and 1392×1040 pixels. These cameras mount CCD sensors sensible to UV light. The cameras are equipped with Uka Optics quartz lenses with a focal lens of 9-12 mm, and a field of view of 37° to 45°. These quartz lenses do not affect the investigated wavelength, the focus is manual and the iris ranges from 2.8-16. An Edmund Optics pass-

band filter (cantered at either 310 nm or 330 nm) is placed between each lens and camera couple (see below).

The camera operates on the principle of contrasting the brightness of the pixels in the presence/absence of SO_2 absorption when measuring back-scattered sunlight (skylight). This is achieved using two Edmund Optics pass-band filters placed between the lenses and the CCD of the two simultaneously operating cameras. The use of the two filter method, with simultaneous image acquisition from two cameras, allows compensating for aerosol attenuation/backscattering, while minimizing any temporal mismatch associated with filter changes on a single camera system (Mori and Burton, 2006; Bluth et al., 2006). It also allows increasing sampling rate up to 2 synchronous images every 2 seconds taken from two cameras (Kantzas et al. 2010).

In the dual camera system, a first filter, named as α of 310 nm, transmits wavelengths strongly affected by the presence of SO_2. The second filter, β or 330 nm, mounted on the second co-aligned camera, transmits wavelengths that are not absorbed by SO_2. Sulphur dioxide absorption ends at ~320 nm (Vandaele et al., 1994) (fig. 2), and filters α and β operate in the range 300-320 nm and 320-340 nm respectively. A qualitative measure of absorbance A can therefore be obtained per camera pixel, following eq. 1:

$$A = -\log_{10}\left[\frac{\left(\frac{IP_{310}}{IB_{310}}\right)}{\left(\frac{IP_{330}}{IB_{330}}\right)}\right] - A_0 \quad \text{(eq. 1)}$$

where A is the absorbance, I^{310} and I^{330} are the pixel intensities associated with cameras mounting the 310 or 330 nm filter, while A_0 is the absorbance level associated with clear background sky sub-area of the image that is assumed to be unaffected by SO_2 absorption.

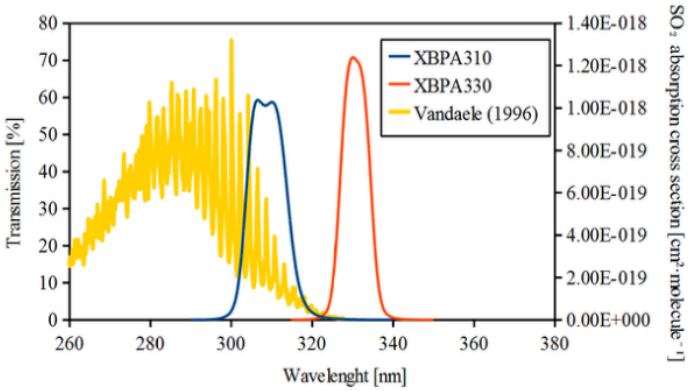

Figure 2 Vandaele SO_2 cross section and the two pass-band filter range

Absorbance (eq. 1) is then converted in SO_2 column density integrating data from a co-located ultraviolet spectrometer, which is pointing to a known sub-area within the camera

field of view. This allows us to obtain in real-time the proportionality ratio (slope and intercept of the calibration curve) between absorbance and SO_2 column densities using the method described in Lubcke et al. (2013).

The use of the UV spectrometer allows to quantitatively measuring the full UV spectrum discriminating the different bandwidth contributions. This allows us to fit the theoretical SO_2 absorption cross-section (Vandaele et al., 1994) with the differential absorption between two consecutive spectra, which were acquired every 5 seconds. The Ocean-Optic USB2000+ Spectrometer in use has a Sony ILX511B Linear Silicon CCD Array Detector at 2048 pixels on-board, with a Wavelength Response of 200-1100 nm and a dynamic range of 8.5 x 108 and a SNR of 250:1 at full signal. Calibrated SO_2 column densities over the entire images are then obtained by integrating images achieved by the UV-camera with information achieved by the spectrometer.

The acquisition/processing module consists in an integrated data-logging and image processing system which was specifically designed to automatically gather synchronous data from instrument module. We designed the acquisition/processing module for monitoring applications where either a Fujitsu Server Primergy RX100 S8 rack computer (UV3) or a Jetway N2600 embedded pc (UV4) is connected to the instrument module, acquires and process data automatically without the need of the operator. To do this we designed algorithms to control acquisition and processing parameters, such as the automatic tuning of the exposure associated with UV cameras and spectrometer and automatic evaluation of optimal viewing condition. Computer internal time drift is controlled by a specifically designed application that reads the time-stamp from a NMEA standard message coming from a GPS antenna. The instrument module communicates with acquisition/processing module via wired or wireless TCP/IP connection. Once a raw image is acquired, it is read by the system to check the presence of any saturated or under-exposed pixels, in order to automatically tune the camera's exposure time accordingly. An automatic real time tuning of exposure time is applied to UV spectrometer data in order to have the best measurement dynamics within the UV bandwidth.

The final derived SO_2 column density image is used for obtaining a profile orthogonal to the plume direction. The integrated profile (integrated column amount or ICA) is then multiplied by the plume transport speed to calculate a SO_2 flux.

2.2 Data processing with Vulcamera

The two co-aligned cameras capture sequential image of the Etna volcano's plume, with an acquisition rate of ~1 Hz and are able to resolve up to ~5 m. The collected data were initially post-processed using the Vulcamera software (Tamburello et al., 2011), following the methodology of Kantzas et al. [2010]. Later, a set of scripts was developed in order to automate the image processing, as detailed in section 3.3.

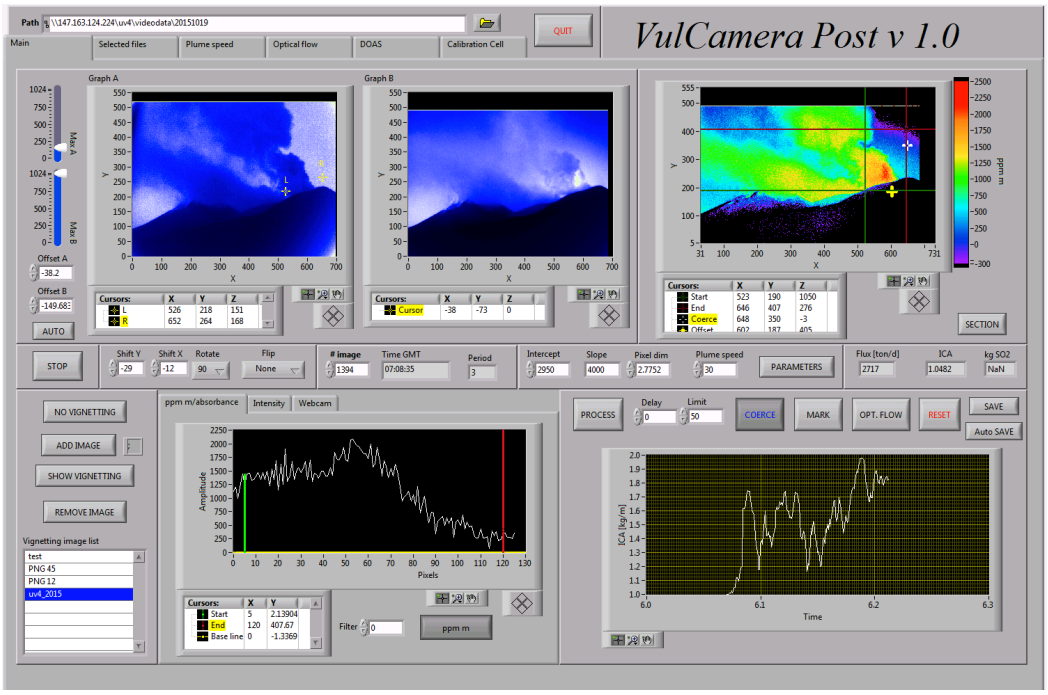

Figure 3 The main frame of Vulcamera Software. On the top are displayed the two pass-band filtered uv images and the absorbance images. On the bottom there are the ICA time series graph, on the right, and the pixel vs amplitude graph on the left

Vulcamera is a stand-alone software with a user-friendly user interface for performing exploratory analysis on UV image dataset. The main panel of Vulcamera (Figure 3) displays the raw 310 and 330 nm filtered images in blue color scale, called "Graph A" and "Graph B" respectively. A SO_2 column density (SCD) image is simultaneously calculated and displayed using the entered intercept and slope parameters. A SCD profile is obtained by selecting its initial and final positions in the "Graph A".

The Integrated Column Amount (ICA) is calculated from the bottom left graph by integrating the white curve within the green, red and yellow lines. The background offset (coefficient A_0 in eq. 1) is selected with the white cursor in the SCD pseudo-color graph and automatically subtracted. A first order correction of the dilution effect is performed by subtracting an average UV intensity measured on a dark background framed (e.g. volcanic

rock) assuming a negligible UV reflectivity and therefore a dominant contribution from scattering effects. The dark background is selected with the yellow cursor in the SCD graph.

If the raw images exhibit an intense darkening at the edges (especially if the passband filters are placed in front the lenses), Vulcamera allows to correct it with a correction mask calculated from an image of a homogeneous clear sky as background

Plume transport speed can be calculated in Vulcamera following two methods: cross correlation between ICA time series and optical flow algorithms. The former consists in calculating two distinct ICA time series from two parallel plume profiles separated by a certain distance (dx), that will exhibit a time shift (dt) as a function of the plume speed. The shift is due to the time required by a puff of gas to travel from the first to the second profile. The cross-correlation function will find an average time shift in an interval of time and plume speed is calculated as dx/dt.

Optical flow algorithms have been extensively documented (Peters et al., 2015) as an accurate method for calculating speed vectors of trackable features of a volcanic plume (e.g. gas puff edges). The algorithms analyse the apparent motion of image objects between two consecutive frames under the assumptions that the pixel intensities of an object do not change significantly between consecutive frames, and that the neighboring pixels have similar motion.

Vulcamera allows to use two different optical flows algorithms: Lucas Kanade or Horn and Shunck (Bruhn et al., 2005) optical flow works by selecting a region in the SCD image within the red and green cursors. A dedicated front panel allows to change the the optical flow parameters. A plot with speed vectors allows to select the best algorithm and setting and apply different filters (smoothing and direction) in order to reduce errors in the plume velocity calculation.

2.3 The automatic post-processing routine

Vulcamera offers the advantage to follow the image processing frame by frame. On the other hand, this manual procedure requires a considerable amount of time (half hour for processing 4-5 hours of UV camera acquisition), especially if we are dealing with a huge amount of data such as those produced by the UV3 station (~8500 shot each day). Therefore, we have created in Matlab an algorithm for automatically processing a dataset of UV images. The automatic procedure has been calibrated using results from Vulcamera, in order to obtain the minimum differences between the two results.

Automatic procedure consists in 1) determination background absorbance level, 2) determination goodness of images using image quality indexes, 3) automatic calculation of gas speed with optical flow algorithm, 4) automatic calculation of SO_2 flux distribution; the protocol is described more in detail below.

2.3.1 automatic determination background absorbance level

To obtain background absorbance level to be subtracted as offset in the obtained absorbance images we select a horizontal profile in the image located at a distance of ~1 km above the source vents (Fig 4c). We the considered as the background absorbance level the minimum absorbance value associated with this horizontal profile.

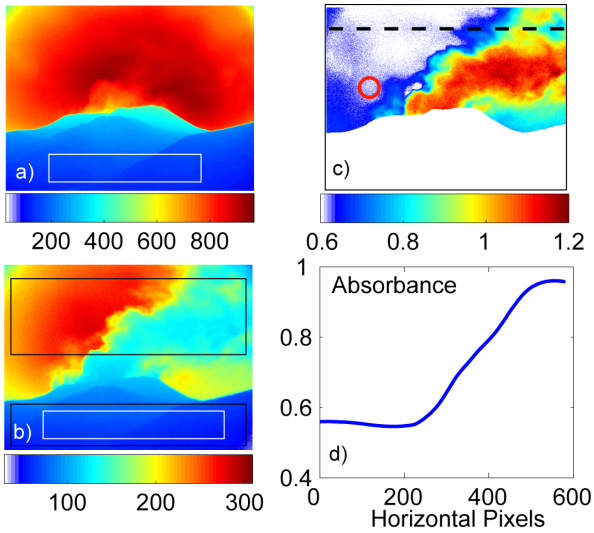

Figure 4 calculation of SO_2 column densities using dual camera method with 310 nm (a) and 330 nm (b) optical filter. Absorbance image (c) is obtained using lambert-beer equation after image normalization. Black boxes in a e b represents the ground area where absorbance is assumed to 0. Once absorbance is obtained (c), offset is removed by subtracting minimum value (d) associated with the cross section in c (dashed line). Blue rectangles in b represent the areas used for visibility index calculation. Calibration curve using co-located uv-scanning spectrometer is shown in b) which allows us to convert un-calibrated absorbance intensities into so2 column densities

2.3.2 Automatic determination of optimal viewing condition

To have a reliable SO_2 density measurements, an optimal viewing condition of the plume and the presence of a clear sky is required. However, weather condition is rather variable at the summit of Etna volcano, and thus often preventing to have reliable SO_2 measurements. To minimizing uncertainties due to poor weather condition we performed a real-time calculation of a visibility index. This index is calculated by the ratio between the mean pixel intensity associated with the camera field of view portions capturing the sky and the ground respectively. The higher is this ratio and the better is the visibility condition. SO_2

measurements are then selected using the visibility index, and thus discarding measurements too much affected by bias due to poor visibility condition.

However, the condition to detect the sky respect to the ground is not sufficient to have a reliable measurement of gas, especially with the presence of a highly condensed plume which can mask the SO_2 absorbance signal.

Thus, an additional automatic procedure is performed real time to image dataset to select only images showing an a clear SO_2 signal above the atmospheric noise.

This procedure is based by combining absorbance and 310nm image associated with the plume. SO_2 signal is well detected and measurable within the plume only when the plume shows lower intensities respect to the neighbors in the 310nm image (because SO_2 is absorbing solar radiation) and higher intensities in the absorbance image (following Lambert Beer equation). This condition is only verified if gas signal is high enough to emerge above the atmospheric noise. To discriminate this condition real time, we calculate the correlation coefficient between absorbance and 310nm pixel intensities over a cross-section intersecting the plume (Fig. 5). The closer to -1 is correlation coefficient and the more absorbance is related to gas. Images that not satisfy this condition are discarded from the automatic computation.

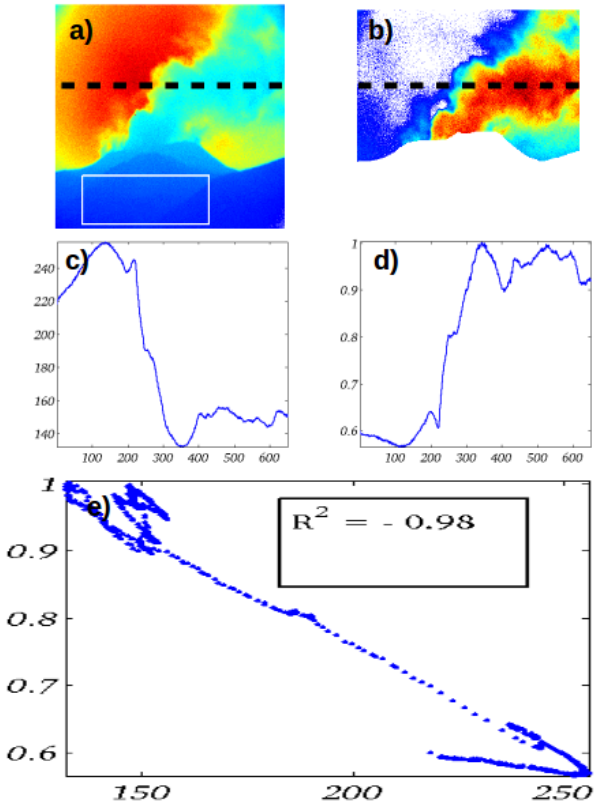

Figure 5 image quality calculation method using correlation coefficient between 310nm filter image (a) and relative absorbance image (b). Intensity profiles associated with a section (dashed line) crossing the volcanic plume for 310nm filter image (c) and absorbance image (d) is obtained. If these profiles are negatively correlated with an high correlation coefficient(e), then gas is well visible within the plume.

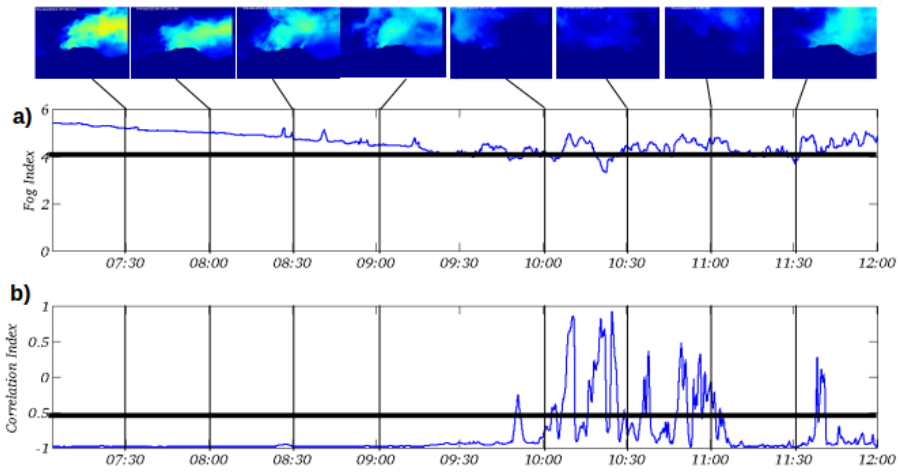

Figure 6 fog index and correlation indexes fluctuation through time as a function of visibility condition (c). Gas is well visible only when fog index is greater than 4 and correlation index is less than -0.5.

2.3.3 Plume velocity field

A reliable calculation of the plume velocity field is mandatory to have reliable SO_2 flux measurement since errors in velocity have shown to contribute up to 40% to the overall error in determination of total flux (Bluth et al., 2007; Burton et al., 2015).

The UV camera approach offers the unique opportunity to track gas while it is moving just after it reaches the atmosphere and allows us to minimize the errors due to the velocity uncertainties that affect indeed the more established DOAS and COSPEC methods, where plume velocities are assumed equal to wind velocity, that can be measured on site or also be inferred from meteorological models.

The UV camera approach allows us to derive the velocity profile over the crater terrace by applying an optical flow algorithm to track gas particles in consecutive frames.

Optical flow consists in the pattern of apparent motion of image objects between two consecutive frames caused by the movement of object or camera and is valid under the assumptions that the pixel intensities of an object do not change significantly between consecutive frames, and that the neighboring pixels have similar motion.

If a pixel, with intensity I(x,y,t), where (x,y) are the pixel coordinates and t is the time in first frame, moves by distance (dx,dy) in next frame taken after time dt, we assume that:

$$I(x,y,t) = I(x+dx, y+dy, t+dt) I(x,y,t) = I(x+dx, y+dy, t+dt) \quad \text{(eq. 2)}$$

Then the Taylor series approximation of right-hand side, remove common terms and divide by dt to get the following equation:

$$\frac{\partial I}{\partial x}u + \frac{\partial I}{\partial y}v + \frac{\partial I}{\partial t} = \mathbf{0}\ \frac{\partial I}{\partial x}u + \frac{\partial I}{\partial y}v + \frac{\partial I}{\partial t} = \mathbf{0} \quad \text{(eq . 3)}$$

$$u = \frac{dx}{dt}; v = \frac{dy}{dt} u = \frac{dx}{dt}; v = \frac{dy}{dt} \quad \text{(eq. 4)}$$

where $\frac{\partial I}{\partial x}\frac{\partial I}{\partial x}$ and $\frac{\partial I}{\partial y}\frac{\partial I}{\partial y}$, are the image gradients, $\frac{\partial I}{\partial t}\frac{\partial I}{\partial t}$ is the gradient along time, u and v, are horizontal and vertical velocities which are unknown. Lucas & Kanade (1981) provide a method to derive these unknown velocities, by solving the basic optical flow equations (eq. 2) and (eq. 4) for all the pixels using the least squares criterion and by combining information from nearby pixels. We test the performance of the method in calculating velocities by applying on artificial images with known particle velocities. The method has successfully determined velocity field with an error of <5%.

Absorbance images obtained using the two filter method allows us to obtain an image where gas-rich and ash-free portions of the plume are enhanced respect to the background and other ash-rich or particle-rich image portions because they have a higher absorbance. We then exploited this feature to track gas moving fronts in consecutive frames by filtering them from other moving features such as lapilli and ash, by applying the Lucas Kanade method to the absorbance images. Velocities are then calculated by selecting the best features to track within the image and which correspond to the areas with high pixel intensities (i.e. high SO_2 column densities) and showing high spatial coherence in consecutive frames with a time interval of 2 seconds.

2.3.4 Image analysis aimed to obtain SO_2 flux

To enhance the signal associated with the volcanic emissions respect to atmospheric noise and to avoid dispersion and chemically conversions of SO_2 once it reaches the atmosphere, image processing was conducted on a restricted image portion capturing a sub-region of the image located above the crater area (Fig 7).

Our aim is also to discriminate among different vent contribution in the total degassing in order to look at changes in degassing dynamics and location during volcanic activity (see also D'aleo et al., 2016). To do this, we selected a rectangular sub-area over the crater terrace where SO_2 column densities and plume velocity field are extracted to have a SO_2 column density and velocity distribution over the crater terrace (Figure 7). We calculated SO_2 column densities and plume speed as close as possible to the vent position, minimizing thus the effects of wind and air entrainment within the plume that would produce dilution of the SO_2 concentration as the plume moves away from the vent. This allowed us also to detect changes in degassing dynamics across the crater terrace that could be associated with changes in volcanic activity and regimes.

We then calculate velocity (mean, maximum, and associated standard deviation) and absorbance distribution along an ideal profile positioned on the middle of the sub-area. We then obtain SO_2 densities flux (in kgm-1s-1) by combining column density with velocity profiles respect to the specific horizontal and vertical component of motion along all the profiles shown in Figure 7. Velocity profiles (Fig. 7) are achieved by averaging the calculated two dimensional velocity field achieved and filtering out velocity point showing low coherence. We also derive uncertainty of velocity determination along the profile by calculating the standard deviation associated with the velocity values used to determine the average velocity, and that we used as uncertainty in the SO_2 flux calculation.

SO2 fluxes is then obtained by spatial 1D integration over the profiles. Discrimination of degassing between the different crater areas, the central and south-eastern ones, will be then obtained by algebraic sum among various SO2 flux components that border each crater, taking into account if flux is moving away or toward the vent, corresponding to a positive/negative contribution respectively. This method allows us to discriminate flux contribution from different. Given the position of the station respect to the summit crater area (Fig 7) we are able to capture with high detail gas emissions from the Southeast Crater (SEC, NSEC of Fig. 7) and that one associated with the Central crater (BN, VOR).

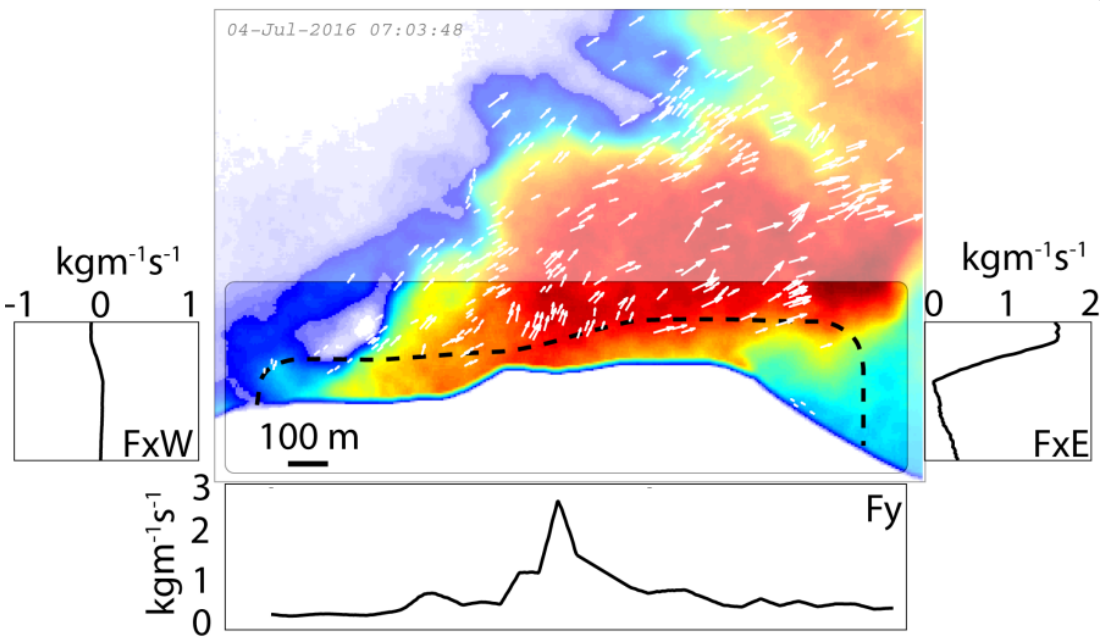

Figure 7 SO_2 column densities calculated on image encompassing the crater terrace. White arrows correspond to gas velocity vectors calculated on high coherence regions of the images. So2 density flux distributions along the entire crater area and over the black dashed profile is calculated within the highlighted area and shown in b), c) and d), corresponding to the vertical, western and eastern horizontal components respectively. So2 total flux for a given sector is then calculated by integrating the density flux over the total length of the profile

For the given profile P(x,y) of figure 7, where (x,y) are the pixel coordinates associated with every points of the profile, we calculate SO2 flux as integration of SO2 column densities and normal velocity component over the profile:

$$\mathrm{f}SO_2 = pd * \alpha * \sum_i A^i(x,y) v_n^i(x,y) \qquad \text{(eq .5)}$$

where *pd* is pixel dimension (in meters), α is the empirical coefficient to convert uncalibrated absorbance (*A*) into column densities (kgm^{-2}) which derives from DOAS analysis, v_n is the normal velocity component over profile (in m/s), and *i* is pixel index associated with the profile.

Chapter 3
Etna

3.1 Activity and geological history of Etna

Mt. Etna is the largest European volcano. It is located in the east side of Sicily and covers an area of 1250 km^2, reaching 3340 m of elevation. It is one of the most active basaltic volcanoes in the world, and one of the largest volcanic SO_2 point sources to the atmosphere (Allard et al., 1991; Allard, 1997; Caltabiano et al., 1994, 2004). It lays on a sedimentary basement made of flysch and clayey deposits that belong to the Maghrebian-Appenninic chain (Lentini**,** 1982), overlaying a 10 km-thick carbonate sequence. Close to Etna, three principal geodynamics domain are recognized:

- The Maghrebian-Appenninic and Calabrian arc, on the north;
- The Iblean foreland, on south;
- The Gela-Catania foredeep, on southwest;

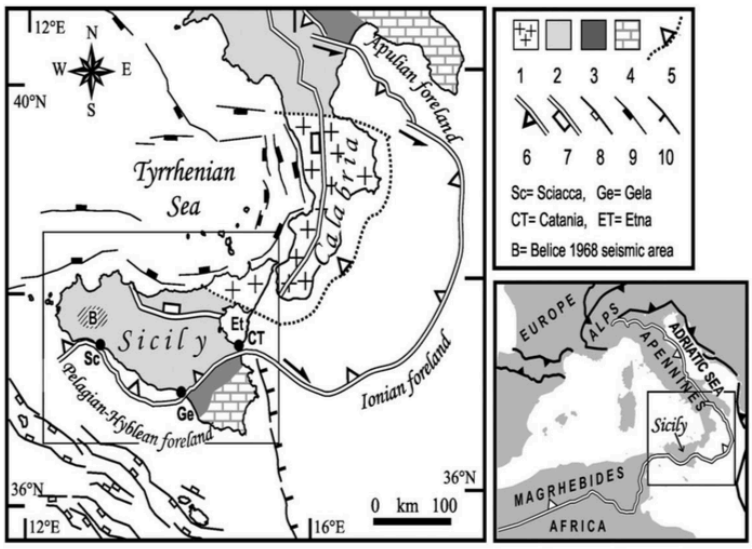

Figure 8 structural and tectonic settings of etna's area with the structural domain of south of italy. 1 peloritan-calabrian metamorfic unit (thrust system); 2 maghrebian-appenninic unit (fold and thrust system); 3 foredeep deposits; 4 iblea and apula foreland; 5 peloritan unit alpin-trust front; 6 external front of the maghrebian-appenninic chain; 7 external limit of the extensional upper crust; 8 fault system of the sicily channel; 9 normal fault of the tirrenian sea; 10 malta (form lavecchia et al., 2007)

Mt. Etna developed at the intersection of three regional faults systems:

1) the Tindari-Giardini system and the connected Maltese fault escarpment, both oriented NNW-SSE and elongated discontinuously from the Aeolian Islands to the Island of Malta (Carbone et al., 1987).

2) the Comiso- Etna system and its inferred prolongation, the Messina - Capo Vaticano system (Lo Giudice et al, 1982; Bousquet et al, 1988). This fault system trends NE - SW and extends discontinuously from the southwestern limit of the Hyblean foreland to the Catania plain and further northeast, from the northeastern boundary of Etna to southwestern Calabria. The southwesternmost portion of the Comiso—Etna system marks the boundary between the Hyblean foreland and the Gela-Catania foredeep.
3) the Monte Kumeta-Alcantara system, oriented E - W (Ghisetti and Vezzani, 1984), which runs through central Sicily and bounds the northern side of Mt. Etna. Both the Maltese fault and the Comiso—Etna— Messina systems are subject to tensional strains and guide the ascent of Etna's magmas from depth, as the majority of the tectonic structures and eruptive fissures in the Etna area follow one of these two structural directions (Chester et al, 1985; Rasa et al, 1995). At a regional scale, the NE-SW and the NW-SE fault systems separate two main structural units: the Maghrebian-Appenninic chain to the north, which is part of the Euroasian plate, and the Hyblean platform to the south, which instead belongs to the African plate (Lentini, 1982).

A strong relation exists between tectonic setting and Etna's volcanic activity. Although eruptions at the summit craters and/or their upper slopes are the most frequent, eruptions occasionally occur along the volcano's flanks, where magma ascent is favoured by weakness zones called rift, located along the main active faults.

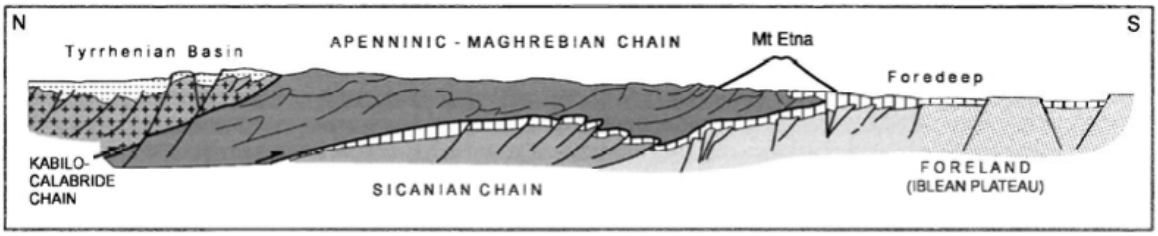

Figure 9 schematic cross-section along eastern sicily, highlighting the geometrical relationship between the main structural domain forming the apenninic-maghrebian orogenic belt and the location of etna volcano (branca et al. 2004, redrawn after lentini et al., 1996)

Mt. Etna overlays a continental crust of ~22 km thickness, which borders the 10-12 km thick Ionic basins. The Maltese fault Escarpment marks the limit between the continental and the oceanic crust. With 200 km of extension, it is the main active fault of the Mediterranean Sea.

Etna volcano developed in four main stage (fig. 10), each being characterized by different petrological and structural features (Branca et. al, 2004)

- Basal Tholeiitic phase (a) (600.000-250.000 years ago)
- Alkali-basalts Timpe phase (b) (250.000-100.000 years ago)
- Valle del Bove centers phase (c) (80.000-40.000 years ago)
- Mongibello strato-volcano phase (d) (last 40.000 years)

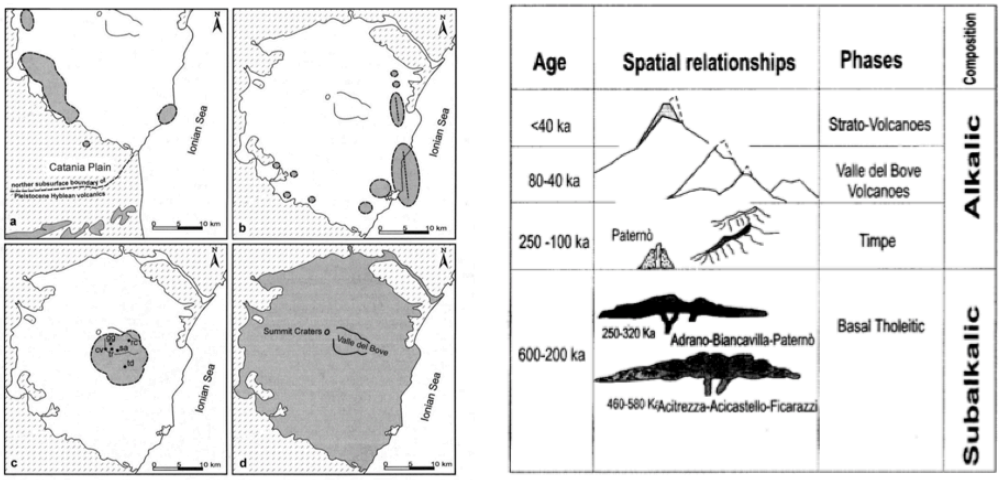

Figure 10 left: spatial evolution of mt. Etna history: a) basal tholeiitic phase; b) timpe phase; c) valle ddel bove centre's phase; d) strato volcanoes phase. Right: structural scheme, age (gillot et al., 1994) and phases of etnean magmatism as proposed by (branca et al., 2004) form corsaro and pompilio 2004.

Volcanic activity started ~500ka ago (a) with fissural-type submarine eruptions that produced tholeiitic basalts (Gillot et al. 1994; Tanguy et al., 1997). These earliest volcanic products outcrop between the villages of Aci-castello and Acitrezza. They consist of a shallow sub-volcanic body that fed the eruptions of pillow lavas, and hyaloclastic breccias at a depth of a few hundred meters (Corsaro and Cristofolini, 1997; 2000). The early submarine volcanic events were followed by subaerial eruptions, in concert with a regional uplift starting ~ 300 ka ago (Branca et al., 2008). The composition of the erupted products shifted from tholeiitic to transitional to Na-alkalic (~ 200 ka; Tanguy et al., 1997). Along the Ionian coast, north of the Acicastello-Acitrezza area, the products of the Timpe phase (b) crop out at the base of the Acireale Timpa fault scarp, below the village of S. Caterina. A columnar lava body passes laterally to strombolian deposits and overlaying thin lava flow

gently dipping SW. These volcanic rocks, rich in mafic crystals and nodules, represent the remnants of an eruptive fissure oriented as the Timpe fault system (Corsaro et al**.,** 2002).

The building of central-conduit edifice started ~ 130 ka ago (c) with the Valle del Bove volcanic center, resulting in a sequence of several distinct volcanic edifices characterized by alternation of effusive and explosive eruptions, and frequently associated with caldera collapses (De Beni et al., 2005). The last phase of the evolution of the Etna volcano is the Ellittico eruptive center, which was located in the area of the present summit, about 3-4 km NW of the older eruptive centers of VdB. From K/Ar radiometric age determinations on lavas in the VdB (Gillot et al 1994, Trie et al. 1994), onset of the Ellittico eruptive activity has been set at ~80 ka ago. Four caldera-forming eruptions, occurring in a rather short period about 15 ka ago, ended the activity of the Ellittico volcano, and caused the collapse of the volcano summit that presently is truncated at about 2850 m a.s.l. The caldera has an elliptical shape [3.5 x 2.5 km] stretched in NNE direction. Small remains of the caldera rim are still visible at Punta Lucia and Pizzi Deneri, on the northern flank. The Ellittico caldera was almost completely refilled by lava flows and ponds, exposed on the western wall of VdB, at the beginning of Mongibello volcanic activity. Afterward, lava overflowed on the southern flank burying most of the caldera rim and leaving its testimony (Punta Lucia and Pizzi Deneri) only on the northern side (Branca et al., 2004).

Mongibello volcano products, erupted in the last 14 ka, mantle most of the Ellittico stratovolcano; in fact, they cover about 85% of Etna's surface. With respect to the Ellittico volcano, the following eruptions occurred in both summit (or central) vents and flank (or lateral) vents during periods of almost persistent strombolian activity at the summit and large flank lava-flow eruptions from vents located from 2800 to 400 m a.s.l. Strong explosive activity also occurred, reaching the subplinian magnitude several times, and the plinian one once. The spatial distribution of the eruptive vents evidenced the presence of at least three main weakness zones of the volcano edifice (NE, S and W) in which the intrusion of feeder dykes prevalently occurred. The Mongibello succession is mainly constituted by lava flows and minor pyroclastic fallout deposits. Strombolian deposits form the summit cone and the adventive scoria cones are widespread on the volcano flanks. Lava flows are mainly compound lava fields characterized by an aa morphology or a more complex aa and toothpaste morphology. Conversely, pahoehoe lava flows are relatively uncommon. The eruptive vents are formed by single or coalescent monogenic strombolian cones, made of bombs and lapilli layers, or by spatter ramparts extended along the eruptive fissures dotted by hornitos. (Branca et al., 2004). The morphological setting of the Mongibello volcano was radically

modified about 10 ka ago by a catastrophic eastern flank collapse that produced the wide depression of the V d B (Calvari et al., 2004).

The present feeding system is interpreted as an open-conduit system developed at the intersection of two main volcano-tectonic structures: the North East Rift and the South Rift (Ferlito et al., 2009; Giacomoni et al., 2012), which are strictly related to the trans-extensional regional tectonic regime (Monaco et al., 2005). The main volcanic conduit is persistently filled with magma at different levels, which undergoes continuous degassing from the summit craters (Corsaro et al., 2009).

3.2 Previous studies on the Etna's SO_2 flux

Etna is one of the volcanoes worldwide with the longest and most continuous SO_2 flux record. The degassing behaviour of Etna consists in persistent passive SO_2 plume emissions that occur via the five main summit craters (Voragine, VOR; Bocca Nuova, BN; North East Crater, NEC and South east Crater SEC, New south east Crater NSEC), which contribute to almost the totality of the emitted SO_2. Additional emissions, which are sometime very vigorous, do temporary take place during eruptions (Caltabiano et al., 2004). The summit craters are the culmination of the open-conduit feeding system permanently active, which is usually characterised by three types of activity:

a) Non-eruptive (quiescent) emissions of a gas plume from the lava free surface ponding in the upper feeding conduits, or from fumaroles spotting the inner walls of the craters. This is a persistent degassing process, and by far the most significant at Etnean volcano in terms of mass budget. This passive and eruptive gas release is impressive, with SO_2 fluxes ranging between 840 and 21000 tons/day (t/d). The SO_2 flux average for non-eruptive periods is 5000 t/d (Allard et al., 1991; Allard, 1997).

b) Effusive eruptions with low emission rate (typically, < 4 m^3/s), scarce or null explosiveness, and long duration (months/years), generally occurring on short fractures at the base of SEC and NEC.

c) Violent explosive eruptions (paroxysms) occurring on the main vents of all craters, with lava fountains of up to 1 km high, fast lava flows, high emission rate ($\gg 100$ m^3/s) and short duration (hours).

Phases (b) and (c) are typically associated with higher SO_2 fluxes (> 10,000 tons/day).

SO_2 flux measurements have been fundamental to volcano monitoring at Etna since 1970's, with the development of the Correlation spectrometer (COSPEC) (Moffat and Millan, 1971; Stoiber et al, 1983). Malinconico (1979) first observed that increases in SO_2 flux corresponded to increases in volcanic activity. Mt. Etna has been the volcano most intensively surveyed with COSPEC, intermittently between 1975 and 1986 (Haulet et al., 1977; Allard et al., 1991), and routinely since 1987 (Caltabiano et al., 1994; Bruno et al., 1999). Measurements were carried out on a weekly basis since 1987, and two to three times a week since October 1996.

Caltabiano et al. (2004) reviewed a dataset of ~15 years of SO_2 flux observations. They reported a mean flux value of ~5500 t/d, associated to the passive degassing, increasing to up to ~26000 t/d during eruptive periods. Figure (11) shows a low-pass filtered (with different cut-off applied) SO_2 signal (Caltabiano et al., 2004). Results highlight some cyclic oscillation of the SO_2 flux, including a 4-year component that was related to long-term periodical supply, replenishment or/and long-term periodic overturning of magma within the feeding conduit system of the volcano.

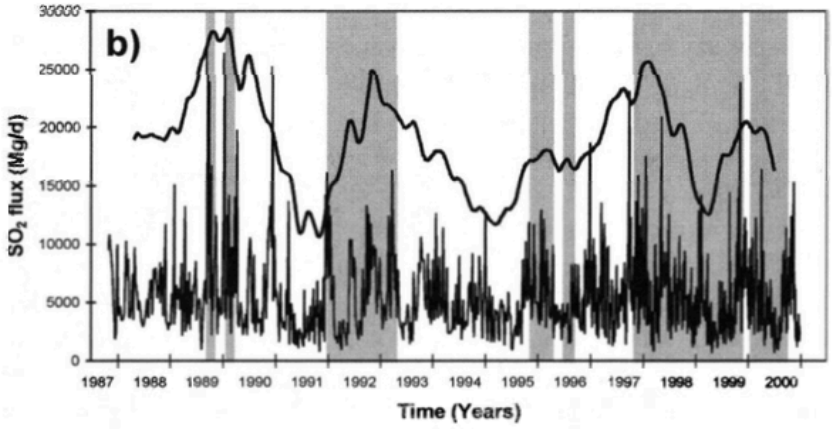

Figure 11 so$_2$ fluxes during the 1987-2000. The grey bands indicate mt. Etna's eruptive activities. The tick cure in the upper part of the graph highlights the 4-years component. Superimposed filtered signals are shown in arbitrary units. (from caltabiano et al. 2004)

These first continuous SO_2 dataset also allowed establishing correlations between and seismic tremor, as shown in figure 12 (Caltabiano et al., 2004). This correlation is particularly clear during periods of strong eruptive activity, as described in Leonardi et al (1999).

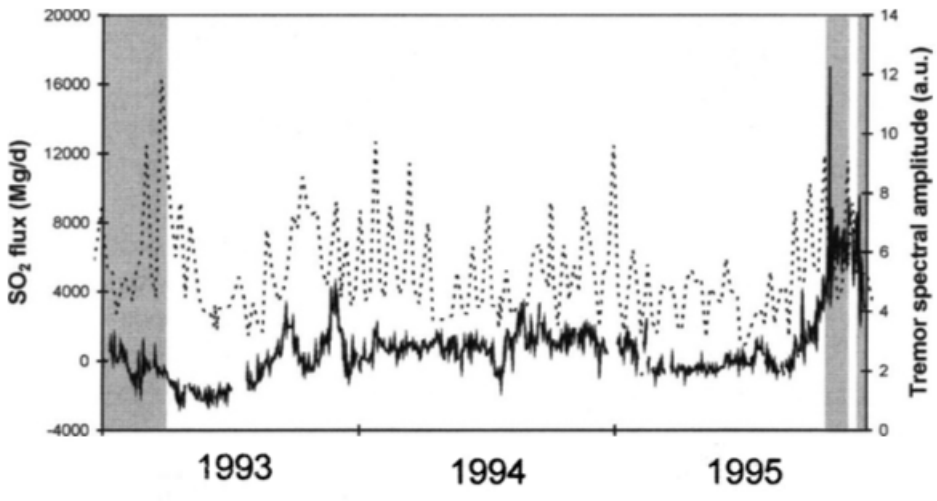

Figure 12 comparison between the so_2 flux (dashed line) and the tremor spectra amplitude (solid line expressed in arbitrary units) at mt. Etna in the period 1993-1995. The grey bands indicate mt. Etna's eruptive activities (from caltabiano et al., 2004 modified from bruno et al., 1999)

This evidence implies that volcanic tremor and SO_2 emissions are produced by a common physical mechanism, related to shallow magma degassing. Other correlations were found between SO_2 flux changes and volcanic earthquakes heralding eruptive activity. For example, drastic drops of the SO_2 flux were observed in coincidence with deep earthquakes recorded about 4 to 6 weeks prior to eruptions and located mainly beneath the western flank of Mt. Etna. In particular, the deep seismic events of August 3, 1989 and October 23, 1991 ($h > 7$-10 km according to Castellano et al., 1995) and the minimum SO_2 flux values of August 9, 1989 (970 Mg/d) and November 8, 1991 (840 Mg/d) were temporally correlated with the onset of 1989 and 1991-1993 eruptions, respectively. Minimum SO_2 flux values, particularly if coupled with deep seismicity, were proposed as indicators of impending eruptive activity and/or upward magma migration by Caltabiano et al, (1994) and Bruno et al, (1999).

More recently, the COSPEC has been largely superseded by compact scanning spectrometers utilizing the Differential Optical absorption spectrometer (DOAS) method (McGonigle, 2005) for retrieving SO_2. In October 2004, the Istituto Nazionale di Geofisica e Vulcanologia (INGV), Sezione di Catania, installed a network of automated scanning DOAS (Salerno et al. 2009) called FLAME (Flux Automated Measurement). This network provides continuous SO_2 flux measurements from a network of DOAS spectrometers, located at ~500m asl, connected by an optical fiber to a telescope that automatically turn scanning the sky in a vertical plane, intersecting the plume at a distance of ~14km from the summit crater. The device is controlled by a custom-built circuit board collecting data daily for almost 9 h depending on the season, and acquiring a complete scan (105 spectra including

a dark spectrum) in ~6 min (Salerno et al. 2009). Such abundance of data brings to a wider understanding of the volcano behaviour from long period variation up to very short, that can characterize a single eruption. Today, the FLAME network is routinely used for monitoring the volcano's behaviour (Salerno et al., 2009; Bonaccorso et al., 2011; Patanè et al., 2013; Spampinato et al., 2015; Corsaro et al., 2017).

In recent years, the advent of the UV camera (Mori and Burton, 2007) has allowed the first high-rate, high spatial resolution measurements of the volcanic SO_2 flux at Etna. The first camera-based SO_2 flux records at Etna are discussed in Tamburello et al., (2013) and Pering et al., (2014a, b) and Wilkes et al., (2017).

Tamburello et al., (2013) analysed the very short period variation in the Etna plume gas flux, tens of second. This "puffing" behaviour is most evident when viewed from the rim of the crater: gas emission virtually stop between on puff and the next. The advent of UV imagining techniques bring an image acquisition rate of ~1Hz, this linked with the calculation of the plume transport speed directly from the image allowed to retrieve SO_2 flux time series with unprecedented high resolution. This sign a step forward in SO_2 flux calculation that, until UV camera used the wind speed retrieved by meteo forecast calculation or meteo station far from the gas source, a mean value of daily wind speed was used to calculate flux from a SO_2 column amount time series measure by several scanning or traverse with DOAS (La Spina et al., 2010; Salerno et al., 2009).

As regards the high-frequency structure of the acquired SO_2 time series, the dataset shown in figure 13 supports the existence of a non-stationary (periodic) degassing SO_2 regime from the North-East crater. The author broadly distinguish two SO_2 variation patterns:

. low period SO_2 flux fluctuations, lasting tens of seconds, and having a mean amplitude of ~ 6 $kg \cdot s^{-1}$ (therefore accounting for ~50% of the average flux). On a typical sequence of consecutively collected UV images, this degassing pattern is clearly detectable as a succession of sizeable clouds of highly concentrated SO_2 being rhythmically released by the vent's rim (Fig. 13);

. longer period flux fluctuations, lasting thousands of seconds, and only barely identifiable in a time series of 6 hours. In Fig. 13, these longer period cyclic fluctuations in SO_2 release are highlighted by the moving average.

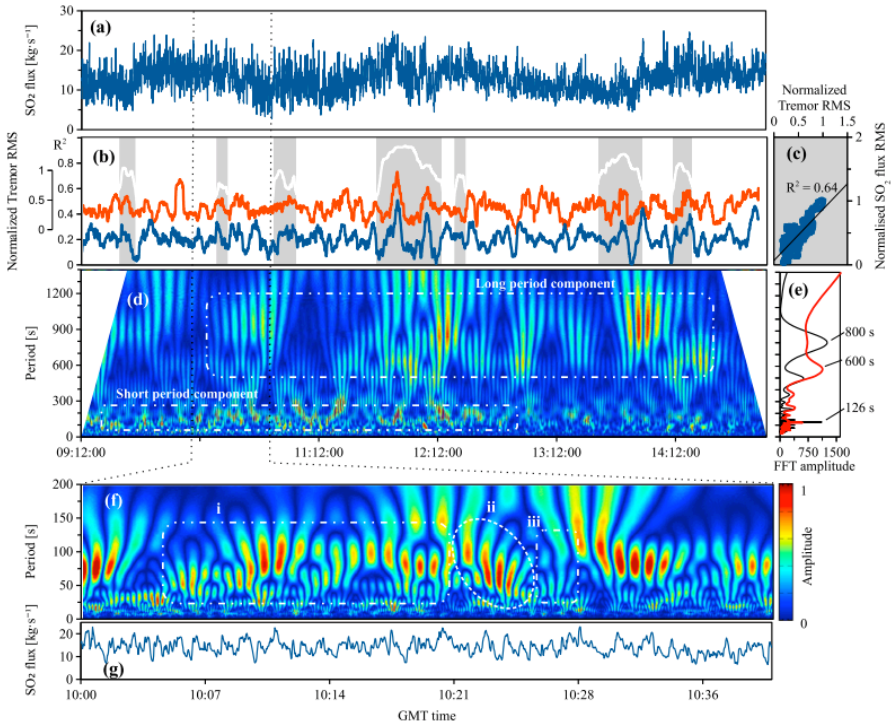

Figure 13 (a) so2 flux time series (blue line, in kg/s) from the nec on 1 july 2011; (b) normalized root-mean-squares of gas (blue) and seismic tremor (orange, m· s?1) amplitudes (calculated within a 200 s moving window); grey areas show the intervals in which rmss exhibit high correlation coefficients (r2<0.6, white line) within a window of 2000 s; (c) so2 flux versus normalized rms of seismic tremor scatter diagram of the intervals within grey areas; (d) normalized dt-cmwt and (e) fft of the so2 flux signal (black curve) (from Tamburello et al., 2013)

Studying the SO_2 flux time-series has contributed key information on the Etna's degassing behaviour. The SO_2 flux can provide indirect information on the volume of degassing magma within the volcano. Knowing the initial and residual sulfur content in Mt. Etna basalts, the measured SO_2 flux can be converted into a rate of magma degassing from the equation (Allard, 1997):

$$Q(SO_2) = 2\ Ve \bullet [S] \bullet \rho \bullet (1\text{-}x) \quad \text{(eq. 5)}$$

where [S] is the degassed weight fraction of elemental Sulfur, and ρ the density of the degassed basalt at 1100°C, with a mean crystallinity (x) of 30% (2700 kg/m^3; Armienti et al., 1994). Because nearly all Sulfur is lost from the melt upon eruption (e.g. Metrich et al, 1993), the weight loss of S during degassing is equivalent to the initial Sulfur content of the melt (0.3 wt. %).

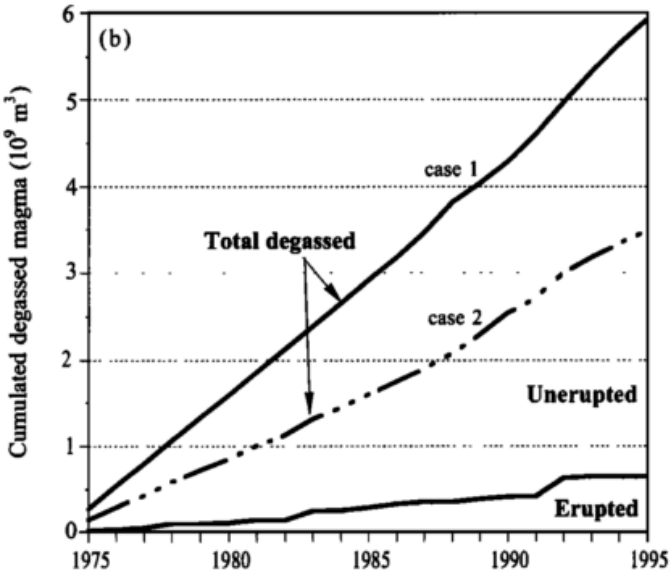

Figure 14 cumulated amount of erupted (ve) and unerupted (vu) degassed magma. The two curves for total degassed magma (vd) with distinct shape, reflect upper and lower estimates for vu, based on a bulk sulfur loss of either 0.15 wt % (case 1) or 0.3 wt % (case 2) during non eruptive degassing of hawaiitic basalt. From 3.5 to 5.9 km^3 of magma was degassed over 21 years, 82 to 89% of which did nor erupt(from allard 1997)

By integration over a specific temporal interval, this procedure allows comparing the degassing magma volumes with the volume of magma erupted in the same period, as obtained from field observations. This comparison demonstrates that only ~10-20% of degassing magma is finally erupted (Allard 1997; Caltabiano et al. 2004). This implies a separated conduit flow of gas and melt, and storage or/and recycling of most (~ 87 %) of the degassing magma within or/and beneath the volcano (Allard 1997; Allard et al., 2006). This amount of "missing" magma becomes sterile to further SO_2 release, and is replaced with new basalt that is needed to sustain the SO_2 flux. The upper Etna's plumbing system is not large enough to accommodate several cubic kilometres of degassed (plus un-degassed) basalt that are produced at the average basalt degassing rate of 0.17-0.28 km^3/yr (Allard 1997; Allard et al., 2006). Hence, this magma is more likely removed beneath the volcano due to a convective overturn started by the density difference between new ascending magma and degassed magma. The sinking of the degassed magma gives rise to formation of a huge 'plutonic' complex, about 10 km wide and deep, detected within the sedimentary basement of Etna (Allard, 1997).

Figure 15 show a recent view of Etna's summit crater (Corsaro et al 2017) with the 2014 and 2015 lava flows. Volcanic activity at Etna was confined to the summit area. Etna's summit comprises a main cone embracing two craters, Bocca Nuova (BN) and Voragine (VOR), and two parasitic cones, NE Crater (NEC), SE Crater (SEC) and the New South East (NSEC), located respectively to north and south of the eastern border of the main cone.

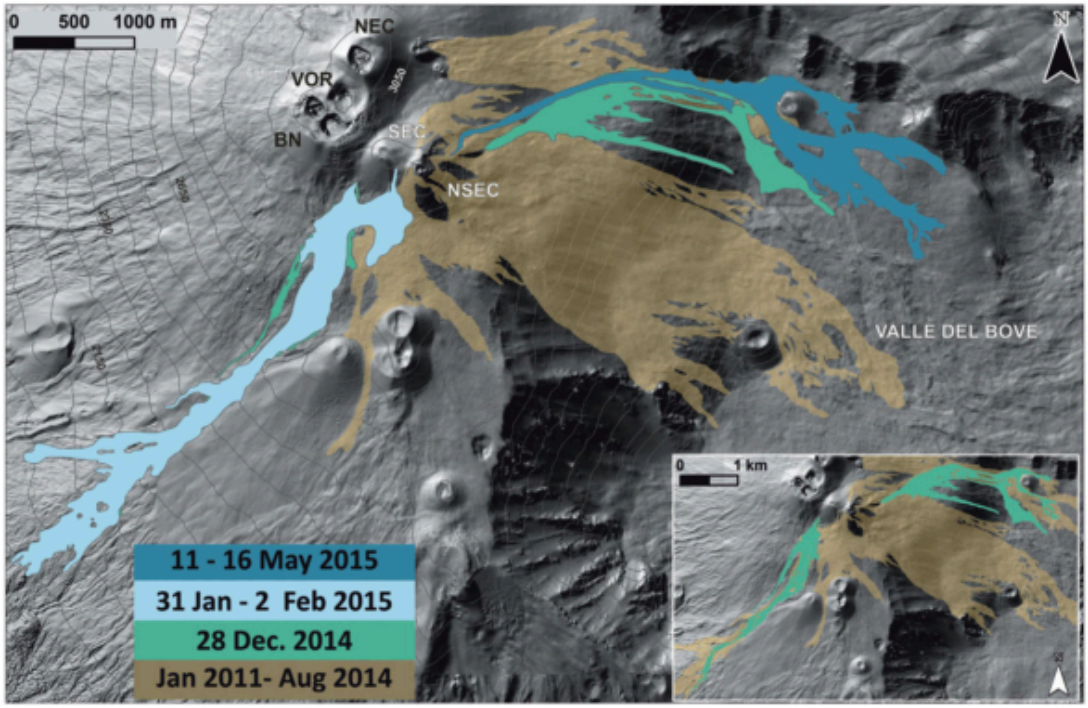

Figure 15 Shaded relief of Mt. Etnawith the lava flows emitted between 12 January 2011 and 16May 2015. The digital elevation model was produced by the Laboratorio di Aerogeofisica, Sezione Roma 2, INGV trough helicopter survey on October 2014. The inset shows the lava flow field of 28 December 2014 paroxysmal activity, formed by two lava flows spreading toward E and SW. The SW lava flow was almost completely covered by the lava flow of the 31 January–2 February 2015 activity. (From Corsaro et al 2017)

Several studies tried to explain the different volcanic activity of Mt. Etna, through both petrological (Corsaro et al. 2007) and geochemical (La Spina et al., 2010) analysis. La Spina et al., 2010, in order to explain the strong fractionation of CO2/SO2 and other gas ratios measured between the summit craters, propose a branched conduit system (fig. 17), constrained by a requirement for an integrated bulk degassing process from the sum of crater gas emissions. This simple model requires a fixed physical branching pressure (PB), where gas and magma feeding the volcano can separate in different proportions before entering the NEC and CC conduits.

Corsaro et al., 2007 (fig. 16) observed striking differences in petrography, mineralogy and chemical composition of products erupted by the Upper and Lower vents during the 2001 eruption that reflected distinct intratelluric conditions in a complex plumbing system where magmas resided in distinct reservoirs and ascended following different paths. The different composition of erupted magma and of gas compositions bring different author (Burton et al., 2003; Giammanco et al., 2013; La Spina et al 2010; Spilliaert et al., 2006) to create several models of deep and shallow plumbing system.

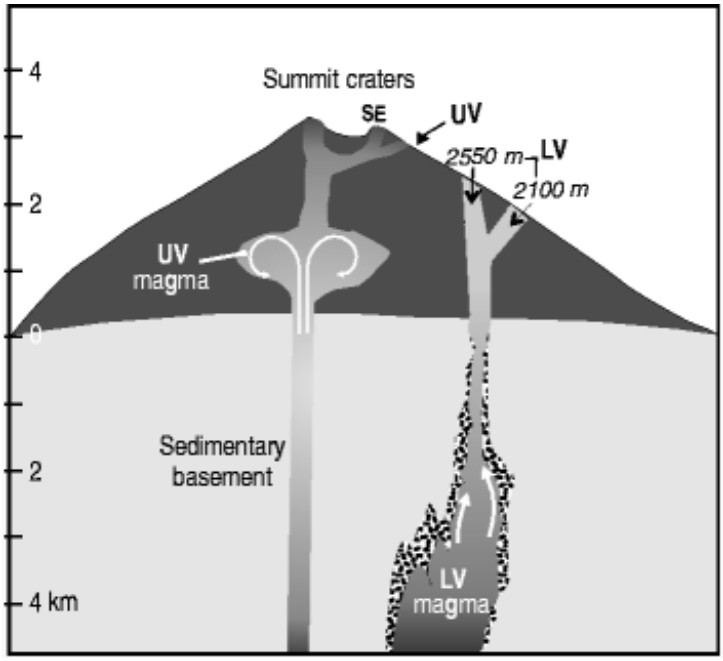

Figure 16 Schematic cartoon of Mount Etna plumbing system feeding the activity of Upper and Lower Vents during 2001 eruption, projected on a vertical plane roughly cutting E–W the volcano. SEC South East Crater, UV Upper Vents, LV Lower Vents From Corsaro et al 2007

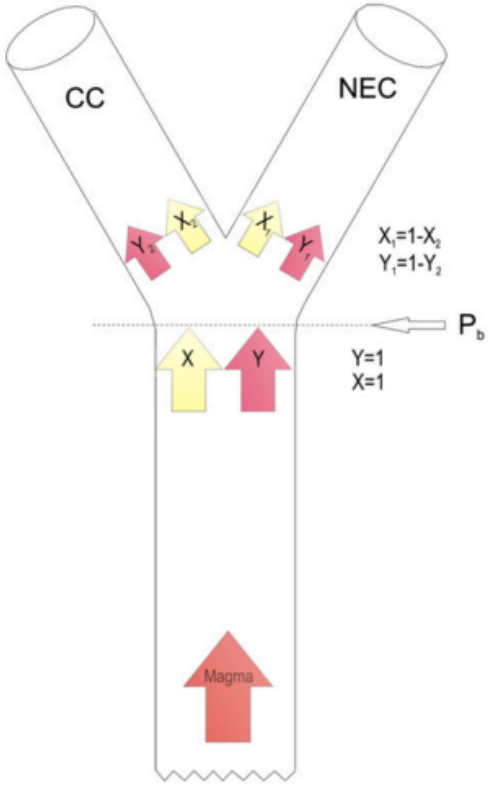

Figure 17 Sketch of the proposed model. The amount of magma entering the system (lower red arrow) is calculated from the SO2 flux (Allard, 1997). Pb is the pressure of conduit branching point. X and Y are the mass of gas and magma below the branching point, respectively. X1 is the proportion of the gas phase entering NEC and X2 (1−X1) entering CC. Y1 is the proportion of the magma phase entering NEC and Y2 (1−Y1) entering CC. (La Spina et al., 2010)

Chapter 4
Results

4.1 Introduction

In the following chapters (4-6), I report on the results of three years of SO_2 flux observations on Mt. Etna volcano, obtained using a permanent network of UV cameras installed within the ERC-funded project "Bridge". In this temporal interval, several eruptions have occurred at Etna, having different styles and dynamics, and thus offering the opportunity to test the value of the camera network for monitoring porpoises.

Figure 18 summarises the SO_2 flux dataset, obtained at Etna during 2014-2016. Results obtained in the 3 years are separately discussed in chapters 4 to 6.

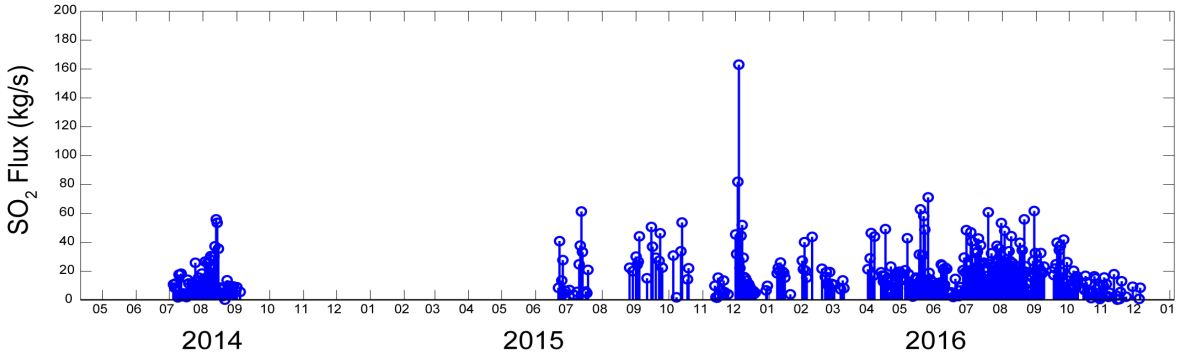

Figure 18 uv camera-based time-series of the total so_2 flux released by mount etna in 2014-2016

The following chapter and sub-chapter constitute the main body of papers already published (chapter 5 and 8) submitted (chapter 6 and 7).

Chapter 4.2 "Spatially resolved SO2 flux emissions from Mt Etna" is an article published on Geophysical Research letters on 2016 by D'Aleo, R., M. Bitetto, D. Delle Donne, G. Tamburello, A. Battaglia, M. Coltelli, D. Patanè, M. Prestifilippo, M. Sciotto, And A. Aiuppa.

Chapter 5 "Degassing processes during Mt Etna's December 2015 paroxysmal sequence" submitted on Frontiers in Earth Science by D'Aleo R., Bitetto M., Delle Donne D., Coltelli M., Coppola D., McCormick Kilbride B., Pecora E., Ripepe M., Salem L.C., Tamburello G. and Aiuppa A.

Chapter 6 "An automatic algorithm for real time processing of UV camera data: methodology and application to the 2016 Etna's activity" submitted on Geoscience by Delle

Donne D., Aiuppa A, Bitetto M., D'Aleo R., Coltelli M., Coppola D., Pecora E., Ripepe M., and Tamburello G;

Chapter 7 "Volcanic Plume CO_2 Flux Measurements at Mount Etna by Mobile Differential Absorption Lidar" published on Geoscience in 2017 by S. Santoro, S. Parracino, L. Fiorani, R. D'Aleo, E. Di Ferdinando, G. Giudice, G. Maio, M. Nuvoli and A. Aiuppa.

My contribution in these scientific papers consists in the development of the UV camera instrument, hardware and software, in conducting the field experiments, the manual process of the UV data in order to calculate gas velocity and SO_2 flux, and in the draft of the manuscripts. All these papers, use a multidisciplinary approach in the study of the volcano behavior, I brought the geochemical point of view in all of these teamwork.

During 2014 (Chapter 4.2), eruptive activity at Etna was characterized by explosive (strombolian) and effusive activity in an Eruptive Fracture (EF) opened within the Valle del Bove, between the North East Crater (NEC) and New South East Crater (NSEC). This EF eruption, started in July 2014 and ended in August 1, was carefully monitored by the UV camera network, which also allowed following eruptive activity shift from EF toward NSEC, occurred on 10 August.

During 2015, Etna remained relatively quiet between June and mid-October. On 3-5 December, four violent paroxysms occurred on Voragine crater with an eruptive column eight up to 15 km. Volcanic activity then shifted toward the NSEC, which produced strombolian activity and lava flows. This violent 2015 activity offered the opportunity to quantify, for the first time, the SO_2 budget of an Etna's paroxysmal sequence. Results are discussed in Chapter 5.

Year 2016 (Chapter 6) was characterised by a paroxysmal lava fountain at Voragine on May, and by mild strombolian activity at the same crater during August. In the end of the year, the erupted material accumulated inside the Central Crater slowly subsided. The SO_2 flux variations accompanying this time-changing activity are analysed and discussed in Chapter 6.

4.2 Etna 2014 eruption:

Spatially resolved SO_2 flux emissions from Mt Etna [1]

The advent of increasingly sophisticated imaging techniques (Platt et al. 2015) has recently prompted a revolution in our ability to study volcanic gas emissions. Ground-based observations via UV cameras (Mori and Burton, 2006), in particular, have granted acquisition of volcanic SO2 flux time series of unprecedented temporal and spatial resolution, thus paving the way to a variety of novel volcano monitoring applications (see Burton et al. [2015] for a review). Importantly, UV cameras can allow examining "fast" degassing processes at high-rate and in real-time, therefore opening the way to integration of geophysical and volcanic gas datasets into multidisciplinary models of volcanic explosions (Dalton et al. 2010; Nadeau et al. 2011; Tamburello et al, 2012; Waite et al., 2013; Pering et al., 2015), passive degassing (Tamburello et al., 2013) and lava lake dynamics (Nadeau et al. 2015).

One additional advantage of UV cameras is that, at least in principle, these are suited to adaptation to fully automated, permanent systems for long-term SO_2 flux monitoring (*Burton et al*., 2015; *Kern et al*., 2015). Within the context of the FP7-ERC-funded Project *BRIDGE* (http://www.bridge.unipa.it/), we recently deployed two stand-alone UV camera systems on the flanks of Mt. Etna volcano, one of the strongest punctual sources of volcanic gas worldwide (*Oppenheimer et al*., 2014). Etna has one of the longest and most complete records of volcanic SO_2 flux (*Caltabiano et al*., 2004). However, the majority of the available data are spectroscopically sensed from relatively remote measurement sites, located several km away from the volcano's summit. In such conditions, any transient at high frequency degassing signal (e.g., from puffing behaviour and/or discrete explosions) is lost during atmospheric transport, the contribution of individual gas sources, such as vents, cannot be resolved, and the temporal resolution of observations is typically in the ~10s of minutes range (*Salerno et al*., 2009).

Here, we report on results obtained from the BRIDGE network, in a period encompassing the summer 2014 eruptive episode(s) of Etna volcano. We show that our observations contribute spatially and temporally resolved SO_2 flux time-series that, when interpreted in tandem with independent volcanological and geophysical (seismic tremor and infrasound data) information, allow to fully interpret and understand the time changing degassing and

[1] Article published on Geophysical Research Letters, 2016, vol. 43, pp. 7511–7519, doi:10.1002/2016GL069938

eruptive behaviour of the volcano. We demonstrate, in particular, that transition from one degassing/eruptive mode/site to another, a recurrent process on Etna (*Allard et al*., 2006; *Marchetti et al,* 2009; *Cannata et al.* 2011a; *Patanè et al*., 2008, 2013), can be fully captured from the UV camera

.

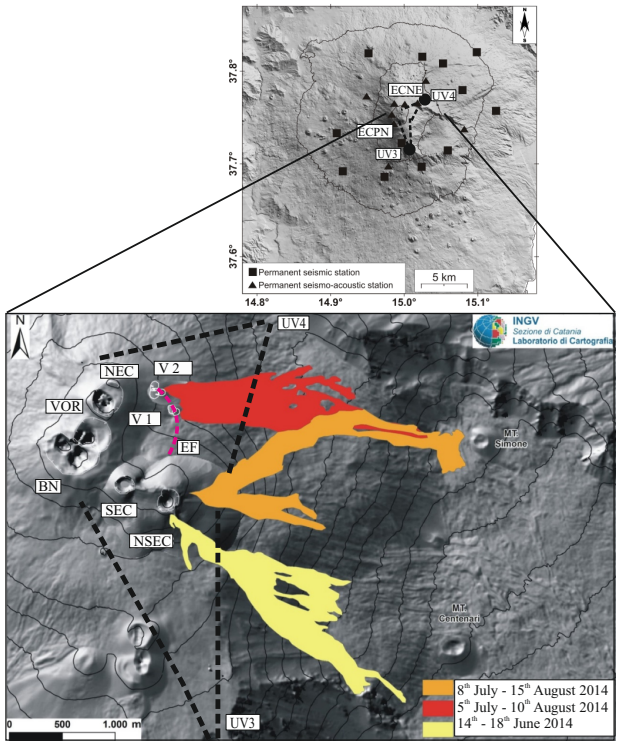

Figure 19 (a) digital map of mt. Etna showing the location of the permanent uv camera systems (uv3 and uv4; with their field of views) and of the geophysical multi-parametric stations (ecne and ecpn) which data are used in the present study; (b) a detail of (a), with the 5 etna's summit craters (nsec: new southeast; sec; southeast; bn: bocca nuova; vor: voragine; nec: northeast). The summer 2014 eruptive fissure (ef) and vents (v1: vent of ef phase 1; and v2: vent ef phase 2), and the june-august 2014 lava flow fields are also indicated (re-drawn from de beni et al. 2015 and ingv-oe monitoring reports; see www.ct.ingv.it).

4.2.1 Materials and methods

The SO_2 flux data were collected with a network of permanent, fully autonomous UV cameras run by University of Palermo. The network includes two stand-alone UV camera systems installed at La Montagnola (UV3), 3.5 km from the New South East Crater (NSEC), and at Pizzi Deneri (UV4), 2 km from the North East Crater (NEC). The two UV camera systems are designed to separately resolve degassing activity from Etna's summit craters NSEC (Fig. 20a) and NEC (Fig. 20b). We specifically designed the network (Fig. 19) to also capture the degassing from any eruptive fissure (EF) opened on the upper Etna's Eastern flank (the upper Valle del Bove area; Fig. 19), where eruptive activity has systematically

been concentrating since 2004 [*Behncke et al.,* 2006, 2014]. Our SO_2 flux time-series do not account for degassing from Bocca Nuova and Voragine craters (Fig. 20), and therefore should not be considered as representative of the total volcano's SO_2 budget.

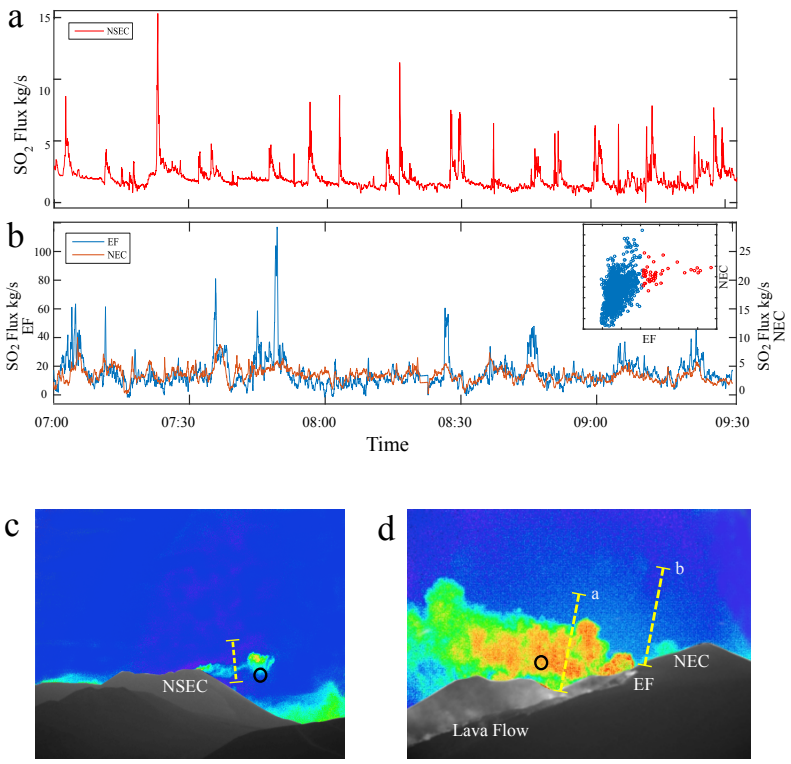

Figure 20 (a) an example of 4 hour-long so2 flux time-series of the nsec, taken from uv3 (from 9th july, 2014). A representative pseudo-color image of the plume, demonstrating the cameras' field of view, is shown in (c). The largest (> 5 kg/s) so2 flux pulses correspond to strombolian explosions; (b) an example of 2.5 hour-long acquisitions from uv4 (14th august, 2014). The plumes of both the nec and the eruptive fracture (ef) were simultaneously contained in the cameras' field of view (see pseudo-color image in (d)). From this, the so2 flux contributions from the two distinct gas sources were resolved from ica time-series obtain along two different plume's cross sections (dashed yellow lines in fig. 20b), one (labeled "j") relative to so2 flux contributions from the nec only, and the other (labeled "i") corresponding to gas contributions from nec+ef. This procedure contributed two so2 flux time-series (in which the ef flux was calculated as difference between the ef+nec flux and the nec flux) that exhibited a high level of temporal coherence (see scatter plot in the inset). Since the so2 flux oscillations at the ef are 5-10 higher than at the nec, we consider unlikely that the correlation between the two time series are an effect of our calculation routine. In both pseudo-color images (c, e), the empty circles indicate the fvo of the spectrometer used for camera calibration

Our SO_2 flux dataset was integrated with seismic and infrasonic data recorded by the permanent networks run by the Istituto Nazionale di Geofisica e Vulcanologia, Osservatorio Etneo (INGV-OE). Seismic stations used to investigate volcanic tremor are equipped with broadband (40 s corner period), three-component Nanometrics^{TM} Trillium seismometers acquiring at a sampling rate of 100 Hz (Fig. 18). Seismic amplitudes were obtained by calculating RMS (root-mean square) envelope over 1-minute-long non-overlapping time windows at ECNE (Fig. 20b) and ECPN stations (Fig. 20a). The infrasonic permanent

network, in 2014, was made up of 9 stations, 3 equipped with Monacor condenser microphones (sensitivity of 80mV/Pa in the 1-20 Hz infrasonic band) and the others with G.R.A.S.S. 40AN microphones (sensitivity of 50mV/Pa and flat response in the 0.3–20,000 Hz band). In order to investigate eruption dynamics and the inter-connection between craters involved in the 2014 summer eruption, we located volcanic tremor and infrasound events extracted from the continuous signal (*Di Grazia et al*., 2006; *Patanè et al.,* 2008; *Cannata et al.,* 2011b and 2013).

Volcanic activity was recorded by video-surveillance camera network of INGV-OE (www.ct.ingv.it/en/webcam-etna-en.html) operating both in visible (with standard and 5MP video resolutions) and thermal (LWIR) bands. Cameras located at La Montagnola, in the same shelter hosting UV3 camera, and Mt. Cagliato on the middle eastern flank at about 7 km from the summit area, were able to record any change of the eruptive activity occurred in the summer 2014.

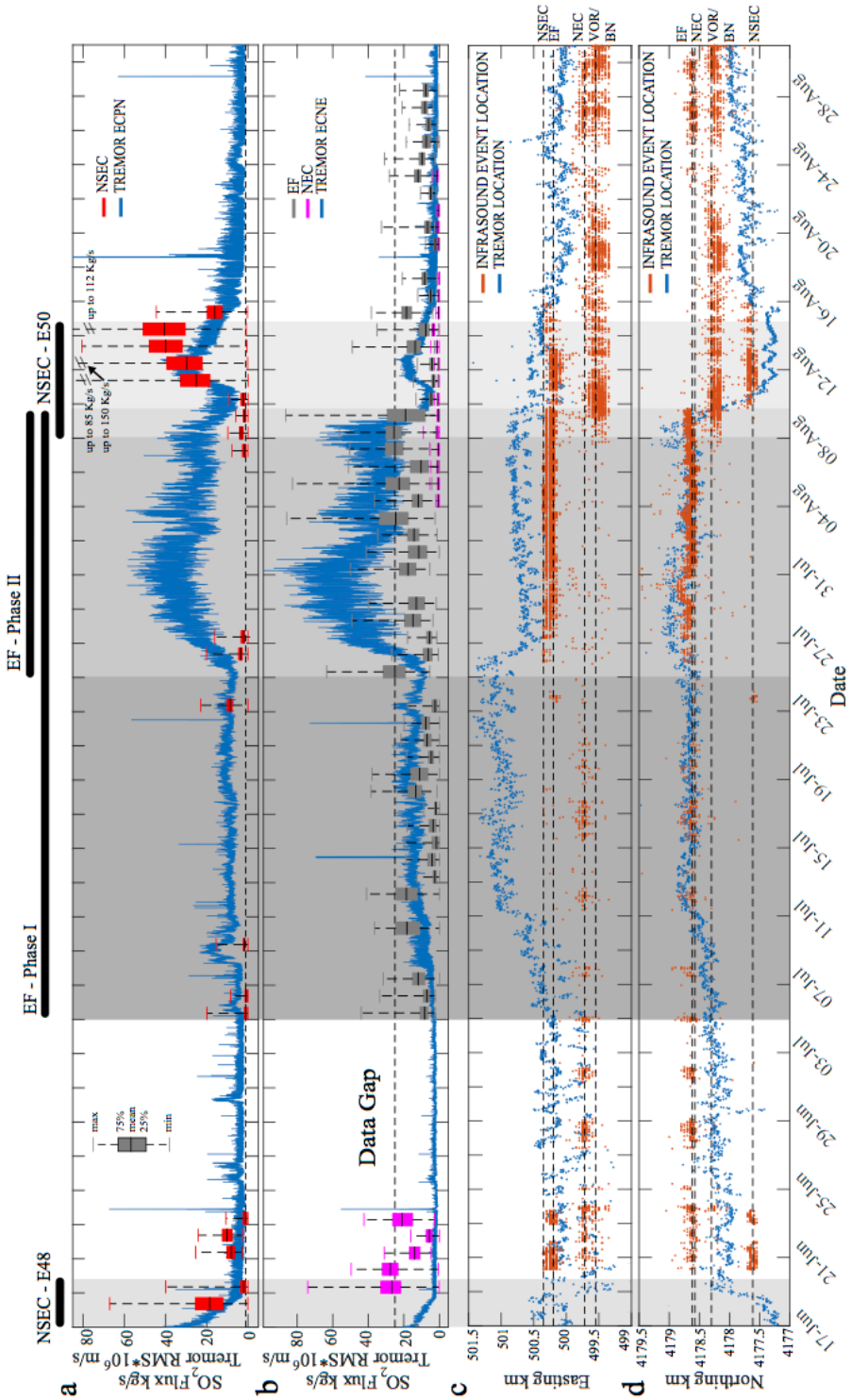

*Figure 21 temporal record (june 17th – august 31st) of so2 flux emissions from (a) the nsec and (b) the nec and the july-august 2014 eruptive fissure (ef). For each measurement day and degassing vent, the vertical bars show mean, minimum (min), maximum (max) and inter-quartile (25-75%) range of the so2 flux. The blue-colored lines stand for volcanic tremor amplitude (rms*106) from recorded at ecpn (in a) and ecne (in b) stations (see fig. 1 for their location). The locations of the centroid of volcanic tremor (blue) and infrasound events (red) are shown in (c), highlighting activity switch between different sources/vents. Centroids of the volcanic tremor sources were obtained by means of a grid-search location method based on spatial amplitude distribution of seismic signal filtered in the frequency band 0.5-5.5 hz (for details see di grazia et al., 2006; patanè et al., 2008; cannata et al., 2013). In order to locate infrasound event sources we applied a grid-search method based on the composite use of semblance and brightness functions (see cannata et al., 2011b, 2013 for details). On the upper side, solid bars mark the eruptive activity of ncse (episodes e48 and e50 in de beni et al., 2015) and two phases of ef.*

4.2.2 Volcanic activity

The SO_2 flux observations we report on in this work were taken between June 17Th () and August 31st, 2014, when both UV3 and UV4 systems were operating (Fig. 21). This temporal window encompasses two eruptive episodes of the NSEC, in June 14th-18th (therefore only partially covered by our measurements) and August 8th-15th. The first episode, referred as E48 in *De Beni et al.* [2015], started with a one month-long prelude phase, in which mild strombolian activity with weak ash emissions increased in frequency/intensity. This was followed by a four days-long paroxysmal phase, with intense strombolian explosions to lava fountaining that formed lava flow travelling on the cone's eastern flank toward the Valle del Bove (Fig. 21) (www.ct.ingv.it; and *De Beni et al.* [2015]). After three days of scanty explosions from NSEC and two weeks without any summit activity, an Eruptive Fissure (EF) opened in the Valle del Leone (the upper side of Valle del Bove) on the east flank of the NEC (Fig. 21). According to *De Beni et al.* [2015], the EF activity was fed by a NW-SE-trending fractures system, departing from the NSEC (Fig. 21) The EF eruption consisted of two phases (I: July 5th-25th; II: July 25th-August 10th) that occurred from two distinct, but closely-spaced vents, at 3000m and 3090m elevation, respectively (Fig. 21) Both phases were characterized by emplacement of a compound lava flow field that covered a wide area of the Valle del Leone, during a strong spattering/strombolian activity at the vents, that were particularly intense during Phase II. The EF activity gradually vanished during August 8th-10th, in tandem with resuming of activity at the NSEC (episode E50). On late August 10th strombolian explosions became intense forming the first lava flow. The paroxysmal phase occurred on August 11th-15th, when lava fountaining fed both an ash-rich plume and a vigorous lava flow travelling toward the northern side of the Valle del Bove.

4.2.3 Results

Figure 22 shows examples of two 4h-long UV camera acquisitions from (a) UV3 and (b) UV4. The plots demonstrate the usual structure of high-rate (~1Hz) Etna's SO_2 flux time-series, characterized by the repetition (periods of 10s to 1000s of seconds) of small-amplitude (< 5 kg/s) gas flux oscillations - produced by emission of distinct gas pulses, or "puffs" (*Tamburello et al. 2013*). Super-imposed on this "puffing" degassing style are, at both the NSEC (Fig. 22) and EF (Fig. 22), stronger (> 5 kg/s) SO_2 pulsations, typically lasting tens of seconds to minutes, and corresponding to individual strombolian explosions or, more frequently, sequences of closely spaced strombolian events (Fig. 22)

In the attempt to explore the temporal evolution of degassing behavior at each target, we calculated, for each measurement day and crater, the mean SO_2 flux value and the inter-quartile ranges. We remind our mean daily values are in fact representative of only 6 hours of observations. These exhibited large variations during our 10-week observation period observation period (Fig. 21).

The NSEC (Fig. 21a) contributed little to the total SO_2 budget during most part of the observational period, and was characterized by SO_2 emission below the instrumental detection limit (<1 kg/s) during its periods of quiescence. In contrast, the NSEC was the strongest SO_2 source (among those analyzed here) during its August 11th-15th eruptive episode, with mean SO_2 fluxes of 16.0 to 44.4 kg/s, and a peak emission of 150 kg/s during the major (paroxysmal) eruptive phases on 13th August. In the same August 11th-15th interval, source locations of both seismic tremor and infrasound events (Fig. 21c) confirm that eruptive/degassing activity was concentrating at the NSEC. Interestingly enough, the NSEC SO_2 emissions were also detectable (range, 2-20 kg/s) between 5th-9th July (see example in fig. 20a) and 23rd-27th July (e.g., at onset of both eruptive episodes of the July 2014 EF); and, even more importantly, in the days (August 7th-10th) prior to the NSEC paroxysmal activity (of August 11th-15th). These pre-paroxysmal gas detections at the NSEC were accompanied by a concomitant shift in seismic tremor centroid and infrasound event locations, from the EF toward NSEC, during August 9th-10th (Fig. 20c).

The SO_2 degassing regime of the EF (Fig. 21b) was clearly captured by our network since eruption onset on July the 5th. The daily means of the EF SO_2 flux ranged from 2.1 to 26.6, and daily peak emissions varied from 11.5 to 86.4 kg/s. SO_2 emissions were typically higher during episode II (July 25th – August 10th) than in episode I (July 5th-25th), in agreement with distinct volcanic tremor RMS amplitudes (Fig. 21a, b). The initial phases of EF activity were accompanied by a weak and gradual increase of seismic amplitude, and a migration of volcanic tremor centroids, from central craters towards EF area (Fig. 21c). In contrast, more evident amplitude variations occurred on July 25th (start of EF phase II), when RMS amplitude sharply increased (Figure 21a,b). Intense explosive activity at EF during phase II (July 25th – August 10th), is revealed by infrasound events, which had sources located in the area of EF (Fig. 21c). Notably, the EF SO_2 emissions attenuated on August 10th, just one day before eruptive activity switched to the NSEC (Fig. 22).

SO_2 degassing at the NEC (Fig. 21b) was substantially reduced (daily means of 1.2-4.2 kg/s) during the EF activity, at least compared to the pre-eruptive period (e.g., end of June; daily means: 5.7-27.7 kg/s; peak SO_2 fluxes: 16.1-75 kg/s). After opening of the EF on July

5th, the NEC contributed only ~20% of and EF+NEC flux. Yet notwithstanding, daily records (e.g., Fig. 20b) systematically showed a high level of coherence (e.g., simultaneous gas variations) between the two gas sources (EF and NEC) throughout the entire eruption duration.

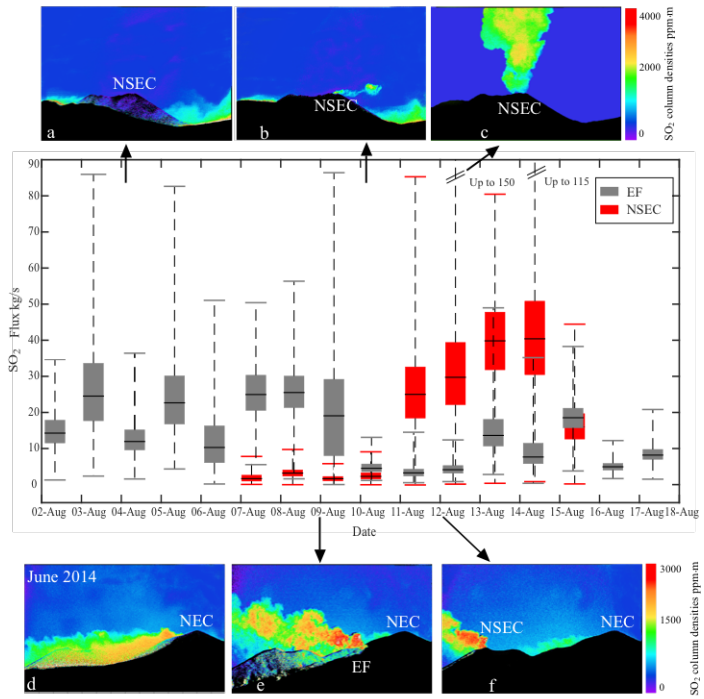

Figure 22 detail (august 2nd – august 18th) of so_2 flux time-series from the nsec and ef, demonstrating activity switch on august 10-11. The paroxysmal nsec activity (august 11-15) was preceded by 4 consecutive days of precursory mild (but detectable) so_2 emissions.

4.2.4 Discussion

UV cameras contribute SO_2 flux time-series of unprecedented-high spatial and temporal resolution, and therefore open the way to investigating novel aspects of volcano degassing regime. At Etna, a >30 year-long SO_2 flux record is available from use of the COrrelation SPECtrometer (COSPEC) (*Caltabiano et al.*, 1994; 2004) and, more recently, from continuous UV scanning spectrometers of the FLAME network (*Salerno et al.*, 2009) using the DOAS technique (*Galle et al.*, 2003). In contrast to such distal (> 5 km from degassing vents) "bulk plume" measurements, near-vent observations of individual crater's SO_2 flux have remained very sporadic and limited in number (*Aiuppa et al.*, 2008, 2011; *La Spina et al.*, 2010). The Etna's four summit craters have diverse degassing/erupting behaviors, and often exhibit fast (timescales of hours/days) transitions in activity style, with frequent switches from one vent to another (see section 2 and (*Allard et al.,* 2006)). As such, vent-

resolved SO_2 flux measurements are needed to fully interpreting, and eventually predicting, the volcano behavior.

Our study here attempts at a systematic characterization of SO_2 emissions from Etna's individual craters/eruptive vents. While we admit that gas emissions from Etna's central craters (BN and VOR, see Fig. 19) do also require careful scrutiny, we here specifically target gas emissions from the eastern side of the volcanic summit (Fig. 19), where eruptions have been clustering since 2004 (www.ct.ingv.it and *Branca and Del Carlo,* [2005]; *Behncke et al* [*2006, 2014*]) .

The summer 2014 example shows that SO_2 emissions from an eruptive fissure can successfully be monitored over time using UV cameras (Fig. 21b). The daily averaged SO_2 emissions from the 2014 EF eruption ranged between 2.1 to 26.6 kg/s and, if extrapolated over the entire eruption duration (≈ 36 days), imply a cumulative released SO_2 mass of 50,000 tons. This corresponds to ≈30 % of the total SO_2 mass released by Etna during the same temporal interval (considering an average total SO_2 flux of ≈3000 tons/day in July-August 2014, as measured by the FLAME network of INGV-OE; www.ct.ingv.it). We conclude that, during eruptive periods, active degassing at the fissures contributes a non-marginal fraction of the volcano's total SO_2 budget. This result has typically been difficult to prove from traditional spectroscopic observations made from distal locations (*Caltabiano et al.* 2004), where volatiles contributed from a single fissure are dispersed within the "bulk plume", and mixed with volatiles derived from the summit craters.

SO_2 emissions from the NEC virtually ceased during the 2014 EF activity (Fig. 21b). A data acquisition gap (from 23th June to July 5th) prevents us from establishing the exact timing of the SO_2 drop at NEC. Still, no SO_2 emission was detected from the NEC during most part of the EF eruptive episode (until August 5th), and the SO_2 flux was detectable but low (≤4.2 kg/s) until late August. We interpret the drastic reduction of the NEC SO_2 emissions, combined with the temporal coherence observed in the NEC and EF time-series (Fig. 20b), as an evidence for the two systems being structurally connected. We propose that opening of the EF in early July drained magma/gas normally circulating in the NEC feeding conduit system. Interestingly, a similar link between the NEC conduit system and an eruptive fissure was proposed (based on geophysical data) by *Sciotto et al.* [2013] for the 2008-2009 eruption, which insisted in similar area (*Bonaccorso et al*., 2011).

The appearance of SO_2 at the NSEC, in concomitance with onset of both EF eruptive phases (Fig. 21a), suggests structural link between these two systems as well. We propose a mechanism in which the EF eruption was triggered by magma intrusion along NW-SE

trending dyke, irradiating from the NEC, and which fracture system eventually intersected the NSEC plumbing system (Fig. 19b). The centroids of seismic tremor, located at about 2.5-3 km a.s.l., suggest dyke intrusion propagated at very shallow depth. Some level of structural inter-connection between EF and NSEC is also supported by Figure 22, where degassing activity at the former is seen to vanish (on August 10^{th}) as the latter re-actives (during August 11^{th} -16^{th}). This activity switch, evident in the gas record (Fig. 22), is also captured as rapid shift in the centroid of seismic tremor and infrasound event locations, from the EF area towards NSEC crater (Fig. 21c). We caution that, while a connection between EF and NEC/NSEC conduits is supported by our SO_2 and volcanic tremor data, additional (independent) evidence for this hydraulic link needs to be established. We cannot rule out that our observations merely reflect ascent of gas, rather than magma, through interconnected chimneys opening as the Etna's upper plumbing system pressurizes.

Our observations also allow characterizing the SO_2 degassing behavior of the Etna's NSEC (Figs. 21a and 22). This pyroclastic cone, developed over a series of collapse pits formed on the eastern flank of the SEC cone during 2004-2009, has shown an unusually fast growth and eruptive rate in 2011-2014. Fifty eruptive episodes, including lava fountaining episodes, strombolian activity, lava flows have been recognized at NSEC by *Behncke et al*., [2014] and *De Beni et al*. [2015], making this crater the current largest source of volcanic hazard on the volcano (*Spampinato et al.*, 2015). No gas flux information has been reported for the NSEC until this study. We show here that the NSEC exhibits no detectable SO_2 flux (< 1 kg/s) during quiescence, but becomes a substantial source of gas (with peak emissions up to 150 kg/s) during its paroxysmal eruptive phases (Figs. 21a, 22). Importantly, low but detectable (2-3 kg/s) SO_2 flux emissions from the NSEC were detected for four consecutive days (August 7^{th}-10^{th}) prior to onset of the paroxysmal phase (of August 11^{th}-15^{th}) (Fig. 22). Such pre-paroxysm gas detections at the NSEC appear to anticipate the shift in volcanic tremor centroid and infrasound event location, from the EF toward NSEC, which were clearly visible only on August 9^{th}-10^{th} (Fig. 21c). Our gas observations are promising, but more work is needed to understand their implications for a robust, gas-based early-warning system of NSEC eruptions.

4.2.5 Conclusions

In this work, we took advantage of the high spatial (~5 m) and temporal (~1 Hz) resolution of the UV camera to systematically investigate SO_2 gas emissions from Etna's individual vents. Our vent-resolved SO_2 flux time-series suggest rapid (hours/days) switch in degassing activity from one active vent to another, that imply a geometry of the Etna's shallow plumbing system with interconnections between summit vents (NEC and NSEC) and with (EF) summit eruptive fissure.

We find that the 2014 EF contributed a substantial (~30%) fraction of the total volcano SO_2 budget, and altered the usual magma/gas circulation in the summit craters' shallow feeding conduits. The SO_2 emissions from the NEC were, consequently, strongly reduced. Our SO_2 flux records also indicate that the NSEC contributed little or no gas to the quiescent Etna's emissions in summer 2014. SO_2 degassing activity reactivated at the NSEC in the days prior to its eruptions, and intensified as volcanic activity escalated toward paroxysmal phases. We conclude UV cameras open new prospects for identifying short-term gas flux variations prior to paroxysmal Etna eruptions.

Chapter 5
Results: Etna 2015

5.1 Degassing processes during the Etna's December 2015 paroxysmal sequence[2]

Open-vent mafic volcanoes on Earth are one of the most persistent and spectacular forms of active volcanism of our planet (Rose et al., 2013). Apart from being prodigious sources of magmatic volatiles to the Earth's atmosphere during passive (quiescent) degassing (Shinohara et al., 2013; Carn et al., 2017), these basaltic volcanoes are also the most frequently erupting (Siebert et al., 2010). Although their eruptions are most commonly effusive in nature, explosive paroxysmal eruptions do also periodically occur, ranging in size and intensity from Hawaiian-Strombolian (Volcanic Explosivity Index, VEI: 1-2) to Plinian (VEI: 5-6) in the most extreme events (Williams, 1983; Coltelli et al., 1998; Houghton et al., 2004; Pérez et al., 2009).

Magmatic volatiles play a central role in the generation of these basaltic paroxysms (e.g., Aiuppa et al., 2010). However, in contrast to quiescent emissions that are relatively easy to quantify (e.g., Allard et al., 2016), measuring the gas output from paroxysmal basaltic explosions is challenged by the high ash content of eruptive clouds (that hampers measurement from ground), and the relatively low eruptive column heights (a few km), complicating the use of satellites. As such, magmatic gas budgets for basaltic paroxysms are often only indirectly quantified, e.g., from knowledge of eruption magnitude and pre-eruptive volatile contents (from melt inclusions) (e.g., Roggensack et al., 1997).

[2] Article to be submitted on Frontiers in Earth Science, section Volcanology

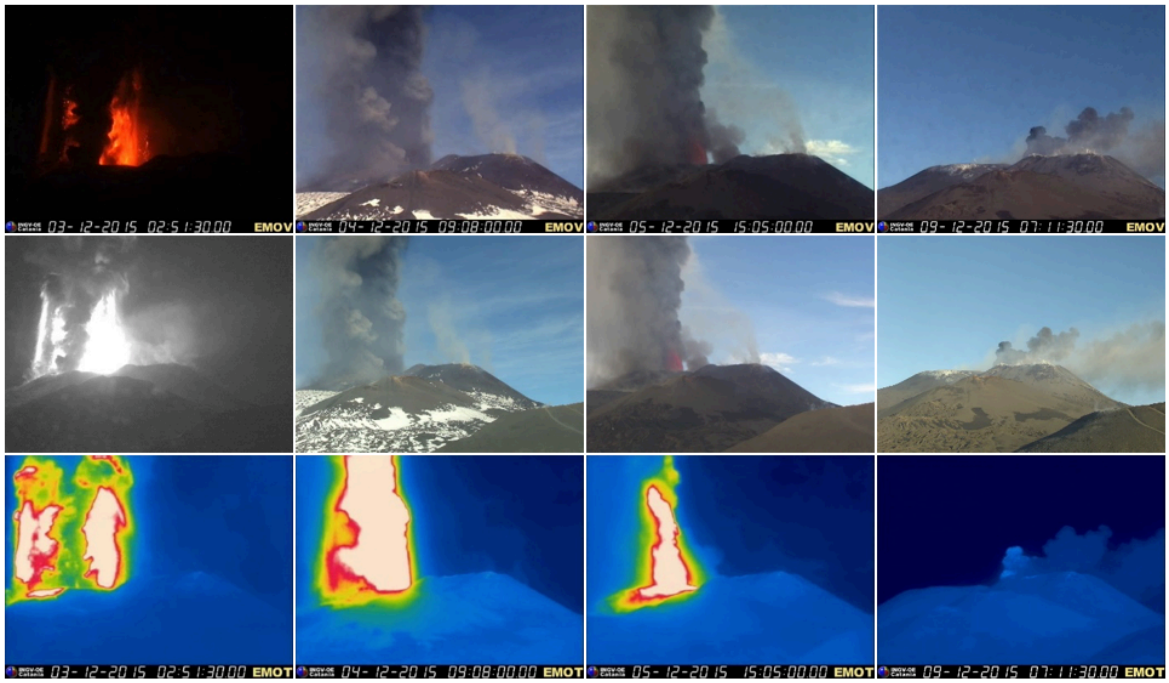

Figure 23 visible (upper and middle panels) and thermal (bottom panel) images of etna's paroxysmal activity from vor on december 3,4,5 (phase 4), and strombolian activity from the nsec (december 9; phase 5). All images taken from the ingv-oe montagnola multi-parametric station (see fig. 2 for location), using (from top to bottom) emov, emhd and emot cameras

Some of the most frequent and violent basaltic paroxysmal explosions in nature occur on Mt. Etna volcano, in Sicily (southern Italy; Fig. 24). Since the late 1990s, roughly ~200 paroxysmal explosive events have occurred at Mt. Etna, frequently clustered in cycles of discrete lava fountaining events initially at the Southeast crater (SEC) (during 1996-2008; Allard et al., 2006; Behncke et al., 2006; Bonaccorso et al., 2011) and at the New Southeast crater (NSEC) afterward (2011-present; Behncke et al., 2014; de Beni et al., 2015) (. 24).

These paroxysmal events are exceptionally well characterized in terms of eruptive dynamics (Harris and Neri, 2002; Dubosclard et al., 2004; Andronico and Corsaro, 2011; Scollo et al., 2012) and composition, texture and volume of erupted materials (Corsaro and Pompilio, 2004; Polacci et al., 2006; Kahl et al., 2015). Interpretation of their associated geophysical signals has led to increasingly refined models for their source region and triggering mechanisms (Alparone et al., 2003; Calvari et al., 2011; Patanè et al., 2013; Bonaccorso et al., 2013, 2014; Spampinato et al., 2015; Gambino et al., 2016). The composition of magmatic gases in the co-eruptive clouds has also been measured occasionally (Allard et al., 2005; La Spina et al., 2015). However, the gas output (gas flux and total emitted gas volume) of individual paroxysms has been more difficult to characterize. While it is well established that Etna's SO_2 flux peaks (typically at >10,000 tons/day) during paroxysmal episodes (Caltabiano et al., 2004; Spampinato et al., 2015), the

explosive gas output from the erupting crater has proven difficult to resolve from the background quiescent emissions that persist at the other craters. This is because traditional spectroscopic techniques (COSPEC and scanning DOAS) have typically targeted a distal plume (several km away from the summit area), where the two gas contributions (from the paroxysm and passive degassing) have merged into a single aggregate plume (Salerno et al., 2009).

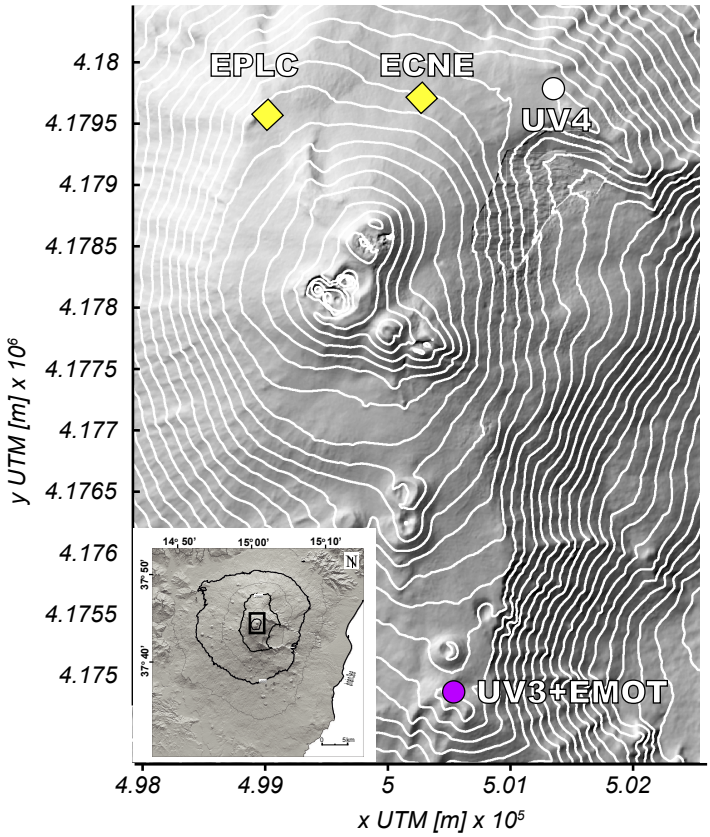

Figure 24 Map of the Mt. Etna area showing the active summit craters and the location of the instruments used in this work. Results from EPLC and ECNE, part of the INGV-OE monitoring network, were used to generate the seismic tremor

Recently, we demonstrated the use of a novel network of UV cameras to obtain spatially resolved SO_2 flux emission data from individual Etna's craters (D'Aleo et al., 2016). The high temporal and spatial resolution of UV cameras enables the gas emissions from distinct emission sources (craters) to be resolved, for example our measurements of the SO_2 flux signature from Etna's NSEC prior to, during and after its paroxysmal phase during 11–15 August, 2014.

Here, we extend this previous work to characterize SO_2 degassing processes at Etna during its late 2015 paroxysmal phase (Fig. 23). The paroxysmal sequence lasted from 3-18 December and has been described by Vulpiani et al. (2016), Corsaro et al. (2017), Pompilio et al. (2017) and Bonaccorso and Calvari (2017). Although the eruption was composed of individual lava fountain episodes similar in duration (~1-2h), magnitude (~10^9-10^{10} kg of

erupted tephra) and fountain height (~1-4 km) to previous Etna's events, it is also exceptional for (i) the unusually rapid progression of eruptive episodes, with 4 violent lava fountain events in <2 days; (ii) the eruptive ash column reaching up to 12-15 km height; (iii) the nearly simultaneous reactivation of several summit craters; and particularly (iv) the first paroxysmal events at the Voragine crater (VOR) in more than a decade. This crater, although the oldest of those presently active on Etna (being the remnant of the 19th-mid 20th century Central Crater; Chester et al., 1985), has remained poorly active (aside from strong gas emissions) since the intense 1998-1999 activity that included a sub-plinian explosion on 22 July 1998 (Aloisi et al., 2002). Our UV camera measurements in 2015 thus offer the opportunity to characterize the SO_2 degassing budget of Voragine paroxysmal explosion(s) for the first time. To this aim, our UV camera results are also combined with complementary satellite-based observations of the explosive SO_2 release during the paroxysm(s), obtained from the Ozone Monitoring Instrument (OMI; Levelt et al., 2006, 2017), and with thermal radiance measurements obtained by a network of ground based thermal cameras operated by INGV-OE (Coltelli et al., 2017) and infrared satellite images acquired by the Moderate Resolution Imaging Spectroradiometer (MODIS) (Wright et al., 2002, 2004, 2008; Rothery et al., 2005; Coppola et al., 2013, 2016). Using multiple ground- and satellite-based sensors in concert, we aim to fully quantify pre- syn- and post-paroxysmal SO_2 emissions, as well as the degassing magma volumes required to source these emissions. We compare our degassing magma volumes with the volume of pyroclastic materials and lavas erupted throughout the paroxysmal sequence.

5.2 Material and methods

5.2.1 Etna's paroxysmal activity in 2015

Etna has remained relatively quiet between June and mid October 2015, in what we refer to as *Phase 1* of quiescence, background activity. Mild intra-crateric explosive activity finally resumed inside the VOR crater since October 19 (Corsaro et al., 2017), with strombolian activity increasing in vigor until November 30 (*Phase 2*). A further escalation in strombolian activity during December 1-2 (*Phase 3*) was precursory to onset of vigorous paroxysmal sequence, characterized by the rapid succession of four individual lava fountain episodes at VOR in only three days (December 3-5; *Phase 4*) (Fig. 23). The lava fountain eruption parameters for the 4 episodes are described in Bonaccorso and Calvari (2017) and Pompilio et al (2017). According to these results, the paroxysmal episodes lasted 65-114

minutes and produced 680-1740m high lava fountains topped by 12.5-15 km high ash-rich convective clouds. The most energetic lava fountain was episode I on the night of December 3, having peak mass discharge rate of ~6 kg/s. Each episode produced think lava fountain-fed rheomorphic lavas filling the CCs, and a lapilli-ash tephra deposit along the volcano's flanks. On December 6, after a few hours of quiescence, *Phase 5* started with switching of volcanic activity toward the NSEC. *Phase 5* was characterized by with intense strombolian activity and effusive activity in the Valle del Bove (~ 2 Mm^3 of lava released) during December 6-9 (Fig. 23), followed by waning eruptive activity during December 9-18 (Corsaro et al., 2017).

5.2.2 SO_2 fluxes: UV cameras

Etna's volcanic SO_2 flux was measured from ground using a permanent network of 2 stand-alone UV cameras run by University of Palermo (D'Aleo et al., 2016). These camera systems have been operational since 2014 and are located at Montagnola (UV3) and Pizzi Deneri Observatory (UV4)

The 2015 UV camera dataset is unfortunately not continuous. Due to logistical challenges (e.g. very high snow cover and extremely low temperatures in winter), the UV4 camera system is only maintained during summer-early autumn; the NEC SO_2 flux dataset thus only extends from mid-June to mid-October 2015. The UV3 camera system sits in a robust housing (a hut containing several multi-parametric instruments from INGV-OE). However, technical problems (including icing of the outer quartz window and un-sticking of the optical lenses from the cameras during quick temperature changes) together the frequent cloud cover over the volcano's summit resulted in non-continuous SO_2 flux measurements for the Central Craters (VOR + Bocca Nuova) and the NSEC. Although many of these technical issues have now been solved, the 2015 dataset demonstrates the challenges in maintaining a permanent UV camera system on a high-altitude volcano with occasionally extreme meteorological conditions.

5.2.3 Satellite-based SO_2 observations from OMI

The Ozone Monitoring Instrument (OMI) is a hyperspectral ultraviolet/visible spectrometer carried aboard the NASA satellite Aura (Levelt et al., 2006, 2017). OMI is one of several UV sensors used in monitoring global atmospheric SO_2 concentrations, but it is arguably the most sensitive and effective, offering good spatial resolution (13 x 24 km at

nadir), a wide spectral range (270-500 nm, with resolution of 0.45 nm) and contiguous daily coverage of the Earth. These factors are particularly beneficial in the daily monitoring of volcanic SO_2 emissions, both during eruptions and in the intervals of passive degassing that may separate eruptions, and numerous studies have exploited OMI data for long-term studies of volcanic degassing at individual volcanoes and on a global basis (e.g. McCormick et al., 2012, 2015; Flower and Carn, 2015; Flower et al., 2016; Fioletov et al., 2016; Carn et al., 2008, 2013, 2017). Recently, a new SO_2 retrieval algorithm using a principal component analysis technique has been developed that dramatically reduces the noise in the OMI SO_2 data (Li et al., 2017). A new dataset, optimised for the study of volcanic emissions, and designated OMSO2VOLCANO is publicly available from the NASA Goddard Earth Sciences (GES) Data and Information Services Center (DISC; http://disc.sci.gsfc.nasa.gov/Aura/data-holdings/OMI/omso2_v003.ht- -ml). SO_2 column amounts are provided for a set of SO_2 vertical profiles, distributed around a centre of mass altitude (CMA). We use the lower tropospheric SO_2 data (CMA of 3km) for the interval before the onset of the paroxysmal eruption, and either middle troposphere (CMA of 8 km) or lower stratospheric data (CMA of 18 km) throughout the paroxysm, based on auxiliary plume height data. OMI data can be analysed using OMIplot, a collection of bespoke software routines written in IDL (Carn, 2015).

Here, we use OMI observations to compute a time-series of daily SO_2 mass loading over Etna for the paroxysmal interval in December 2015, and several months of preceding activity. The pixels in each OMI instantaneous field-of-view (IFOV, or "scene") that contain SO_2 are identified and the column concentration of SO_2 in each pixel, reported in DU, is combined with pixel area and converted to a mass. We obtain a total scene mass loading by summing the mass of all SO_2 pixels, and the resulting quantity is typically taken to be the daily SO_2 mass released by the volcano, since OMI makes one daily overpass of each point on the Earth's surface. Under certain conditions, e.g. low winds-peed or slow SO_2 loss rates, it is possible that OMI could observe newly-emitted SO_2 in addition to relict SO_2 emitted on preceding days. In this study, we consider this unlikely to be a significant problem: local wind speeds at Etna plume altitudes (roughly, 4 to 10 km) are sufficiently high—usually >10 m/s based on NCEP2 Reanalysis Data (Palma, 2013)—to carry SO_2 rapidly downwind, which we tend to see in SO_2 imagery (e.g. drifting plumes can be tracked downwind in consecutive OMI orbits). Moreover, the emissions that concern us in this study are mostly restricted to the free troposphere and as such would tend to have lifetime on the order of 1-2 days particularly for particle-rich volcanic plumes (Eatough et al., 1994; Oppenheimer et

al., 1998; Faloona, 2009). To be certain of only including fresh SO_2 in our daily mass loadings calculations, we examine each OMI scene manually, and compute separate mass loading for discrete drifting SO_2 clouds within each image.

The temporal information required to convert SO_2 mass loadings to emission rates is usually unavailable, since the satellite obtains an instantaneous snapshot of activity at the time of overpass. Where high quality atmospheric wind speeds and estimates of SO_2 lifetime are available, mass loadings can be converted into emission rates (e.g. Lopez et al., 2013, Carn et al., 2013) though some of these methods require particular plume geometries to be successful. In this study, we favour the use of daily mass loadings rather than drawing on auxiliary data to compute emission rates from OMI observations, particularly because the key interval of interest for the satellite observations is the paroxysmal period of late November and early December 2017, where plume geometries are unfavourable for emission rate calculations, and the pulsatory nature of the paroxysmal eruption and emissions are not necessarily well-represented by emission rates averaged to tons per day.

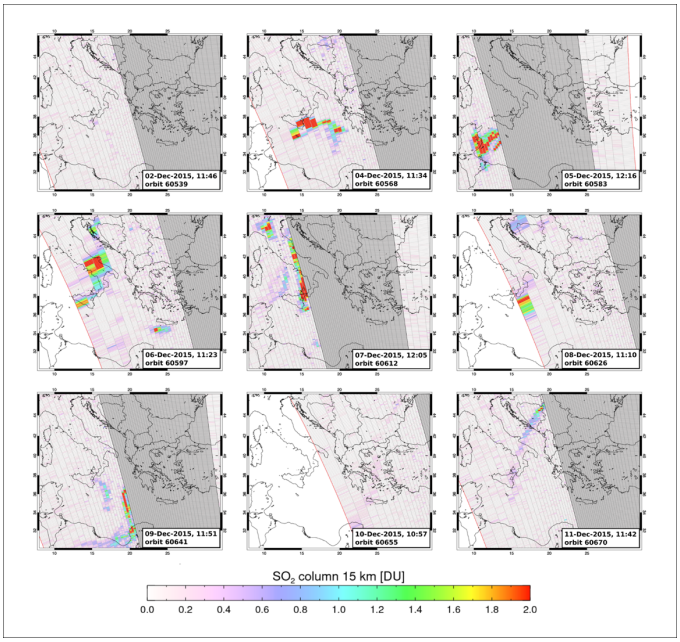

Figure 25 individual omi scenes for the paroxysmal period, showing so2 column concentration in dobson units (i.e. The number of molecules in a square centimeter of atmosphere. If all of the sulphur dioxide in a column of the atmosphere was compressed into a flat layer at standard temperature and pressure, one dobson unit would be 0.01 mm thick and would contain 0.0285 g of so2 per square meter). Omi swath edges are shown by thin red lines, and the pixels within the swath are shown with their true geometries. Rows affected by the omi row anomaly are highlighted in grey.

Our reported daily mass loadings should be considered as minima, given the influence of the OMI Row Anomaly (ORA, Carn et al., 2016; Flower et al., 2016). Since 2009, certain rows of the OMI swath have been rendered unusable due to a blockage in the instrument's field of view. This obscures parts of the plume, leading to an underestimate, and on certain days the affected rows may be located squarely across a target volcano and the downwind

dispersal area, obscuring the entirety of the plume. In practice this means that SO_2 mass loadings may be underestimated on certain days, and moreover that gaps of 2-3 days between OMI observations are now not uncommon. Another potential problem in the use of tropospheric SO_2 data is meteorological cloud cover obscuring lower altitude volcanic plumes. We include a time-series of mean scene reflectivity (Fig. 26) here as a proxy for cloud cover during the OMI observations, and filtered out pixels where cloud fraction (computed from reflectivity exceeds 30%). Relative to tropical volcanoes, cloud cover is anticipated to be a much less significant problem at Etna and based on the reflectivity time series is not considered likely to majorly impact our results.

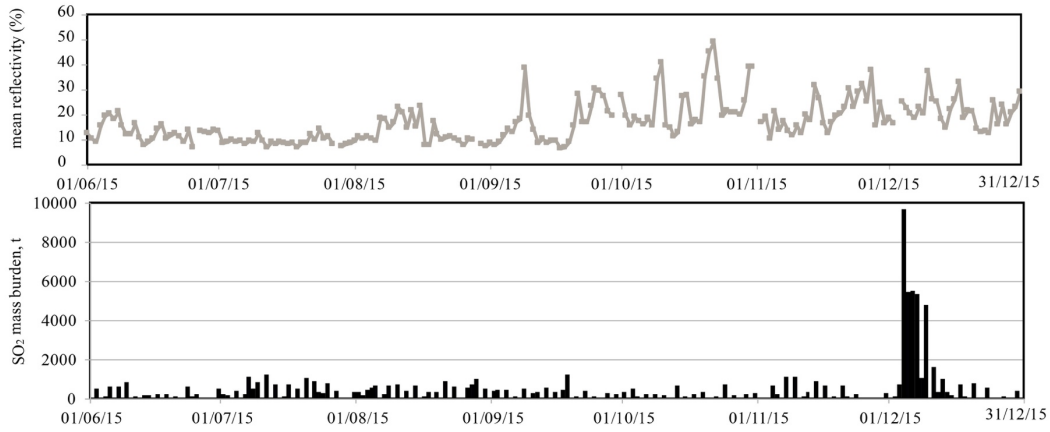

Figure 26– Time series of (a) mean reflectivity (in %) and (b) the daily SO2 mass burden (in tons) measured by OMI

5.2.4 Satellite-based thermal data

Thermal data acquired by MODIS were analyzed using the automated, near real time volcanic hot-spot detection system MIROVA (Coppola et al., 2016; www.mirovaweb.it). MIROVA uses middle infrared radiance (MIR) measured by the two MODIS sensors, carried on Terra and Aqua NASA's satellites, respectively. These satellites, scanning the Earth surface four times per day, allow monitoring of volcanic activity globally on a daily basis (Wright et al., 2002, 2004, 2008; Rothery et al., 2005; Coppola et al., 2013, 2016).

The hot-spot detection algorithm is designed to detect small to large-scale thermal anomalies (from < 1 MW to >40 GW), and thus capture a large variety of volcanic activity (Coppola et al., 2013, 2016). Starting from hot spot pixels detected by MIROVA, we use the Wooster et al. (2003) formulation to retrieve the volcanic radiant power (VRP, W):

$$VRP = 1.89 \times 107 \times (L_{MIR} - L_{MIRbk}) \qquad \text{(eq. 6)}$$

where L_{MIR} and L_{MIRbk} are the MIR radiances ($W \cdot m^{-2} \cdot sr^{-1} \cdot \mu m^{-1}$) characterizing the single hot spot pixel and the background. The coefficient 1.89×10^7 ($m^2 \cdot sr \cdot \mu m$) was obtained from best-fit regression analysis (Wooster et al., 2003), and allows estimating VRP (±30%) from hot surfaces ranging in temperature between 600 and 1500 K.

5.2.5 Ground-based thermal data

Volcanic activity at Mt. Etna is continuously monitored by INGV-OE using a network of video-surveillance cameras located on the southern, eastern and western flanks of the volcano (Andò and Pecora 2006). The INGV-OE Mt. Etna's camera network consists of five thermal cameras and nine visible cameras that allow continuous, real-time ground-based imaging of volcano activity (Andò and Pecora, 2006; Behncke et al., 2006, 2009). In this study, we use data recorded by EMOT, EMOV and EMHD cameras, all hosted at La Montagnola Multi-parametric Station, 3 km SE from the vent (Fig. 24). These cameras provided the best quality information and images (Fig. 23) during the 3–9 December paroxysmal sequence. Images acquired by thee cameras are sent to a receiver in Catania through microwave, WiFi, 2 GHz video transmitter and/or cable. All images are digitized and archived on computers in AVI format, with each video clip representing 5 min.

EMOT is equipped with an A320 M Flir Thermovision camera, recording in the 7.5 and 13 μm spectral range, and providing 320 × 240 pixel images with a spatial resolution of 1.3 mrad. The camera has a thermal sensitivity of 70 mK at 30°C, and 80 mK at 25°C, respectively. Thermal images are converted on board the camera to output the peak temperature found in a region of interest, centered on the zone affected by eruptive activity. This value is transmitted at 1 Hz to the acquisition center in Nicolosi. Thermal images and thermal data, recorded between 0 and 500°C, are processed in real-time by a dedicated software (NewSaraterm) developed with LabVIEWTM 8.0 to detect ash-rich eruptive columns, explosive and effusive activity (Behncke et al., 2009). This software calculates, with a median filter, the daily thermal offset and extracts for each measurement the difference between the measured value and the dynamic thermal offset. NewSaraterm is set to transmit alert messages to the INGV-OE Operative Center anytime when prefigured thresholds are exceeded. Temperatures displayed in the video frames are much lower than the true temperatures at the target, because of the distance between the camera location and the target (the summit craters), environmental factors such as air humidity, pressure, air

temperature, and the presence of an additional protective lens on the camera (Sawyer and Burton, 2006). The temperatures discussed here are thus apparent, not absolute, as they have not been corrected for the aforementioned factors and are measured in Arbitrary Units (A.U.).

5.3 Results

5.3.1 UV camera-based SO_2 fluxes

Figure 27 shows examples of SO_2 flux records (30 minutes each) taken by the UV camera network in 3 distinct measurement days: (a) 14 July, (b) 2 December, and (c) 6 December. Figure 28 illustrates the SO_2 observations made by UV camera during paroxysmal activity on December 4. These examples are selected to illustrate some of the characteristics of our SO_2 flux measurements but cannot be taken as an exhaustive representation of the highly variable degassing behaviours seen at Etna's different vents during the monitored period.

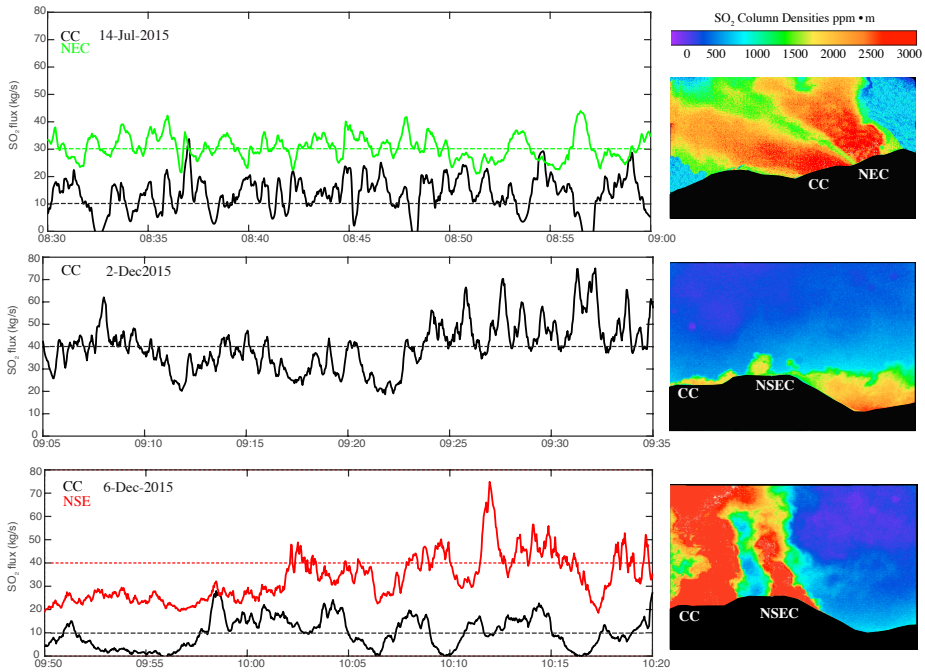

Figure 27 examples of so_2 flux records (30 minutes each) taken by the uv camera network in 3 distinct measurement days. The horizontal dashed lines indicate the mean so_2 flux values. For each time-series (measurement day), a snapshot of a representative absorbance image (outputted by the camera system) is also shown to illustrate typical plume geometries. Upper panel, 14 july results obtained from uv4; middle panel, 2 december results obtained from uv3; bottom panel, 6 december results obtained from uv3.

The 14 July dataset (Fig. 27a) is taken as representative of background, quiescent degassing activity during *Phase 1* (see section 2.1). Both time-series and image show that, during *Phase 1*, the NEC was the dominant gas source on the volcano, the CCs were moderately degassing, while the NSEC was essentially producing no gas. The December 2

observations illustrate a visible acceleration in SO_2 degassing from the CCs in *Phase 3*, as a prelude to the ensuing paroxysmal sequence which started only a few hours later.

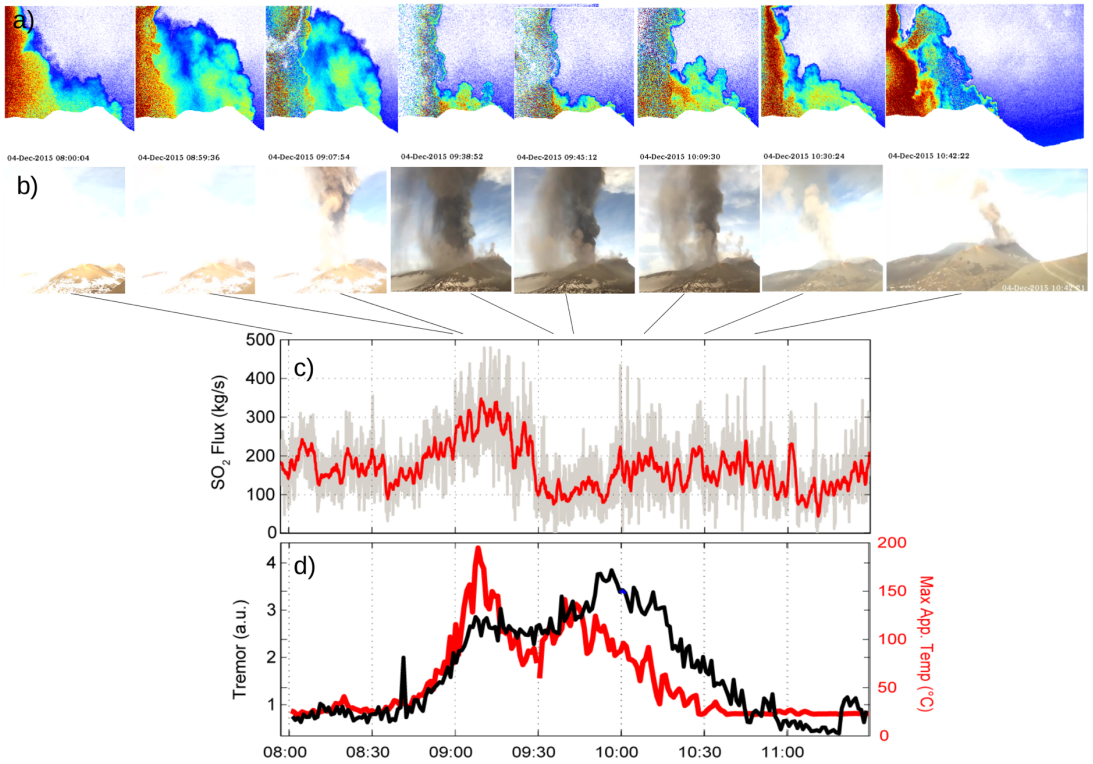

Figure 28 4th december paroxysm. SO_2 flux, tremor and thermal signal are plotted. On the top visible image and uv camera, absorbance, image.

Paroxysmal activity from VOR during *Phase 4* was only captured in the morning of December 4 (Fig. 28). The three other VOR paroxysms occurred during night-time (episodes I and III on December 3 and 4, respectively) or during daytime but outside the UV3 operational time window (episodes IV on December 5). Our example thus corresponds to the second lava fountaining event of VOR (episode II: from 08:41 to 10:03 of December 4). The pseudo-colour images in the top panel of Fig. 28 illustrate the 2D distribution of SO_2 in the basal (gas thrust) portion of the eruptive cloud. These figures show a dense, tall SO_2-rich plume rapidly dispersing to the left of the camera's FOV (toward S-SW). Based on comparison with OMI data (see below), we are confident that, in the basal portion of the eruptive column (just right above the crater rim), where our integration cross-section is taken to derive the SO_2 fluxes, the largest fraction of the plume is still captured in the camera's FOV. Our December 4 time-series (third panel Fig. 28) demonstrates high SO_2 fluxes (>100 kg/s) in the 40 minutes before the paroxysm onset (08:41 L.T.). After the onset, the SO_2 flux progressively increases, in parallel with an escalation in thermal activity and seismic tremor, and peaks at >300 kg/s at ~09:10 L.T. The subsequent drop in SO_2 flux and apparent temperature between ~09:30 and ~09:50 L.T. is caused by the elevated ash content in the

plume (see stills from visible video footage, second panel Fig. 28), precluding accurate retrieval of SO_2 (note degradation of pseudo-color images, Fig. 28). After ~10:00 L.T., the SO_2 flux oscillated around high (~150 kg/s) values during the paroxysm's waning phase.

A typical dataset for a *Phase 5* measurement day (December 6) shows increased degassing from the erupting NSEC crater, and continued vigorous degassing from the Central Craters (Fig. 27).

In the attempt to characterize Etna's SO_2 degassing behaviour in the ~6 months temporal window culminating in the December 2015 paroxysmal sequence, we calculate, for each available measurement day, the daily averaged SO_2 flux, by simply taking the arithmetic mean of data in each 5 hour-long daily acquisition (same as examples given in Figs. 27 and 28). Results are illustrated in the synoptic temporal plot of Figure 29, which also summarizes the results of satellite-based SO_2 (Fig. 29d) and thermal (Fig. 29e) observations.

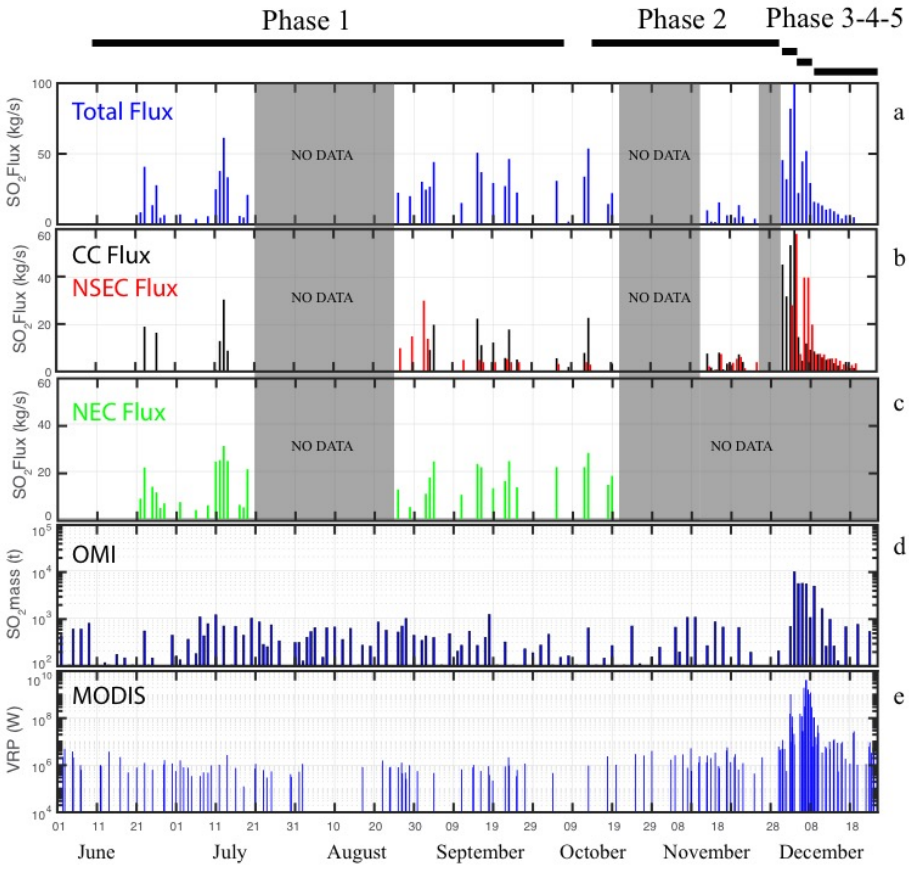

Figure 29 temporal record of the monitored gas and thermal data, june-december 2015. The upper panel (a) is the daily averaged total so₂ flux from etna, calculated from the summation of daily averaged so₂ flux contributions from the cc and nsec (panel b) and the nec (panel c). Note that the total fluxes are under-estimate since mid-october 2015, when the uv4 camera system was dismantled for the winter and the nec contribution is thus not accounted for. It is also worth to remind that our daily averages are calculated from 5 hours of daily observations only. Panel (d) shows the temporal record of the daily so₂ mass loadings captured by omi, while panel (e) is a temporal plot of the modis-derived volcanic radiant rower (vrp), calculated by the mirova system. In all plots, note the visible escalation in so₂ degassing and thermal regime in phase 4-5 (3-9 december), followed by a vanishing coda in mid- to late-december.

In spite of the several data gaps, caused by adverse weather conditions and technical problems (see Section 2.2.), the ground-based SO_2 flux time-series (Fig. 29a-c) documents the temporal evolution of Etna's degassing activity, as indicated by changes in the Total SO_2 flux (Fig. 29a) and in the vent-resolved SO_2 flux contributions from NEC, NSEC and CC (VOR+BN) (Fig. 29b-c). We find that, in *phase I* (July-October) the Total (NEC+CC+NSEC) SO_2 flux oscillates around a ~30 kg/s average, with the NEC (mean, ~52%) and the CC (mean, ~40%) being the primary SO_2 sources and the NSEC contributing only ~8% of the gas on average. The CC SO_2 flux systematically remains < 30 kg/s (Fig. 29b). *Phase 2* (19 October-30 November), characterized by resumed strombolian activity at VOR is unfortunately very poorly covered by our observations (note that, from *Phase 2* onward, the Total SO_2 flux accounts for the contribution of CC+ NSEC only, because UV4 was no longer operative, meaning that NEC emissions were not quantified). Corsaro et al., (2017), based on results of the INGV-OE permanent scanning-DOAS network (Salerno et al., 2009), report a SO_2 flux increases to 30-50 kg/s during this phase of escalating strombolian activity at VOR. Intensification of eruptive-degassing activity at VOR is well consistent with our UV camera records for *Phase 3* (1-2 December; 45 and 32 kg/s, respectively; see Fig. 29b and 30b). No appreciable SO_2 is detected at the NSEC in the meanwhile (Fig. 30c). The onset of paroxysmal activity at VOR, *Phase 4* (3-5 December), marks a sizeable increase in the CC (53-103 kg/s), NSEC (30-58 kg/s) and Total (~82-160 kg/s) SO_2 flux (Fig. 30). It is useful to recall that, since only episode II (December 4 morning paroxysm; Fig. 28) matches with the UV camera acquisition interval, the SO_2 increases on December 3 and 5 reflect heightened degassing in between the paroxysms themselves. During December 6-8, the onset of *Phase 5*, volcanic activity switched from VOR to NSEC (see Section 2.1) as illustrated by increased SO_2 fluxes at NSEC (up to 40 kg/s, and by an abrupt decline of VOR SO_2 emissions (compare Figs. 27b and 27c). An exponential decay of SO_2 emissions from all craters is observed in the waning phase of the paroxysmal sequence (10-18 December) (Figs 29 and 30).

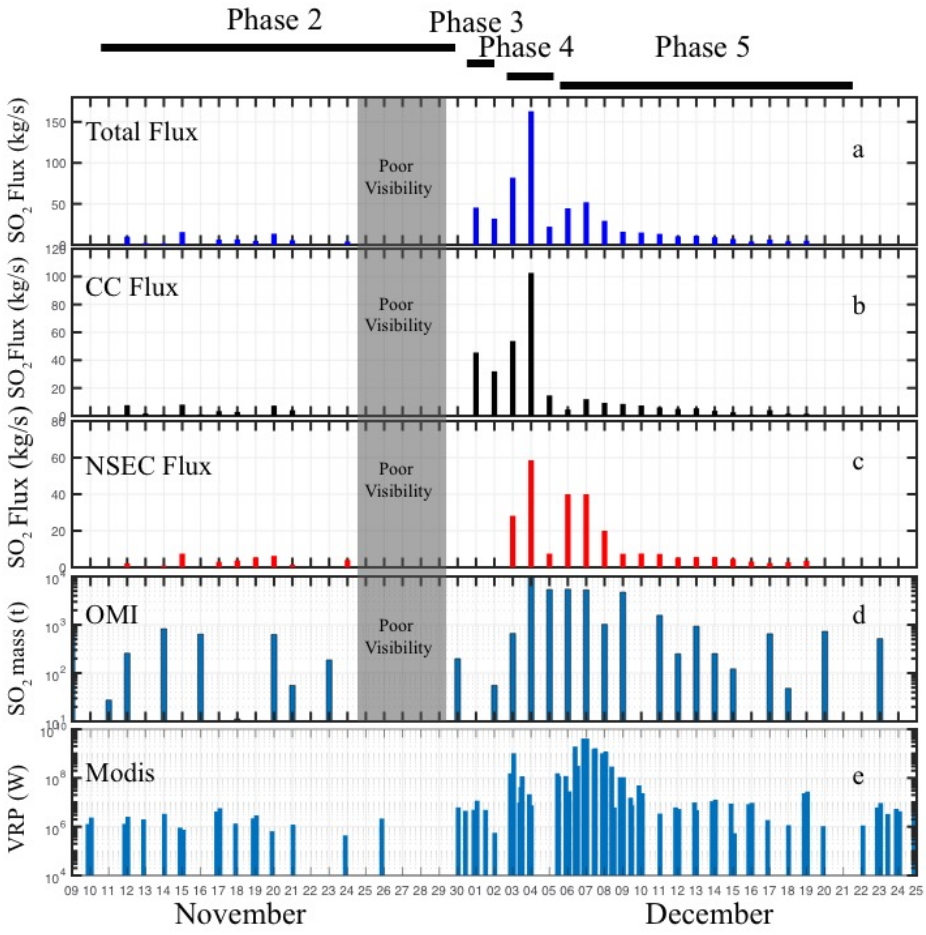

Figure 30 a detail of figure 29, showing the temporal evolution of gas and thermal signals in november-december 2015.

5.3.2 OMI-based SO_2 observations

Example of SO_2 mass loading maps on OMI scene from some selected days are shown in Figure 25. The OMI-derived daily SO_2 mass loading over Etna varies widely during *Phases* 1-3, but remains systematically below 1200 tons (Fig. 29d). The wide range observed (from <100 to ~1200 tons) is likely to reflect daily variations in the passive degassing flux from Etna, but also variations in OMI's detection of the prevailing low-altitude and low mass SO_2 clouds during this period of lower intensity activity. Increases in daily cloud cover or in the position of the ORA-affected portion of OMI's swath relative to Etna can both hamper accurate quantification of SO_2 mass and small plumes during lower intensity volcanic activity suffer disproportionately. That OMI did not observe SO_2 mass greater than 1200 t in any overpass reflects the general low level activity of Etna during this passive degassing interval.

Onset of the *Phase 4* paroxysmal activity marks a sizeable increase in daily SO_2 mass loading on December 4 (~9600 tons), indicating substantial SO_2 injection in the higher atmosphere during the first two more vigorous VOR episodes. SO_2 mass loading persists at high levels (~5300 tons) over the next three consecutive days (5-7 December). During *Phase 5*, the high SO_2 mass loading on December 9 reflects degassing from the erupting NSEC, but declines to pre-paroxysm levels (< 1000 tons) by December 12.

5.3.3 Satellite thermal data

Between 01 July and 31 December 2015, 145 thermal anomalies are detected over Mt. Etna by the MODIS-MIROVA system (Coppola et al., 2016) (Figs. 29e and 30a). The radiant heat flux spans from 0.15 MW to 4151 MW (on 7 December 2015) with about 80% of the data below 10 MW (Fig. 31b). Visual inspection of all the images allows us to discard thermal anomalies due to fires (located at more than 5 km from the summit), as well as to filter out thermal data affected by cloud/plume contamination or acquired under poor geometrical conditions (satellite zenith angle > 45°). The resulting dataset consists of 101 alerts (red line in Fig. 31a), yielding a total radiant energy of 5.22×10^{14} J over the analysed time window.

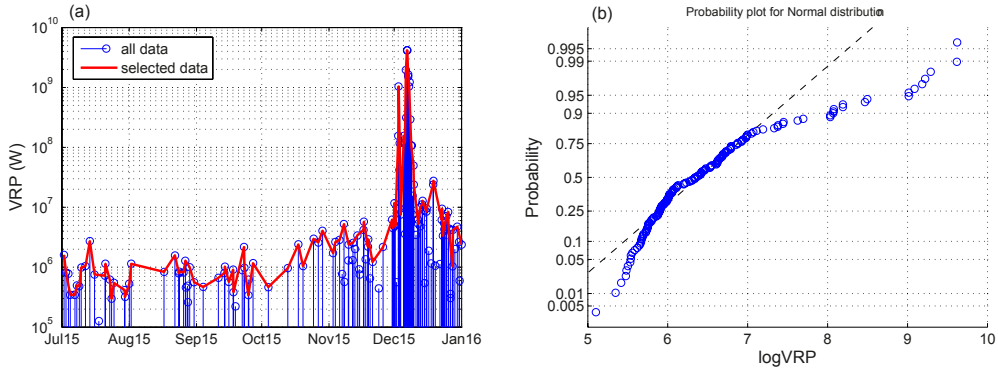

Figure 31 time series of volcanic radiant power (vrp) detected by modis-mirova system over etna volcano between july and december 2015. (b) probability plot of log-transformed vrp (all data).

Between July and late September, during *Phase 1*, the radiant power is very low and relatively stable at around 1 MW (Fig. 31a). However, thermal anomalies increase gradually during late October-November (*Phase 2*), to reach 5 MW, on 28 October 28, and 11 MW on 11 November 2015. On December 2 (*Phase 3*) at 21:00 (UTC), a sharp VRP increase at 155 MW coincides with the first VOR paroxysmal episode. The paroxysm itself generates a peak VRP of 1037 MW on 3 December at 01:15 (UTC). In the following 2 days, the volcanic plume often obscures and attenuates thermal anomalies, thus precluding clear view

observations of paroxysmal episodes 2-4. From December 6 (*Phase 5*), a new phase of increased thermal activity was detected by MIROVA, in response to lava effusion from the base of the NSEC. This phase is accompanied by a clear view of the Etna's summit area, and culminated on 7 December (00:50 UTC) with VRP reaching the maximum value of 4151 MW (Fig. 31a). Cessation of lava effusive activity in the evening of December 8 is marked by a VRP decline below 100 MW (Figs. 29e and 31a). Thermal anomalies progressively declined throughout the following days, dropping to 3 MW by 31 December 2015.

5.4 Discussion

Our gas and thermal observations (Figs. 29, 30, 31) contribute novel constraints on degassing processes associated with the Etna's December 2015 paroxysmal sequence. We show that, in the two days before onset of the paroxysmal sequence (in *Phase 3*), SO_2 degassing intensifies at the VOR (up to 40 kg/s, Fig. 30). The SO_2 flux results presented in Corsaro et al (2017) imply that this SO_2 flux increase (~30-50 kg/s) persisted during *Phase 2* too (19 October-30 November), and therefore accompanied the entire sequence of escalating strombolian activity at VOR that occurred prior to the paroxysms. The onset of paroxysmal activity at VOR on 3 December saw a further escalation in UV camera-derived SO_2 fluxes, and is also marked by an abrupt increase in OMI-derived SO_2 loadings over Etna (Figs. 29, 30) and in radiant power (Fig. 29). This anomalous SO_2 output and thermal regime persisted throughout the entire VOR (*Phase 4*) and NSEC (*Phase 5*) paroxysmal sequence, and then slowly decreased after 10 December, with SO_2 and thermal emissions decaying to pre-paroxysm values by the end of the month. The heightened SO_2 degassing behavior of Etna in December 2015 is clearly illustrated by the plot of Figure 30, which shows the cumulative masses of degassed SO_2 derived from both ground- (UV Camera) and space-based (OMI) observations. This plot enables us to quantify the total volume of gas associated with Etna's 2015 paroxysmal sequence, and to reconstruct the associated degassing magma budget.

5.4.1 SO_2 release in Etna's 2015 paroxysmal sequence

The time-averaged SO_2 flux from Etna is exceptionally well characterized (Caltabiano et al., 1994, 2004; Allard, 1997; Allard et al., 2006), and is known to be dominated by persistent passive degassing from the summit craters. In contrast, the SO_2 flux sustained by the brief but very intense paroxysmal episodes is poorly characterized. This paroxysmal SO_2 flux is likely to constitute only a small fraction of the long-term total emission budget, but –

quantifying the paroxysmal flu would nonetheless have profound implications for constraining the dynamics and trigger mechanisms of the paroxysms.

Our 4 December 2015 dataset (Fig. 28) is, to the best of our knowledge, the first example of an high-frequency (1 Hz) SO_2 flux record during paroxysmal episode at Etna (VOR episode II). This dataset demonstrates both advantages and challenges in UV camera sensing of basaltic paroxysmal activities. Our results show a massive SO_2 release during Etna's paroxysmal activity, peaking at ~400 kg/s in the most intense phase between 09:00 and 09:30. Temporal SO_2 flux fluctuations broadly correlated with seismic tremor and thermal amplitude (Fig. 28), but are also modulated by ash content, with SO_2 fluxes declining (and being underestimated by an unknown but certainly significant extent) during ash-rich periods where plume opacity increases. In the VOR episode II example, rapid dispersion of the eruptive cloud toward S-SW is an additional issue, and implies that only part of the column is contained in the cameras' FOV (this effect is minimized by taking the integration cross-section right at the crater rim edge, where the majority of the plume is captured). With these limitations in mind, we calculate by integration that 1220 tons of SO_2 was explosively released during less than 2 hours of vigorous VOR episode II. To put this context, this SO_2 mass corresponds to what normally released by the volcano in one full day of background quiescent activity (e.g., *Phase 1* in 2015).

In a typical Etna lava fountain, SO_2 comprises ~0.8±0.3 mol. % of the gas phase (Allard et al., 2005; La Spina et al., 2015). From this and the paroxysmal SO_2 mass of 1220 tons (above), we estimate the total magmatic gas output for VOR episode II to be $8 \cdot 10^8$ m^3 (assuming T = 1100 °C, P = 0.1 MPa, and molecular weight of ~20.9 g/mol for a 90 mol. % H_2O gas composition; La Spina et al., 2015). For comparison, Bonaccorso and Calvari (2017) calculated, based on processing of thermal camera images, a total fluid volume for this event of the same order of magnitude ($1.5 \cdot 10^9$ m^3 of total fluid, with pyroclastic materials accounting for a trivial fraction of this volume, ~0.2 %).

The three other VOR episodes (I, III and IV; cfr. 2.1) unfortunately occurred outside the daily UV camera acquisition hours, so that their volatile budget cannot be constrained from measurements on ground. The elevated SO_2 fluxes observed on December 3 and 5 (Fig. 30), therefore, are reflecting heightened quiescent (or weakly explosive) degassing in the periods between one paroxysmal episode and the successive.

We therefore place constraint on the total explosive SO_2 release during the entire VOR sequence by using OMI record, which clearly peaks during *Phase 4* (Figs. 30, 31). These are likely to fully capture eruptive gas emissions injected into the higher atmosphere, while

being less sensitive to Etna's low-altitude quiescent emissions (we consider the average daily SO_2 mass loading of ~500 tons in July-October 2015 as representative of these background emissions) (see *4.3*). By summing up the SO_2 mass loadings seen by OMI during December 3-6, we find a cumulative SO_2 mass of ~21,000 tons (Fig. 30, Table 1). Thus, using a total eruptive mass of ~21,000 tons and the parameters as above for the composition and T-P conditions of the eruptive plume, we infer the total magmatic gas output for the entire Phase 4 (VOR episodes I-V) at $1.4 \cdot 10^{10}$ m^3. This is in the same order of magnitude of (a factor ~2 higher than) the total calculated erupted volume of fluid of Bonaccorso and Calvari (2017) ($5.9 \cdot 10^9$ m^3). Given the impact of the row anomaly on OMI mass burden measurements, this is likely to be a minimum estimate for the total gas output of Phase 4.

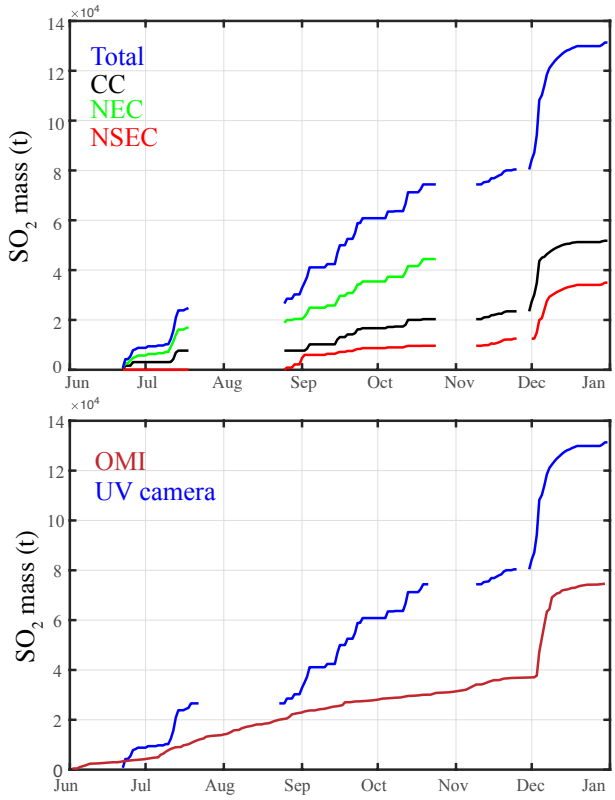

Figure 32 cumulative plot of uv camera-based so_2 masses (in tons), calculated by summing –up the daily so_2 fluxes of figures 26a-c. (d) comparison between camera-based and omi-based cumulative so_2 masses. The cumulative omi so_2 masses are obtained from summation of the daily so_2 mass loadings of figure 26d. The camera-based so_2 cumulative trend exceeds the omi trend in phases 1-3, implying this latter method underestimates quiescent, low-altitude so_2 emission plumes. The two independently obtained cumulative so_2 masses are reasonable similar during the paroxysmal sequence of phases 4-5 (see tab. 1)

A similar approach can be used to quantify the SO_2 degassing budget for the NSEC activity of *Phase 5* (Tab. 1). Although OMI observes a composite plume from Etna, and cannot by itself distinguish the relative contributions of the distinct summit craters, the decrease in Central Crater flux measured by our UV camera network in Phase 5 gives us confidence that the SO_2 mass dings measured by OMI are dominated by NSEC emissions.

Using OMI data, we calculate that ~11,000 tons of SO_2 may have been explosively released by the NSEC during 6-9 December, from which we estimate (at same composition, temperature and pressure as above) a total magmatic gas output of ~$7.2 \cdot 10^9$ m^3, or ~2 times less than during *Phase 4*. Again, given the influence of the ORA obscuring part of the plume detected by OMI, this is likely to be a minimum estimate of gas output.

5.4.2 Magma volume fluxes from SO_2 fluxes

One equally important exercise is to use the above inferred erupted SO_2 masses to calculate the volumes of degassing magmas required to produce them. In order to convert the SO_2 masses (M_{SO_2}) into volumes of magma (V_e) needed to justify them, we use the same relation as in Allard (1997):

$$V_e = \frac{M_{SO_2}}{2[S] \cdot \rho \cdot (1-x)} \quad \text{(eq. 6)}$$

where [S] is the weight fraction of elemental sulfur degassed per unit mass of magma (3000 mg/kg, from glass inclusion record; Métrich et al., 2004), ρ is typical basalt density (2700 kg/m^3) and *x* is magma crystallinity (0.3; see Pompilio et al., 2017).

Using equation (2) and OMI-based SO_2 masses, we find that a degassing magma volume of only ~1.9 Mm^3 (Tab. 1) is required to justify SO_2 emissions during VOR activity (*Phase 4*). This is well below the erupted pyroclastic volume for 3-5 December, for which available estimates range between 5.1 Mm^3 (Vulpiani et al., 2016; Pompilio et al., 2017), 7.1-7.2 Mm^3 (Corsaro et al., 2017; Neri et al., 2017) and 12 Mm^3 (Bonaccorso and Calvari, 2017) (Tab. 1). We interpret this mismatch as an evidence for that only a small fraction (8-33 %) of the erupted magma was actually emplaced above the SO_2 degassing depth (~ 3 km below the summit; Spilliaert et al., 2006) *during* the VOR paroxysm(s). Rather, we argue that a large (77-92 %) fraction of the erupted magma was already degassed (SO_2-poor) at the time of the paroxysm(s), likely because it had remained stored in the shallow (< 3 km) VOR conduit for days before the paroxysm. This interpretation is well consistent with textural and compositional features of *Phase 4* ash particles (Pompilio et al., 2017), whose heterogeneity indicates coexistence in the VOR conduit of variably degassed/crystalline/viscous magma volumes that had been emplaced somewhere between hours to several days before. We calculate that, at the average magma shallow emplacement rate of 0.2-0.4 Mm^3/day (implicit in the SO_2 flux release of 30-50 kg/s in *Phases 2-3*) (Tab. 1), 9 to 45 days would have been required to accumulate in the VOR conduits the missing magma volume (the difference between the erupted and the syn-eruptive degassing magma). This 9-45 day interval is

consistent with the total duration of the VOR activity observed from 19 October (43 days in total).

We conclude that the VOR paroxysmal phase in December 2015 is likely driven by progressive re-mobilization and eruption of degassed conduit magma, emplaced days to even >1 month before the onset of eruption. The ascent of fresh magma, perhaps corresponding with our syn-paroxysm ~1.9 Mm^3 magma volume, is the most likely trigger for destabilization of resident conduit magma, as invoked on completely independent basis by Pompilio et al., (2017). We finally argue that this mechanism may not be exclusive to the VOR paroxysmal sequence in 2015. For instance, a similar mismatch was observed for the ensuing NSEC activity between the co-paroxysmal degassing magma volume (~0.6 Mm^3) and the erupted (~2 Mm^3) magma volume (Tab. 1).

5.4.3 UV camera vs. OMI

Our 2015 dataset also allows testing the level of agreement between ground-based and satellite-derived SO_2 emission observations (Fig. 32). Inter-comparison studies between ground- and satellite-based measurements of SO_2 emissions are relatively sparse, and due to differences in sensitivity to SO_2 and the spatial/temporal duration and resolution of each measurement type, strong quantitative agreement is limited to certain ideal cases, e.g. estimates of long-term emissions budgets where short-term variability of SO_2 fluxes are suppressed (Carn et al., 2017).

In our specific Etna example, we caution that direct comparison between UV camera and OMI datasets is challenging, since the two measurement types target volcanic SO_2 emissions on distinct temporal/spatial timescales and good quantitative correlation is therefore unlikely. UV camera SO_2 measurements have very high temporal/spatial resolution, but observations are limited to only 5 hours per day. Whether or not these 5 hours of observations can confidently be extrapolated to quantify the total SO_2 mass degassed in a daily – to become then comparable to the daily SO_2 mass loadings delivered by OMI - depends on how dynamic and changeable the volcano's activity state is. While the operation is probably relatively safe in "calm" days of quiescent degassing (e.g., our *Phase 1*), it becomes more problematic when the volcano behavior changes dramatically within a day, as during the *Phase 4-5* paroxysmal sequence. For example, measurements taken on December 4 encompass 2 hours of intense fountaining and vigorous degassing that raise the mean SO_2 flux at 160±17 kg/s. This, if extrapolated over the entire measurement day, would lead to a daily output of ~14,000 tons, exceeding the OMI SO_2 mass measured on the following day

(~5,400 tons). In contrast, on December 3 and 5, the paroxysmal episodes occurred outside the UV camera measurement interval. Since the UV-derived mean fluxes (respectively, ~82 and ~22 kg/s) thus miss the paroxysmal gas contributions, their extrapolated masses (7080 and 1917 tons) do likely under-estimate the real daily SO_2 output, and are unsurprisingly lower than the OMI-derived mass loading (10,000 and 5,500 tons for December 3 and 5, respectively). We thus find it more prudent to use OMI data for calculation of total eruptive gas masses (see Section 4.1) and degassing magma volumes (see Section 4.2). Still, we note that eruptive gas masses and degassing magma volumes obtained from UV Camera data for *Phase 4* are remarkably close (Tab. 1), implying that the above discussed effects cancel out over the entire paroxysmal sequence (3 days).

On the other hand, our results suggest OMI may under-estimate more sluggish SO_2 quiescent emissions, at least in the conditions of our *Phase 1-2* (see Fig. 32). Over the 3 months period covered by *Phase 1*, for example, the cumulative mass loadings derived from OMI are nearly one order of magnitude lower than those measured on ground from the UV camera (Tab. 1). The sensitivity of ultraviolet satellite observations to atmospheric SO_2 are strongly altitude dependent, and underestimates of SO_2 mass loadings are relatively common for lower tropospheric plumes due to higher SO_2 detection limits (e.g. McCormick et al., 2012, Carn et al., 2013).

We conclude that ground-based and satellite-based SO_2 flux observations are complementary in monitoring basaltic volcanoes. While UV-camera measurements are more effective in monitoring quiescent emissions, and perhaps more useful to capture pre-paroxysm escalation in degassing activity (see our *Phase 3* and results in Corsaro et al., 2017), satellites become invaluable during paroxysmal explosive eruptions. On the long-term (timescales of several months), the SO_2 degassing histories registered by the two independent monitoring tools show similar overall trends (Fig. 32).

5.4.4 Magma volume fluxes from satellite thermal data

Satellite thermal IR data also potentially offer the opportunity to quantify the volumes of magma involved in the paroxysmal sequence. The conversion between thermal and volumetric fluxes is based on the observed relationships between effusion rates and active lava flow areas (see Harris and Baloga (2009) for a review). Various approaches have been proposed to adapt this methodology to satellite thermal data (i.e., Harris et al., 1998; Wright et al., 2001; Coppola et al., 2013), all aimed at calibration of a simple linear relationship

between space-based radiant flux (for example the VRP) and the Time Averaged lava Discharge Rate (TADR).

The relationship can be written as:

$$TADR = VRP / c_{rad} \qquad \text{(eq. 7)}$$

where c_{rad} is a conversion coefficient empirically calculated (e.g. Coppola et al., 2013) or based on cooling models of active lava flows (e.g. Harris et al., 2007).

Here we used the values for c_{rad} calibrated during previous effusive eruptions of Mt. Etna (Coppola et al., 2013; Coppola et al., 2016), that indicate a range between $2 \cdot 10^8$ J/m^3 and $3.6 \cdot 10^8$ J/m^3. According to equation (7), these two values allow us to estimate a maximum and minimum TADR, and consequently a range of erupted lava volumes. This methodology provides results in excellent agreement with field estimates (cf. Harris et al., 2007; Harris et al., 2011) and, once calibrated (as for at Etna), it allows us to assess erupted volume within ±30% uncertainty (Coppola et al., 2016, 2017).

On the other hand, it is important to highlight some limitations and assumptions of the thermal proxy, if applied to periods that include different types of volcanic activity (such as at Etna in late 2015):

1) A volume calculated using the thermal approach is based on the implicit assumption that the heat flux is generated by an active lava flow (cf. Coppola et al., 2013). Consequently, the model breaks down when the lava is not extruded but instead retained in the vent, as in the case of lava lakes or open-vent activity. In such circumstances, the thermal proxy provides a minimum estimate of the magma circulation (convection) at very shallow depth, rather than effusion rates, as long as the top of the magma column is sufficiently shallow to produce thermal anomalies on the surface (Werner et al., 2017);

2) The coefficient c_{rad} is expressly calibrated for effusive (lava-flow-forming) eruptions (Coppola et al., 2016), and it does not necessarily work during explosive eruptions (i.e. paroxysms). During explosive eruptions, the heat flux detected by satellite is sourced by the lava fountains themselves and by the accumulation of intra-crateric material forming reomorphic lava bodies. In these cases, the relationship between erupted volumes and thermal energy is strongly altered by the complexity of the mixed heat source (lava fountains and reomorphic flows). In addition, the thermal approach does not allow us to estimate the volumes of tephra produced by explosive activity;

3) Accurate processing requires filtering out data contaminated by clouds, and/or acquired with extreme viewing angles. Alternatively, the maximum daily or weekly average (considering all data) can produce appropriate but less accurate estimates.

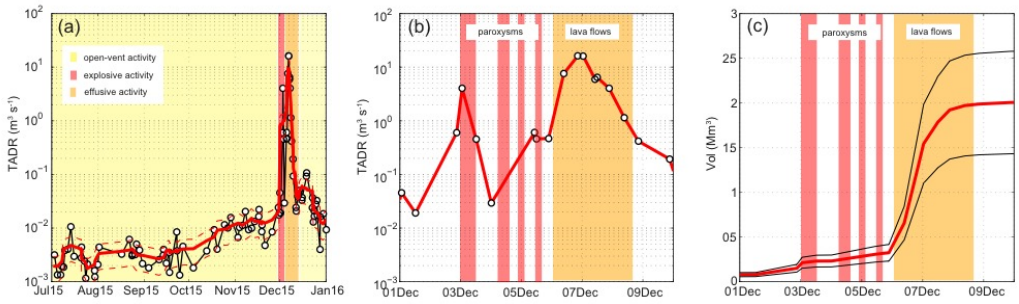

Figure 33 (a) time averaged lava discharge rate (tadr) calculated from modis-mirova thermal data using eq. 7. Note the apparent increase of tadr during october-november that precede the explosive and effusive phases (b) detail of modis-derived tadr during the four paroxysms (red field) and the effusive activity (orange field). (c) detail of modis-derived volume retrieved during the first 10 days of december 2015

The application of equation (7) to the selected MIROVA dataset allows calculating a total volume of lava equal to 2.0 ± 0.6 Mm^3 (Fig. 33). However, based on the observed activity the interpretation of the calculated volume is subdivided according the distinct phases of activity:

- *Phases 1-3* (01 July- 02 December 2015). During this phase we calculate that ~0.1 Mm^3 of magma reached the bottom of the summit craters, before being recycled back into Etna's shallow plumbing system (Tab. 1). Thus, the average TADR (0.005 m^3/s) represents the fraction of the total degassing magma flux that actually reached the surface and radiated heat into the atmosphere. However, most of the degassing magma remains some tens or hundreds of meters below the surface (or more), and therefore does not contribute to the surface thermal anomaly. It is unsurprising that, if we use a cumulative degassed SO_2 mass of 80,000 tons (Tab. 1) for this period (time-averaged SO_2 flux of ~30 kg/s), in combination with eq. 6, we obtain a much higher magma degassing volume (~7 Mm^3; magma degassing rate, ~6 m^3/s; Tab. 1). Notably, between October and November 2015, the thermal-derived magma flux reaching the surface has gradually increased likely reflecting the shallowing of the top of the magma column that preceded the onset of the paroxysmal phase (Fig. 33). The beginning of intense strombolian activity, observed on 2 December at 21:00 (UTC) was marked by a TADR equal to 0.6±0.2 m^3/s that could represent a transition between open-vent passive degassing to explosive/effusive activity.

- *Phase 4* (03 – 05 December 2015). In less than 48 hours, four consecutive paroxysms occurred at the summit craters of Etna. The plumes generated by this explosive activity often masked the thermal anomalies associated with the lava fountains and the incandescent material accumulated inside the VOR and BN craters. The thermal proxy applied during this

phase indicates a minimum volume of ~0.2 Mm^3 (Tab. 1), but this figure severely underestimates both the SO_2-based (~1.9 Mm^3) and erupted (5.1-12 Mm^3) volumes (Tab. 1);

- *Phase 5* (06 - 08 December 2015). During this phase, three small lava flows were emitted from a vent that opened at the base of the NSEC crater (Corsaro et al., 2017). The maximum TADR (16±0.6 m^3/s) was reached in the night between 6 and 7 December, when the lava flow reached a maximum extent of ~3.5 km. Based on MODIS data we estimate a total volume of ~1.7±0.6 Mm^3 which agrees well with independent field estimates (2.0 ±0.3 Mm^3; Corsaro et al., 2017).

5.5 Conclusions

We have used ground- and satellite-based information to characterize the extremely dynamic SO_2 degassing behavior associated with Etna's December 2015 paroxysmal sequence.

Our UV Camera-based SO_2 flux records taken on December 4, the first such observations during an Etna lava fountaining episode, show SO_2 emissions peaking at ~400 kg/s, and constrain the total magmatic gas output during such a paroxysm to $8 \cdot 10^8$ m^3. Based on satellite-based OMI observations, we estimate that at least 21,000 tons of SO_2 may have been injected into the atmosphere during the entire VOR paroxysmal sequence, corresponding to a total magmatic gas output of $1.4 \cdot 10^{10}$ m^3. We also infer that the degassing magma required to generate the ~21,000 tons of SO_2 is ~1.9 Mm^3, or much less than the 5.1-12 Mm^3 erupted volume. This mismatch suggest that a large fraction of magma erupted during the December 3-5 VOR paroxysms was shallow stored conduit magma, emplaced and degassed in the days (9 to 45) before the sequence onset. The paroxysmal sequence was also associated with an abrupt increase in thermal radiance, as observed by MODIS. Analysis of these data reveals a magma source of ~0.2 Mm^3, suggesting that the thermal proxy considerably underestimates the paroxysmal pyroclastic volume.

The December 3-5 VOR paroxysms were followed by an activity switch to the NSEC, fully captured by the UV camera network. Based on OMI records, the NSEC activity released at least $7.2 \cdot 10^9$ m^3 of gas, or a factor of 2 less than VOR activity. The MODIS thermal data constrain a magma IR source of 1.7 Mm^3, fitting well the lava erupted volume of ~2 Mm^3. Inverting MODIS data to lava volumes is more accurate during episodes with some effusive activity.

Table 1 – Gas and magma budget estimates for the five phases of the June-December 2015 activity phase. The cumulative SO_2 masses (column 2) are obtained by summing up the daily averaged total (TOT) SO_2 fluxes, or the SO_2 fluxes from individual crates (CC: Central Crater; NEC: North-east crater; NSEC: New South-east crater) during the specific *phase* (all obtained from the UV Camera: UV Cam). The corresponding OMI-based results are shown in the table (lines labeled "OMI"). The Cumulative SO_2 masses are used (from eq. 6) to calculate the magma degassing volumes (Mm^3) shown in column (5). The mean magma degassing rates (m^3/s; column (6)) are obtained by diving (5) by phase duration (1), converted in seconds. For the paroxysmal phases only (*phases* 4 and 5), the cumulative SO_2 masses are converted into cumulative gas masses (tons) and volumes (Mm^3) assuming the magmatic gas in the lava fountain comprises ~0.8 SO_2 mol. % (Allard et al., 2005; La Spina et al., 2015), and using the ideal gas (at T = 1100 °C and P = 0.1 MPa). The mean Time Averaged lava Discharge Rate (TADR; column (7)) is calculated averaging (for each phase) the TADR values obtained from eq. 7. The corresponding Cumulative magma volume is also shown in (column (8)). Ranges for erupted magma volumes are from the literature (Vulpiani et al., 2016; Bonaccorso and Calvari, 2017; Corsaro et al., 2017; Neri et al., 2017; Pompilio et al., 2017).

	Phase duration (days)	Cumulative SO_2 mass (tons)	Cumulative paroxysmal gas mass (tons)	Cumulative paroxysmal gas volume (m^3)	magma degassing volume (from SO_2) (Mm^3)	Mean magma degassing rate (from SO_2) (m3/s)	Mean TADR (m^3/s)	Cumulative magma volume (from TADR) (Mm^3)	Erupted magma volume (Mm^3)
Phases 1-2 (jun-nov)	100						5.00E-03	0.1	?
TOT (UV Cam)		8E+04	-	-	7.1	6.1			
CC (UV Cam)		2.3E+04	-	-	2.1	1.8			
NEC (UV Cam)		4.4E+04	-	-	1.1	1.0			
NSEC (UV Cam)		1.25E+04	-	-	3.3	2.8			
OMI		3.7E+04	-	-	3.3	2.8			
Phase 3 (1-2 dic)	2						0.22	0.04	
TOT (UV Cam)		6.70E+03	-	-	0.6	25.5			
CC (UV Cam)		6.70E+03	-	-	0.6	25.5			
NSEC (UV Cam)		0	-	-	-	-			
OMI		6.00E+02	-	-	-	-			
Phase 4 (3-5 dic)	3						1.009	0.2	5.1-12
TOT (UV Cam)		2.25E+04	2.72E+06	1.5E+10	2.0	57.3			
CC (UV Cam)		1.44E+04	1.73E+06	9.4E+09	1.3	36.6			
NSEC (UV Cam)		8.15E+03	9.81E+05	5.3E+09	0.7	20.7			
OMI		2.10E+04	2.53E+06	1.4E+10	1.9	53.3			
Phase 5 (6 dic -9dic)	4						16	1.7	~2
TOT (UV Cam)		6.45E+03	7.77E+05	4.2E+09	0.6	12.3			
CC (UV Cam)		2.98E+03	-	-	0.3	5.7			
NSEC (UV Cam)		3.47E+03	4.17E+05	2.2E+09	0.3	6.6			
OMI		1.10E+04	1.33E+06	7.2E+09	1.0	21.0			
Phase 5 (10 dic -19dic)	9						0.05	0.04	?
TOT (UV Cam)		1.03E+04	-	-	0.9	8.7			
CC (UV Cam)		4.61E+03	-	-	0.4	3.9			
NSEC (UV Cam)		5.68E+03	-	-	0.4	3.9			
OMI		5.47E+03	-	-	0.5	4.6			

Chapter 6
Results: Etna Eruption 2016

6.1 An automatic algorithm for real time processing of UV camera data: methodology and application to the 2016 Etna's activity[3]

Real-time, systematic volcanic gas measurements are key to understand and monitor volcanic activity (Oppenheimer et al., 2014; Fischer and Chiodini, 2015; Aiuppa, 2015). Active volcanoes are increasingly monitored by a variety of sophisticated volcanic gas techniques but, although the role of magmatic volatiles as main drivers of volcanic processes is now widely accepted (Wallace et al., 2015), gas monitoring still lags behind more established seismic and geodetic monitoring techniques (Saccorotti et al., 2015). This is because the low temporal resolution of gas observations has unfortunately hampered real-time analysis of fast-occurring volcanic processes, such as shallow intrusion of magma shortly prior to eruption, and/or impulsive gas ascent and release during explosive eruptions. The recent advent of UV cameras (Mori and Burton, 2006) has paved the way to volcanic SO_2 flux observations of much improved temporal and spatial resolution (see Burton et al., 2015 and McGonigle et al., 2017 for recent reviews), and is thus contributing to more effective integration between gas and geophysical datasets (e.g., Dalton et al. 2010; Holland et al., 2011; Kazahaya et al., 2011, 2016; Nadeau et al. 2011; Tamburello et al, 2012; Waite et al., 2013; Pering et al., 2015; Nadeau et al. 2015). The first examples of fully automated, permanent UV camera systems (Burton et al., 2015; Kern et al., 2015, D'Aleo et al., 2016; Delle Donne et al., 2017) are particularly promising, since they are opening the way to routine monitoring of the volcanic SO_2 flux at high-rate, and continuously (daily hours only). A current limitation of these permanent UV systems is, however, that while data acquisition is fully autonomous, data processing is still time-consuming and operator-managed, e.g., data streamed by these systems are archived and post-processed with ad-hoc codes (e.g., Tamburello et al., 2011). Use of this information for hazard assessment would require, instead, real-time processing and visualization.

The aim of this study is to present a new automatic routine for nearly real-time analysis and visualization of UV camera data. A similar processing routine is currently in use on

[3] Article to be submitted on Geoscience

Stromboli (http://147.163.124.220/uv1_page.php; Delle Donne et al., 2017), but its operational principles have not been discussed in detail, to date. To test performance of this automatic processing algorithm, we report on automatically processed data streamed by a permanent UV camera deployed on Mount Etna (Montagnola Site, Fig. 1). Etna is one of the volcanoes worldwide with the longest and most continuous SO_2 flux record. Etna's volatile output is mainly sourced persistent passive SO_2 plume emissions via the five main summit craters (Voragine, VOR; Bocca Nuova, BN; North East Crater, NEC and South east Crater SEC, New south east Crater NSEC). Additional emissions, which are sometimes very vigorous, do temporary take place during eruptions (Caltabiano et al., 2004). SO_2 flux measurements have become fundamental to volcano monitoring on Etna since the 1970's using the COSPEC (Moffat and Millan, 1971; Stoiber et al, 1983; Caltabiano et al., 1994; Bruno et al., 1999) and, more recently, a network of Differential Optical absorption spectrometers (FLAME; (Burton et al. 2004). In recent years, the advent of the UV cameras has allowed the first high-rate, high spatial resolution measurements of the volcanic SO_2 flux (Tamburello et al., 2013; Pering et al., 2014a, b; D'Aleo et al., 2016; Wilkes et al., 2017). No automatically calculated SO_2 flux has ever been reported, to date.

To demonstrate the utility of automatic data processing in volcano monitoring, we apply our processing routine to retrieval of UV camera results obtained in 2016. The 2016 volcano's degassing behavior is characterized by combining SO_2 flux data with thermal, acoustic, and seismic observations. We use satellite-based thermal data obtained from the MIROVA system (Coppola et al., 2016) that uses MODIS radiance data, and ground-based thermal data streamed by the INGV-OE monitoring EMOT IR camera, located at the same Montagnola site (Andò and Pecora, 2006).

SO_2 fluxes are also compared with seismic RMS amplitude and infrasonic activity results, which are traditionally used to constrain volcanic activity state and evolution (Alparone et al., 2003; Vergnoille and Ripepe, 2008; Marchetti et al., 2009; Patanè et al., 2013; Bonaccorso et al., 2013, 2014, 2017; Spampinato et al., 2015; Gambino et al., 2016).

All these independent data-sets show coherent temporal variations that validate the use of UV cameras approach for detecting subtle changes in volcanic and degassing activity. Overall, our results demonstrate UV cameras as low-cost valuable tools for remote monitoring of gas emissions at open-vent volcanoes.

6. 2. Instruments

6.2.1 UV camera system

The UV camera system has been installed at Montagnola site (UV3), and is designed to send real-time SO_2 flux results to INGV-Osservatorio Etneo (in Catania) using a WiFi radio. The objective is to capture gas emissions associated with diverse volcanic processes and dynamics, including quiescent (passive) degassing, explosive eruptions (strombolian activity/lava fountaining) and effusive eruptions. The Montagnola is located at a distance of ~3 km from the active vents and grants perfect views of the southern sector of the summit crater area (Fig. 1). Our additional goal is to resolve gas contributions from the southern-eastern (SEC and NSEC) and central (VOR and BN) craters.

6.2.2 Seismic, thermal and infrasonic data

Our SO_2 flux results are compared with seismic and infrasonic data captured by ETN station, located at Lapide Malerba, at 5 km from the summit area . ETN is equipped with a broad-band seismometer (Guralp CMG-40T, 800 V/m/s with an Eigen period of 30 s) and a five-elements short-aperture infrasonic array equipped with infrasonic sensors (iTem-prs 0100) with sensitivity of 25 mV/Pa, a noise level of 0.01 Pa, and a flat frequency response of 0.01-100 Hz.

In view of the suggested link between SO_2 flux and volcanic tremor at Mt. Etna (Malinconico, 1979; Leonardi et al, 1999; Tamburello et al., 2013; Zuccarello et al., 2013), we calculate volcanic tremor amplitude from raw traces recorded at ETN station, by averaging within a 1-minute length window the maximum RMS amplitude taken within 1 second window.

Infrasonic activity at Mt. Etna, thought to be related to gas dynamics in the shallowest portion of the conduit, is a powerful tool to detect coherent infrasonic signals of volcanic origin (Ulivieri *et al., 2009;)*

These events, automatically detected using the semblance method (Ripepe et al, 2007), are used to capture in real-time source and intensity of explosive activity, and thus issue alert warnings (Ulivieri et al., 2009). Transition from strombolian to lava-fountaining Mt Etna has already proven to be efficiently tracked using infrasound.

Thermal remote sensing offers a great opportunity to follow volcanic unrest from ground and space and to characterize volcanic activity in near-real time. We here use data from the MIROVA system (Coppola et al., 2015) and thermal cameras (Andò and Pecora, 2006) to

constrain onset, duration and intensity through time of eruptive events occurring during the investigated period.

6.3. Application of the automatic real time algorithm: the Etna 2016 case

In view of its recurrent activity and robust past SO_2 flux record, Mt. Etna is an ideal test site for validating our automatic processing method. We report below on the data automatically acquired and processed during 2016, a period characterized by substantial temporal changes in activity styles that included a lava fountain paroxysmal sequence (May), strombolian activity (August) and persistent passive degassing. Our aim is to test if the different degassing dynamics related to such diverse activity styles can be distinguished and characterized in automatic (and nearly real-time) by our UV3 permanent SO_2 camera system.

6.3.1 Etna's volcanic activity in 2016, SO_2 flux records, and comparison with seismic, acoustic and thermal datasets.

The significant variability in volcanic activity style and vigor in 2016 is well reflected by the dynamic SO_2 flux behavior (Fig. 34), as outputted by our automatic processing algorithm. As illustrated in Figure 34, our 2016 temporal record shows daily averaged SO_2 fluxes ranging between a few hundreds to ~6,000 tons per day (t/d). The associated standard deviations of daily fluctuations that concur in the computation of daily average range from 100 to 4000 t/d. To assist interpretation of SO_2 flux variations, we also report time-series in physical parameters including seismic tremor, thermal radiance and infrasonic activity (Fig. 34). Tremor amplitude (Fig. 34b) is shown as RMS amplitude integrated over a one minute of seismic record along the vertical component (ETN site). Thermal activity is expressed in terms of Volcanic Radiative Power (Coppola et al., 2013), while infrasonic activity is presented in the form of daily number of volcanic events detected by the ETN infrasonic array.

We distinguish below three main phases of activity, which SO_2 flux and geophysical results are discussed separately and in chronological order: 1) a pre-2016 paroxysmal phase, in which the volcano was initially quiet (only quiescently degassing) after the major paroxysmal phase occurred in December 2015. Starting from March, volcanic activity gradually resumed; 2) a paroxysmal phase, characterized by lava flows and three lava fountaining episodes, occurred in a brief time lapse between 18 and 25 May; 3) a post

paroxysmal phase, that includes a period of reduced activity in the two months after the May paroxysms, followed by a gradual (re)intensification of volcanic activity culminating in a mild strombolian activity phase at central craters in August-September. This summer 2016 strombolian phase was followed by a general subsidence of the central crater's floor and by reduced activity until the end of the year.

These phases are described in more in detail in the following paragraphs.

6.3.1.1 The pre-paroxysmal phase

Until end of March, volcanic activity was characterized by sporadic ash emissions from NSEC and from NEC. The SO_2 daily averaged fluxes fluctuated at around ~2000 tons/day, seismic tremor was stable at around average levels for Etna, and thermal and infrasonic activity occurred at reduced levels.

During April to May 18th, 2016 volcanic activity gradually resumed and intensified, with frequent ash venting and occasional strombolian activity at NEC and NSEC craters (INGV-OE monitoring reports, 2016). SO_2 emissions reached daily averaged fluxes of ~4000 t/d, infrasonic activity intensified in terms of number and amplitude of detections, and seismic RMS amplitude fluctuated within a subtle increasing trend. No significant thermal anomaly was observed (Fig. 34).

6.3.1.2 The paroxysmal phase

Escalating volcanic activity culminated on May 18th at 10:57GMT with a short-lived lava fountaining episode from the central craters (VOR crater). This event marked the beginning of a paroxysmal sequence that lasted until May 25th, and was characterized by the occurrence of three additional lava fountaining episodes at VOR, accompanied by lava effusion from both BN and NEC. Onset of the paroxysmal sequence was fully captured by our UV camera system, with SO_2 daily averaged fluxes peaking at 6000 tons/day (Fig. 34). All monitored parameters showed coherent increases during this volcanic unrest. High intensity thermal anomalies (of the order of 10^9 MW) were consistently recorded by the MIROVA system during the paroxysmal sequence, and the consequent emplacement of lava flows (Fig. 34). Seismic tremor and infrasound consistently showed high levels of activity.

6.3.1.3 The post-paroxysmal phase

From May 25th until the end of June, volcanic activity paused, while SO_2 fluxes and geophysical parameters (seismic, infrasound, thermal) gradually decreased down to low levels (Fig 34). Field observations (INGV-OE monitoring reports, 2016) indicate that only weak gas/steam emissions at the summit craters were observed, with no explosive and/or

effusive activity. From the end of June, however, enhanced gas emissions from BN, VOR and NEC were increasingly reported (INGV-OE monitoring reports, 2016), accompanied by extensive fracturing of the summit crater area. Consistently with this general reactivation of the volcano, SO_2 fluxes increased again, from ~ 900 to ~2300 tons/day (on a daily average) (Fig. 34). Thermal activity, as detected by MIROVA, coherently increased from 1.3 to 4.5 MW on a daily basis, and a notable increase was also observed on averaged RMS seismic amplitude (Fig. 34). Following a relative minimum in gas, thermal and seismic activity in mid-July, volcanic activity intensified again in August, when intense strombolian explosions started at both BN and VOR. Such an increase was clearly captured by seismic RMS amplitude, infrasound, and thermal signals, with SO_2 fluxes attesting at a high levels of >2000 tons/day. Strombolian activity continued until the end of August, accompanied by intense degassing. Since October, a general subsidence was observed in the Central Craters' inner floor, which had previously been filled by lavas and pyroclastic materials erupted in the 2015-2016 paroxysmal sequences. This inner crater subsidence and collapse was nicely paralleled by SO_2 fluxes declining down to low values (~ 650 tons/day on average). RMS seismic amplitude and thermal radiance decreased as well.

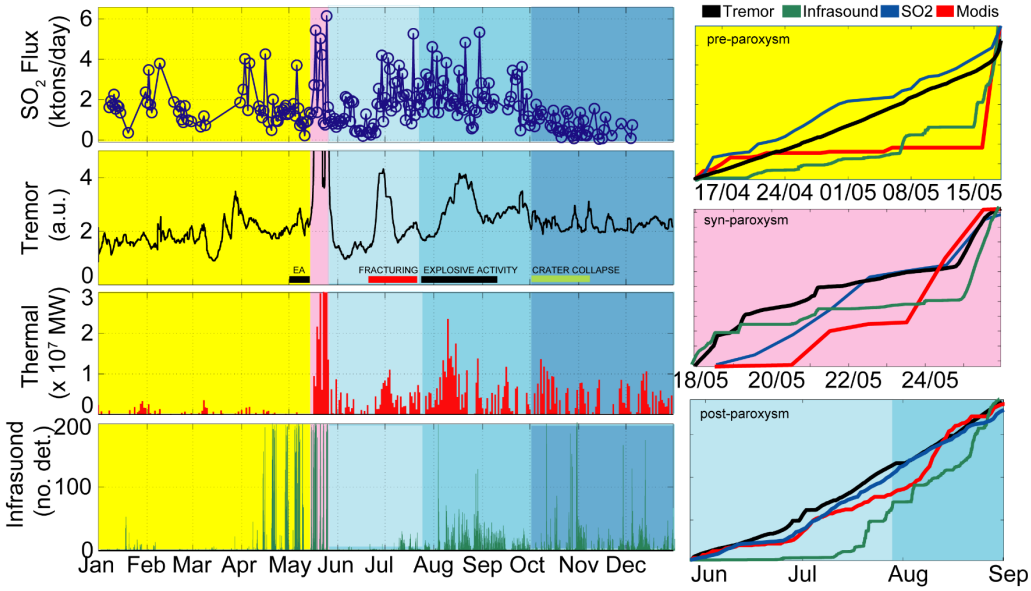

Figure 34 daily averaged so₂ fluxes (a) are compared with independent geophysical data, including seismic tremor amplitude (b), thermal radiance from mirova (c), and infrasonic daily number of detections (d). Three volcanic phases are distinguished by different colors: yellow, pre-paroxysmal phase; pink: paroxysmal phase; blue: post-paroxysmal phase. Different blue color tones identify different activity levels during the post-paroxysmal phase: light blue, post-paroxysm reduced activity; medium blue: strombolian activity; dark blue: reduced activity associated with collapse of the inner central crater's floor.

6.3.2 SO_2 release during the paroxysmal phase

Our SO_2 fluxes observations taken during the May 2016 paroxysmal phase are detailed (along with seismic data) in Figure 35. This paroxysmal sequence lasted seven days, from 18th to 25th May 2016, and included four intense lava fountain episodes alternating with repose periods (Fig. 35). Three of these lava fountaining events are clearly marked by short-lived peaks in seismic tremor amplitude on May 18th, 19th, and 21st (Fig. 35), while episode 4 that closes the paroxysmal sequence (May 25th) is associated with a wider, longer-lived phase of seismic amplitude increase. This alternation of explosive episodes and repose periods in well reflected in the degassing record, showing peaks in daily averaged SO_2 flux in on three (May 18th, 21st, and 25th) out of four days of paroxysmal activity. It is interesting to note that only in one measurement day (May 18th) the peak daily SO_2 flux was caused by the camera recording the paroxysmal episode itself (see below). On the 21st and 25th, the paroxysms occurred outside the camera's recording time interval, and the elevated daily fluxes thus correspond to heightened passive degassing and/or milder (strombolian) explosive activity prior/after them.

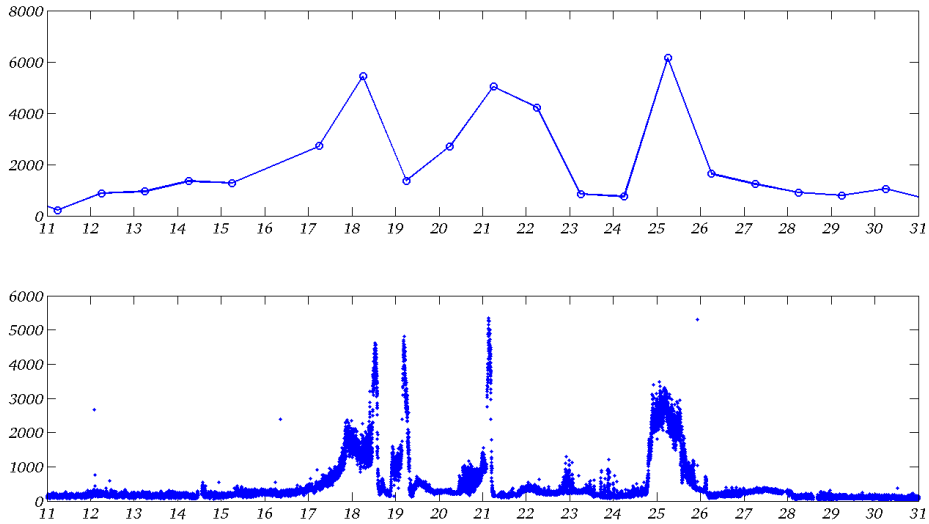

Figure 35 daily averaged so2 fluxes recorded during paroxysmal phase show good agreement with seismic tremor amplitude, with relative maxima well fitting high tremor phase of paroxysmal sequence.

The May 18th lava fountaining event, instead, which occurred in the morning, was entirely captured by the SO_2 camera (Fig. 36), allowing us to explore the "fast" degassing dynamics associated with such kind of explosive event. Lava fountains are of special concern on Etna since the volcanic ash they inject into the atmosphere is a recurrent threat for aviation and population living in the surroundings (Scollo et al., 2012). These events unfortunately, while very well monitored and understood (Harris and Neri, 2002; Alparone et al., 2003; Dubosclard et al., 2004; Andronico and Corsaro, 2011; Calvari et al., 2011; Patanè et al.,

2013; Bonaccorso et al., 2013, 2014, 2017; Spampinato et al., 2015; Gambino et al., 2016), are poorly characterized in terms of their associated gas emission rates and volumes.

Our May 2016 example is, therefore, one of the first sin-explosive gas records on the volcano (D'Aleo et al.., 2017). Onset of the lava fountain at ~ 11 GMT, as constrained by co-acquired records of the INGV-OE thermal camera (Fig. 36), was clearly detected as a visible SO_2 flux increase up to >10,000 tons/d, relative to a pre-eruptive level of ~5000 t/d. In the following hour, while activity escalated to peak at ~ 11.30 – 12.00 GMT (see thermal records), a fluctuating and irregular SO_2 flux trend was registered (Fig. 36). Co-acquired thermal and visual images (see panels in Figure 36), clearly indicate that negative peaks in the SO_2 flux time-series were systematically associated to the presence of ash.

The presence of ash within the plume severely impacts SO_2 detection via UV cameras (e.g., Tamburello et al., 2012), particularly in near-vent measurements where plumes can be very ash-rich and thus optically opaque. Thermal and visual observations show that ash caused high-frequency fluctuations (short-lived negative peaks) in the SO_2 flux record particularly during the paroxysm climax (~ 11.30 – 12.00 GMT), but also prior to the lava fountain onset, e.g., after 09.00 GMT when the webcam captured the first ash injections with no thermal anomaly yet detected (Fig. 36). The thermal signal time-series point to a lava fountaining termination at ~14 GMT, consistent with a gradual SO_2 flux decline since 14.30 GMT.

Our SO_2 fluxes time-series can be used to estimate the cumulative SO_2 mass released by the lava-fountain, by integrating the signal over the eruption duration. Using an average flux of 7000 tons/day and fountain duration of ~3.5h, we obtain a total SO_2 mass released in the event of ~1000 tons. We caution our inferred mass in a minimum estimate, in view of presence of volcanic ash that severely depresses the measured SO_2 signal during the eruption climax phase.

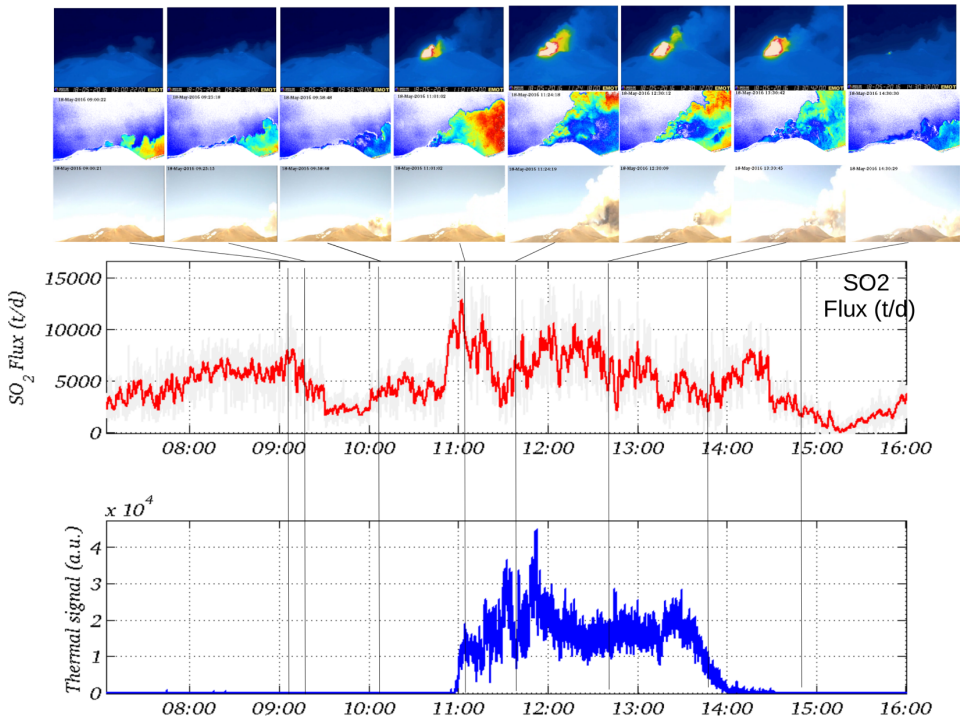

Figure 36 SO_2 camera record of the lava fountaining event of may 18th. The gas record is compared with the thermal signal recorded by the co-located ingv-oe infrared camera. The upper panels show thermal, uv and visula images of the summit area in specific time intervals

6.4. Discussion.

6.4.1 Advantages in automatic processing of UV camera data

Volcanic SO_2 emissions are extensively monitored worldwide using instrumental networks of scanning ultraviolet spectrometers using the Differential Optical Adsorption Spectroscopy (DOAS) technique (e.g., Galle et al., 2003). The advantage of this method is that both acquisition and processing are relatively easy to automate (e.g., Galle et al., 2010), yielding exceptionally continuous records of volcanic SO_2 fluxes at relatively high temporal resolution (tens of minutes; e.g., Christopher et al., 2010; Mori et al., 2013; Hidalgo et al., 2015). Biases in the technique include, however, a poor spatial resolution (making impossible to distinguish contemporaneous degassing from different vents), temporal resolution inadequate to resolve individual explosive events, and errors related to poor knowledge of plume speed (McGonigle, 2005). These limits can be overcome using UV cameras, which have comparatively much higher spatial and temporal resolution and offer the opportunity to measure gas velocities directly from image sequences (Burton et al., 2015; McGonigle et al., 2017). For example, Delle Donne et al., (2017) have demonstrated the ability of UV cameras to capture a precursory phase of heightened SO_2 flux in the weeks prior to the 2014 effusive eruption in Stromboli. Since these high SO_2 emissions were largely determined by high gas exit velocities related to escalating explosive activity, UV cameras were a most ideal technique for their detection.

Automation of UV camera acquisition and processing routines is required to fully exploiting the volcano monitoring potentials of UV cameras. Changes in volcanic activity state do often occur at such very short timescales (hours) to mandatory require real-time data analysis and visualization. Unfortunately however, all published UV camera datasets are, at least to the best of our knowledge, based on post-processing of archived UV camera data.

One of the main objectives of the present work is to report on operational principles and performances of a newly developed automatic algorithm that allows real-time processing and visualization of UV camera-based SO_2 flux results. This automatic algorithm has been used to real-time process camera data obtained on Mt. Etna in 2016, yielding the SO_2 flux time-series shown in Figure 34a. The validity of the automatically processed SO_2 fluxes is here tested by comparison with SO_2 fluxes manually obtained using the Vulcamera software (Tamburello et al., 2013) (Fig. 37). This comparison demonstrates suitable enough average errors (~50 %), and a good correlation (Fig. 37). The correlation coefficient (R^2) between manual and automatic measurements is ~0.75, with a best-fit regression line showing a ~1 proportionality factor. Overall, this comparison validates the use of the automatic SO_2 flux determination procedure, paving the way to its full exploitation in real-time volcano monitoring, as already started on Stromboli (http://147.163.124.220/uv1_page.php; Delle Donne et al., 2017).

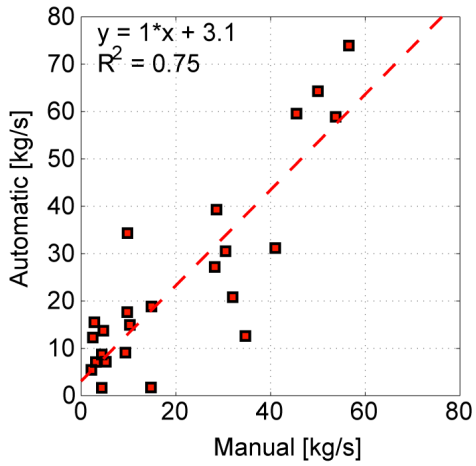

Figure 37 comparison between daily averaged so_2 fluxes calculated by a manual operator (using vulcamera software, tamburello et al, 2013) and those obtained by the automatic algorithm. The correlation coefficient between the two datasets is good (0.75), with a 1:1 proportionality ratio. This correlation validates the automatic algorithm as an alternative, reliable method for so_2 flux calculation.

6.4.2 Insight into degassing mechanisms

Our UV camera-based dataset can be used to gain novel insights into the relationship between rates of SO_2 release from Etna's magma and eruptive styles. These latter have quite diverse in 2016, ranging from short-lived, intense lava fountaining in May to more long-lasting, milder strombolian activity in August.

Combining SO_2 flux and thermal datasets is, at least in principle, a very effective way to investigate and characterize degassing dynamics associated with various eruption types, because these methods provide complementary information on, respectively, gas and magma feeding rate into the shallow volcano plumbing system. We therefore compare, in Figures 34d-f, the cumulative SO_2 fluxes and thermal flux (from MIROVA) trends, in the attempt to characterize gas and magma ascent dynamics prior, during and after the May paroxysmal phase and the August Strombolian sequence.

Our SO_2 flux time-series implies distinct degassing behaviors for the periods prior, during, and after the May 2016 explosive sequence (Fig. 34). In April-early May 2016, before the eruption onset, the SO_2 flux ranged between 300±100 t/d and 1000±350 t/d. The SO_2 flux then increased during the May 2016 eruption, reaching peak values of 6000±2000 t/d (on 25 May) during the lava fountaining sequence, during which the thermal VRP was also particularly elevated. After a general activity drop from the end of May until the end of June, that was consistently observed in the thermal VRP and SO_2 record, volcanic activity slowly resumed in early July with intense degassing from NEC, VOR, and NSEC craters (INGV-OE monitoring report, 2016) which lasted for few weeks. This enhanced degassing was well marked by increasing SO_2 flux and VRP (Fig. 34). Coherent, more pronounced increases in both SO_2 flux and VRP were also observed during the BN-VOR August, Strombolian sequence.

It is worth to note that the cumulative SO_2 flux and thermal flux trends were remarkably different before the May and August events (Fig. 34d and 34f). No precursor SO_2 flux variation was observed in the May case, with an emission jump observed only at onset of the paroxysmal sequence. In contrast, the cumulative SO_2 flux showed a clear inflection point one month before the August strombolian sequence, with the slope of the cumulative curve (a proxy for average flux) increasing from 800 to 2000 t/d. The cumulative thermal trend showed same dynamics: no significant increase before the May paroxysm(s), and a slight but detectable increase one month before the August strombolian activity phase (Fig. 34).

We argue these different gas/thermal dynamics are related to different rates of magma ascent prior to either a lava fountaining or a strombolian episode. Decompression during magma ascent causes volatiles to exsolve into bubbles, which ability to separate from melt mostly depend on melt viscosity and rates of magma ascent (e.g. Gonnermann & Manga, 2012). In basaltic magmas, when magma ascent is fast, melt and exsolved gas remain coupled allowing for rapid acceleration and hydrodynamic fragmentation in lava-

fountaining eruptions (Parfitt, 2004). In such conditions of fast magma ascent, capturing a precursory gas increase prior to a lava fountain becomes challenging, if not over timescales of hours/minutes. In contrast, at slower magma ascent, gas can more effectively separate from melt within the conduit, potentially leading to enhanced gas emissions prior to magma reaching the surface to erupt. This gas-malt separation can be causing out SO_2 flux increase long prior onset of strombolian explosions in August 2016 (Fig. 34).

If the above interpretation is correct, then it should be expected that the melt/gas mass ratio characterizing paroxysmal (lava fountaining) sequences is closer to original magmatic proportions than during strombolian activity (when gas and magma have extensively been separated one each other). To estimate the melt/gas mass ratio during the two unrests (May and August, 2016), we initially convert the VRP thermal signal into a mass eruption rate, using a radiance/mass conversion factor as given by Coppola et al. (2013, 2016). From this, we estimate a total erupted (lava) mass for the May 18-25 paroxysmal sequence of 1-2 Mm^3, corresponding to an average mass output rate of 1.5-3 m^3/s. Using same methodology, we consistently obtain a much lower mass output rate (of 0.02 – 0.04 m^3/s) and total mass (0.6 – 1.2 Mm^3) for the milder strombolian phase in August. Interestingly, while thus the strombolian and paroxysmal episodes are characterized by mass output rates differing by ~2 orders of magnitude, no similar discrepancy is observed in the SO_2 flux record (average values are 2000 and 3000 t/d for the strombolian and paroxysmal phases, respectively).

For a basaltic magma with a 2950 kgm^{-3}density, and having SO_2 contents in groundmass and melt inclusions of respectively 0.04 wt. % and 0.25 wt. % (e.g. Metrich et al., 2004), the average SO_2 fluxes of 2000 and 3000 t/d covert (using equation in Allard, 1997) into magma input rates of ~2m^3/s and ~3 m^3/s for the strombolian and the paroxysmal phases, respectively. Thus, a large mismatch between SO_2-based input rates (~2m^3/s) and thermal-based output rates (0.02-0.04 m^3/s) is obtained for the strombolian phase. This huge difference between input and output suggests that most degassed magma is finally not erupted, but recycled back within the conduit (Allard, 1997). In contrast, magma input and output rates both converge at ~3 m^3/s during the May paroxysmal phase, in total agreement with a mechanism of fast magma ascent that prevent gas to escape from magma as it is rapidly decompressed within the conduit.

The balance between magma input rate and discharged lava throughout year 2016 is illustrated in figure 38, suggesting magma recycling is the dominant mechanism in Etna's magma dynamic (Allard, 1997). Only during paroxysmal phases, output rate may balance out the input rate. Finally, we note that the output/input ratio reached a minimum in April-

early May, prior to onset of paroxysmal phase. This minimum is suggestive of a slight enhanced in degassing (relative to thermal output) starting circa one month before onset of the first lava fountaining event. Such enhanced degassing cannot be detected if one considers the SO_2 flux record alone. The ratio between gas and thermal output may thus reveal as a powerful toll to detected and amplify even subtle changes in magma dynamics in the upper conduit.

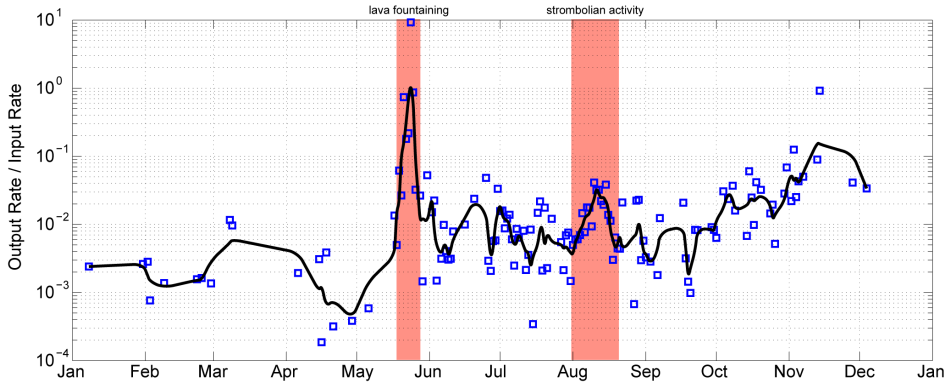

Figure 38 ratio between magma output rate estimated from thermal radiance and magma input rate estimated from so2 fluxes, during and after paroxysmal activity. This ratio oscillates around an average value of $2x10^{-3}$ before paroxysm while shows average grater value after paroxysm indicating a higher thermal signal persisting after paroxysmal phase and not followed by enhanced gas flux. Ratio show a minimum (excess degassing) ~one month before the paroxysmal onset of activity.

6.4.3 Comparison between different paroxysmal sequences

It is well established that SO_2 fluxes are directly linked to the rate of magma ascent and degassing (e.g., Allard, 1997). Thus, temporal variations in SO_2 flux do reflect changes in magma feeding to a volcano's shallow plumbing system, and as such may help tracking transition in activity style, from quiet passive degassing to paroxysmal explosions (Oppenheimer et al., 2011). On Etna, we now have 3 years of UV camera observations available (D'Aleo et al., 2016, 2017, this study), during which transition from quiescence to eruption has frequently been observed. We thus examine our dataset in the attempt to tentatively identify any possible systematic SO_2 flux threshold/trend that corresponds to such activity switch. At this aim, we compare in Figure 39 the cumulative SO_2 flux trends (time-normalized) for three different periods encompassing three lava-fountaining episodes, occurred in August 2014, December 2015 and May 2016, respectively.

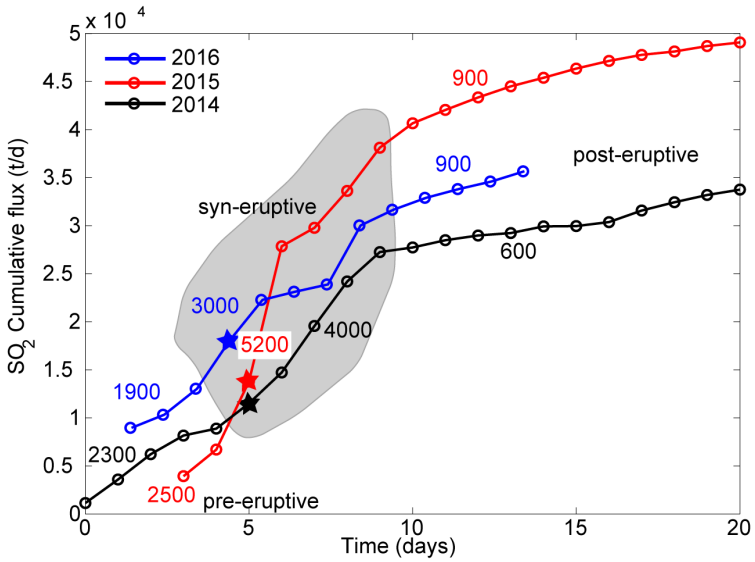

Figure 39 comparison between cumulative so_2 flux trends associated with three lava fountaining paroxysmal sequences occurred at etna's nsec (black line) in august 2014, and at vor in december 2015 and may 2016 (red line and blue line). Stars indicate onsets of the paroxysmal sequence. Pre-eruptive, syn-eruptive and post-eruptive phases show similar so_2 fluxes for all these three events. In each of three events, pre-eruptive fluxes range between 1900 and 2500 t/d, syn-eruptive fluxes are the highest (3000-5200 t/d), while post-eruptive fluxes are systematically the lowest (< 900 t/d)

For each of three events, we calculate the averaged SO_2 fluxes (corresponding to the slopes of the cumulative curve) in the periods before, during, and after the lava fountain, and we find significant similarities between the three events. In each of the 2014-2016 events, the pre-paroxysm fluxes fall in a relatively narrow range, between 1900 and 2500 t/d. The sin-eruptive (during the paroxysmal sequence) fluxes are typically higher, and span between 3000 and 5200 t/d (Fig. 39), and are the highest during the December 2015 paroxysmal sequence that is consistently the most energetic paroxysmal sequence in the past few years (Pompilio et al. (2017). Finally, each of the three post-paroxysmal phases is characterized by reduced SO_2 emissions, with fluxes ranging between 600 and 900 t/d, and implies reduced magma supply and degassing of a volatile depleted (residual?) magma after each eruptive episode.

Our preliminary results are suggestive of the existence of a systematic pattern in SO_2 emissions that, if confirmed, would imply a recurrent degassing process/mechanism prior, during and after the Etna's paroxysmal explosions. Clearly, additional data are required to corroborate this initial hypothesis.

6.5 Conclusion

SO_2 imaging at Mt Etna during the year of 2016 revealed different styles of gas emissions, reflecting changes in volcanic activity, from quietly passive degassing to effusive eruptions and lava fountaining and intense strombolian activity.

We designed a novel methodology to automatically calculate SO_2 fluxes which is based on a computer-based detection of image quality, and on a calculation of plume speed using computer vision libraries. This allows us to have a real time information on volcano degassing dynamics at a high spatial and temporal resolution making a further step ahead in volcano monitoring of gas emission.

We have validated the methodology through manual processing of the dataset and through integration of other geophysical information. This allowed also to us to speculate on different degassing regimes that occurred at Mt. Etna during 2016.

Continuous automatic record of UV images allowed us also to entirely capture a lava fountaining episode from Voragine crater. This is to best of our knowledge, the first SO_2 camera record at high spatial and temporal resolution of an active fountaining of Voragine craters, which allow us to characterize an high level of degassing of 5-6000 tons/day prior the onset of the eruption, and a further increase during the event up to 15000 tons/day. We also show how that ash presence within the plume partially prevents the gas detection via differential absorption leading to underestimate of the total gas mass erupted.

We show that SO_2 precursory signal associated with enhanced activity is not always present and is somehow dependent on how fast magma rises within the conduit. Using thermal radiance detected by MIROVA, we estimate mass flux and we compared with gas flux. This allows us to evaluate whether gas is decoupled from erupting lava. Data suggest that lava emitted during paroxysmal phase is in equilibrium with total released gas, while during strombolian phase lava and gas are not coupled, suggesting a mechanism of magma recycling within the conduit.

In this work we also compared SO_2 flux time series associated with three paroxysmal events occurred in 2014, 2015 and 2016, highlighting strong similarities among each other in the SO_2 flux intensities measured prior, during and after paroxysmal phase. In particular, pre-eruptive fluxes show all consistent values of ~2000 t/d that are very close to value measured during strombolian phase occurred in August 2016. Eruptive phase shows highest fluxes from 3000 t/d up to 5200 t/d on a daily average, while post-eruptive phases show lowest value that are close to the average SO_2 fluxes measured at Mt. Etna. This evidence may have implications in identifying the thresholds in gas emission that could help discriminate various regimes of volcanic activity from a gas point of view.

Chapter 7
Results: UV camera in support to Lidar

The UV Camera sign a step forward in volcano monitoring thanks also to the possibility to measure with high precision the gas velocity in the volcanic plume from the UV images. Taking advantage on this UV camera is often use in combination with other instrument, Multigas, in order to retrieve the gas flux from the measured gas ratio of the other gases with SO_2, and in this case Lidar, in order to know the gas velocity to calculate the CO_2 flux. Here we show the first simultaneous Dial Lidar and UV camera measurement performed on Etna volcano that linked the innovation of the two instrument and that fill the gap of each other's.

7.1 Volcanic Plume CO_2 Flux Measurements at Mount Etna by Mobile Differential Absorption Lidar[4]

In the last two decades, there have been major advances in the instrumental monitoring of volcanic gas plume composition and fluxes (Oppenheimer et al, 2014). These have included the first instrumental networks of scanning Differential Optical Absorption Spectrometers (DOAS) for volcanic SO_2 flux monitoring, the implementation of satellite-based volcanic gas observations, and the advent of sensor units for in situ gas monitoring (Oppenheimer et al, 2014; Saccarotti el al., 2014). Owing to this technical progress, volcanic gas plume composition and fluxes have increasingly been used to extract information on degassing mechanisms/processes (Edmond et al., 2008), and to derive constraints on shallow volcano plumbing systems (Allard et al., 1994). However, work still needs to be done to increase the number of volcanic gas species that can be detected in plumes, which remain few if compared to the countless number of chemicals quantified from fumarole direct sampling (Oppenheimer et al, 2014.)

Studying volcanic gas plumes has additionally contributed to monitoring, and eventually allowed the prediction of volcano behaviour (Saccarotti et al., 2014). In particular, it has been shown that, at open-vent persistently degassing volcanoes, volcanic eruptions are often preceded by anomalous increases of the volcanic CO_2 flux (Aiuppa et al., 2010). These initial

[4] Article published on Geosciences 2017, vol. 7 (1) , 9 doi:10.3390/geosciences7010009

observations have motivated attempts to systematically monitor the volcanic CO_2 flux, and to identify novel measurement strategies (Burton et al., 2013). Until recently, however, attempts to remotely sense the volcanic CO_2 flux from distal locations have been limited in number (Aiuppa et al., 2015, Queiber et al., 2016), while the majority of the observations have involved in situ measurements in the proximity of hazardous active volcanic vents (Aiuppa et al., 2015). On Mt. Etna, for example, one of the largest volcanic CO_2 point sources on Earth (Allard et al., 1991), the volcanic CO_2 flux has systematically been measured since the mid-2000s by combining in situ measurement of the volcanic CO_2/SO_2 ratio (with portable or permanent Multi-Component Gas Analyzer Systems, Multi-GAS; (Aiuppa et al., 2006; Pering et al., 2014)) with remotely sensed SO_2 fluxes (La Spina et al., 2010; Allard el al.,2006). No successful report exists, at least to the best of our knowledge, of spectroscopy-based detection of Etna's volcanic CO_2 flux from a remote (distal) location.

Within the context of the ERC (European Research Council) starting the grant project BRIDGE (BRIDging the gap between Gas Emissions and geophysical observations at active volcanoes), we designed a new DIAL (Differential Absorption Lidar) (Fiorani et al., 2010), with the specific objective to remotely sense the volcanic CO_2 flux. Lidars have only recently been introduced in volcanic gas studies. A CO_2 laser–based lidar was used at Mt. Etna in 2008 (Fiorani et al., 2009) and at Stromboli Volcano in 2009 (Fiorani et al., 2011) to measure the volcanic plume water vapour flux. More recently, lidars were first been used to target volcanic CO_2 (Aiuppa et al., 2015; Queiber et al., 2016; Fiorani et al., 2015; Aiuppa et al.,2017. Our lidar BILLI (BrIdge voLcanic LIdar) (Fiorani et al., 2015), for example, has recently been used to successfully retrieve three-dimensional tomographies of volcanic CO_2 in the plumes of Pozzuoli, Solfatara in 2014 (Aiuppa et al., 2015) and Stromboli volcano in 2015 (Fiorani et al., 2016; Aiuppa et al., 2017). As such, although gas-sensing lidars remain far less exploited in volcanology than those targeting volcanic ash/particles (Scollo el al., 2012; Wang et al., 2008), this novel application field may expand rapidly in the near future.

Here, we report on the first successful use of BILLI at Mt. Etna. We show that, in our July–August 2016 Etna experiment, the lidar successfully resolved a volcanic CO_2 signal of a few tens of ppm (in excess to the background air) from more than 4 km of distance, and with good spatial (5 m) and temporal (10 s) resolution. These results are used to derive the first "remote" assessment of Etna's volcanic CO_2 flux. Our observations open new perspectives for routine volcanic CO_2 flux monitoring via lidars.

7.2 Materials and Methods

7.2.1. Field Set-Up on Mt. Etna

Observations on Mt. Etna were conducted from 28 July to 1 August 2016, including an initial phase of instrumental setup (28–29 July). Successful CO_2 flux detections were obtained on 31 July, when optimal viewing conditions persisted over the day. The DIAL was mounted in a trailer loaded on a truck, parked at the INGV (Istituto Nazionale di Geofisica e Vulcanologia) observatory "Pizzi Deneri" (Figure 40). The observatory is located at 2823 m a.s.l., northeast of the summit crater of Mt. Etna (3329 m a.s.l.), and at about 3 km from the main degassing vents (Figure 40).

The lidar was used to scan the volcanic plume vertically, keeping a constant azimuth angle (230°) and varying the elevation angle from 7° to 14° (Figure 40). A full 7° to 14° vertical scan was completed in ~15 min, and one atmospheric profile every 10 s was recorded throughout. With this instrumental set-up, the volcanic gas plume of the Etna's northeast crater was investigated (Figure 40), plumes from other craters being either too dilute (southeast crater) or only partially visible (central craters).

At our measurement conditions, two rock surfaces, corresponding to the eastern, outer flanks of the central crater, were intercepted by the laser beam at distances of 1.6 and 2.1 km, and at elevation angles from 7° to 9°. These rock surfaces retro-reflected the laser beam, yielding strong return signals (see below, Figure 41). The volcanic plume, e.g., high in-plume excess CO_2 concentrations, was detected in between the two above rock surfaces, and in the 2.2–4.2 km distance range.

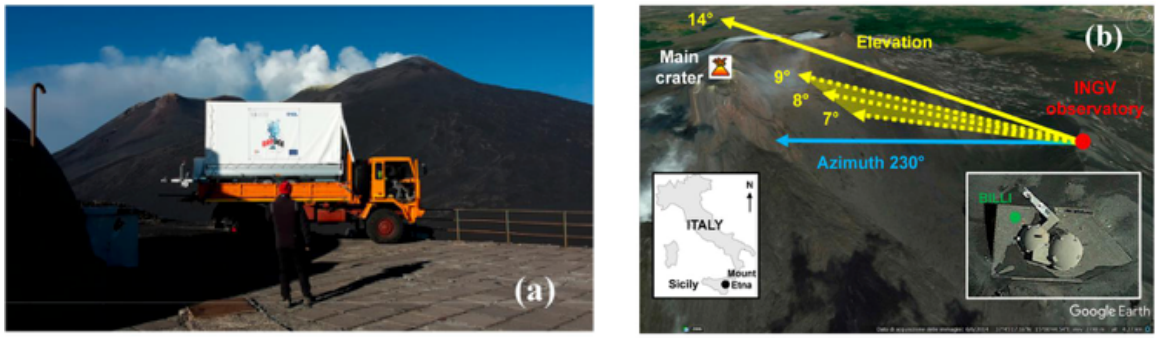

Figure 40 (a) the billi dial (bridge volcanic lidar, differential absorption lidar) system mounted in a trailer (white) on a truck (orange) at the ingv (istituto nazionale di geofisica e vulcanologia) observatory "pizzi deneri" (the volcanic plume of mt. Etna is clearly visible); (b)location of mt. Etna in sicily, southern italy (left inset); the truck was parked at the ingv "pizzi deneri" (right inset); the laser was fired at constant azimuth and different elevations .the volcanic plume of the northeast crater has been crossed by the laser beam. From7° to 9° of elevation, rock faces were encountered

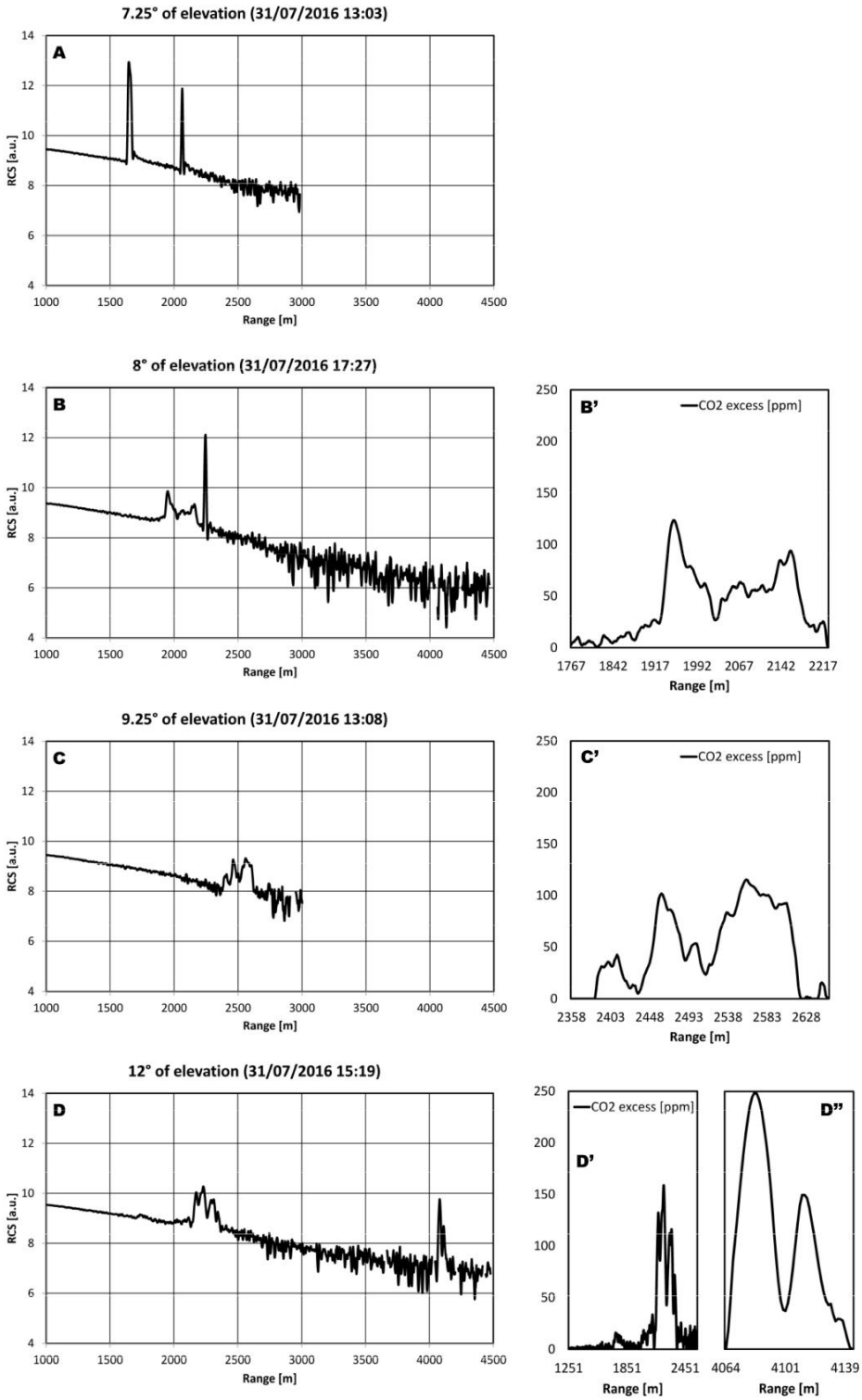

Figure 41(a) lidar return at 7.25° of elevation: two narrow and defined peaks due to beam backscattering from rock faces are clearly visible (beyond 3000 m only noise was recorded and the corresponding signal is not shown); (b) lidar return at 8° of elevation: a wide and jagged peak from the volcanic plume and a narrow and defined peak from a rock face are clearly visible; the co2 profile inside the volcanic plume is shown in (b'); (c) lidar return at 9.25° of elevation: a wide and jagged peak from the volcanic plume is clearly visible; the co2 profile inside the volcanic plume is shown in (c') (beyond 3000 m only noise was recorded and the corresponding signal is not shown); (d) lidar at return at 12° of elevation: two wide and jagged peaks from the volcanic plume are clearly visible; the co2 profiles inside the volcanic plume are shown in (d') and (d").

7.2.2. DIAL

The main components of a lidar are the transmitter (laser) and the receiver (telescope). A lidar is merely an optical radar (Fiorani et al., 2010): a laser pulse is transmitted to the atmosphere, and some of its photons are backscattered to the telescope by air molecules and aerosols (droplets, particles etc.). The optical power corresponding to this photon flux is transformed into an electronic signal by photodetector and preamplifier, and converted in digital signal by an ADC (analog-to-digital converter).

The chemico-physical properties of the atmosphere along the laser beam, at distance R (range) from the lidar, can be inferred from analysis of the detected signal as function t of, the time interval between emission and detection. R and t are linked by the relation $R = ct/2$, where c is the speed of light. The returned signal to the lidars' telescope, as function of R (or t), then yields an atmospheric profile (Figure 41). In other words, an atmospheric profile is a range-resolved characterization of the lidar returned signal, which allows studying the air/plume optical properties along the light trajectory.

Air attenuates the laser pulse due to molecules and aerosol scattering and to the specific absorption of gases: if the laser wavelength coincides with absorption lines of a target gas attenuation will be stronger. A DIAL takes advantage of this effect: unlike a usual lidar, two wavelengths, ON and OFF, are transmitted, with only the former being absorbed by the target gas (Figure 42).

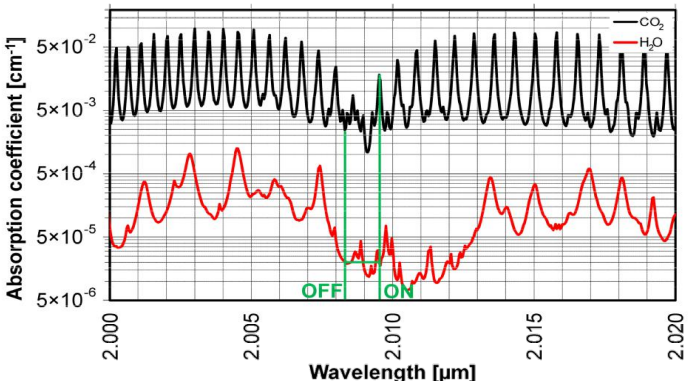

Figure 42 carbon dioxide and water vapor absorption coefficients around the on and off wavelengths (indicated in green).

If the absorption line is narrow, and ON and OFF wavelengths are close enough, the target gas concentration along the lidar optical path can be derived from the ratio between the OFF and ON signals. In this application, we selected the following wavelengths (Figure 42): ON, 2009.537 nm; OFF, 2008.484 nm. This selection was motivated by: (i) the CO_2 absorption is relatively low, thus the system to probe far ranges (beyond 4 km). If a stronger line had been used, the ON laser pulse would have extinguished before; (ii) the beam energy

(depending mainly on the dye efficiency curve) and the detector responsivity are near their maximum; and (iii) the H_2O absorption is very low (Figure 42). Moreover, ON and OFF have been chosen so that the differential absorption of H_2O is approximately zero (within the uncertainty of the spectroscopic data), thus minimizing the interference of water vapour to the carbon dioxide measurement.

In our case, the transmitter and the receiver are coaxial, and the lidar field-of-view can be aimed in the whole atmosphere thanks to a system made of two large elliptical mirrors (Fiorani et al., 2015). This configuration allows the experimenters to scan the plume in both horizontal and vertical planes, thus measuring CO_2 concentrations both outside and inside the volcanic plume (Aiuppa et al., 2015). From this, by scanning the volcanic gas plume from different angles and viewing directions, the CO_2 distribution in a cross-section of the volcanic plume can be retrieved. This, combined with independent knowledge of plume speed and altitude, allows the CO_2 flux to be retrieved.

The reader is referred to previous work (Aiuppa et al., 2015; Fiorani et al., 2015; Aiuppa et al., 2017) for details on instrumental setup and data processing. The systematic error associated with the derived CO_2 concentrations is dominated by imprecision in wavelength setting (Fiorani et al., 2015). This leads to inaccuracy in the differential absorption cross section, and thus in gas concentration. Thanks to a photo-acoustic cell filled with pure CO_2 at atmospheric pressure and temperature, the ON and OFF wavelengths were set before each atmospheric scan. The residual imprecision (Fiorani et al.,2016) of 0.02 cm 1 (half laser linewidth: half width at half maximum of the energy transmitted by the laser system (J) vs the wavenumber (cm 1)) implies a systematic error on CO_2 concentrations of 5.5%. The statistical error of CO_2 measurement has been calculated by usual error propagation techniques from the standard deviation of the lidar signal. At 2.5 km, a mean range, it is about 2%, while it can exceed 5% at 4.2 km. Table 1 compares the instrumental set-up during the Mt. Etna field campaign, with those used at Solfatara Aiuppa et al., 2015 Fiorani et al., 2015), and Stromboli (Fiorani et al., 2015; 2016).

Table 1. *Summary of field operational conditions at Pozzuoli Solfatara, Stromboli, and Mt. Etna (this study).*

Campaign	Pozzuoli Solfatara	Stromboli Volcano	Mt. Etna
Latitude	40° 49’46.28’N	38° 48’06.69’’N	37° 45’57.28’’N
Longitude	14° 08’ 50.51’’E	15° 14’25.69’’E	15° 00’59.65’’E
Period	13–17 October 2014	24–29 June 2015	28 July–1 August 2016
Azimuth scan	196° –234°	235.3° –253.6°	230°
Elevation scan	0° –18°	15.2° –27.4°	7° –14°

7.3 Results

Figure 41 shows examples of lidar returns obtained during our Etna campaign. Results are illustrated for four atmospheric profiles taken on 31 July (the best measurement day) at four distinct elevations, and are shown in the form of range vs. RCS (range corrected signal) scatter plots. During its atmospheric propagation, the laser beam intensity approximately decreased:

- exponentially, due to atmospheric extinction, according to the Lambert-Beer law, and;
- as $1/R^2$, because the solid angle subtended by the receiver is A/R^2, where A is the telescope effective area.

For these reasons, it is a common practice in lidar science to express results using a RCS, this being the logarithm of the product of the signal times the square of the range. To improve the SNR (signal-to-noise ratio), the RCS was obtained by averaging 50 laser shots for each lidar return, and a 13-point Savitzky-Golay filter was applied (Schafer 2011).

During a vertical scan, the measured range-resolved RCS profiles varied as the laser elevation was sequentially increased. Below 7.25 elevation, the laser beam hit a first rock surface at about a 1.6 km distance. Laser beam retro-reflection at this rock surface produced, in the lidar return signal, a strong, narrow RCS peak at R = 1.6 km. At 7.25 elevation (Figure 41a), only part of the beam was intercepted by the R = 1.6 km rock surface, while the remaining part impinged on the rock surface at R = 2.1 km, producing a second narrow RCS peak. For geometrical reasons, an elevation increase corresponded to an increase in the range at which the rock surfaces were encountered, e.g., the second rock surface was encountered at R = 2.1 at 7.25 elevation, shown in Figure 41a, and at R = 2.3 km at 8 elevation, shown in Figure 41b. No rock surface was hit by the laser beam at elevations >9, e.g., note the absence of narrow RCS peaks in Figure 41c, d.

Back-scattering of the laser beam by the volcanic plume produced wide and jagged RCS peaks, therefore very distinct from the narrow and defined peaks produced by beam retro-reflection at rock surfaces (compare the two peak shapes in Figure 41b).

The volcanic plume was detected at range distances in between the two rock surfaces up to a 9 elevation (e.g., Figure 41b), or beyond them at a 9 to 14 elevation (Figure 41c, d). A broad, irregular RCS peak in the lidar returns, corresponding to the volcanic plume, was resolved up to a maximum measurement range of 4.2 km (Figure 41d).

We used the procedure detailed in References (Aiuppa et al., 2015; Aiuppa et al., 2017) to convert the RCS profiles into range-resolved profiles of in-plume excess CO_2

concentrations (see Figure 41b', c',d',d"). This procedure involves calculating the excess CO_2 concentration corresponding to each i-th ADC channel of the lidar profile from:

$$C_{CO2,I}=kRCS_i \quad \text{(eq. 8)}$$

$$K = \frac{\Delta C(R_1 - R_2)}{\Delta R \sum_i RCSi} \quad \text{(eq. 9)}$$

where DR and RCS_i are, respectively, the range interval and range corrected signal corresponding to each ADC channel; R_1 and R_2 are the range distances of the two above rock surfaces; and DC is the average excess CO_2 concentration in the air/plume parcel between them (this is obtained from the intensity contrast of lidar returns produced by the two rock surfaces). The term "excess" implies that the reported CO_2 concentrations are after subtraction of the ambient atmospheric background, and therefore correspond to the "volcanic" CO_2 levels in the plume. The ambient atmospheric CO_2 background was obtained from the processing of lidar returns in the 0–1.6 km range distance, where no plume signal was detected (see Reference Aiuppa et al., 2015 for details of calculations).

At an 8 elevation, shown in Figure 41b', the volcanic plume was evidenced by a band of excess CO_2 concentrations of 125 ppm. These excess CO_2 concentrations agree well with those derived by in situ in-plume measurements with conventional techniques (e.g., the Multi-GAS), from which in-plume CO_2 concentrations of tens to hundreds of ppm above ambient air are typically obtained (Aiuppa et al., 2006). The plume appears to be about 300 m thick; this relatively narrow plume's cross-section was probably justified by the fact that, at such an 8 elevation, the laser beam intercepted the volcanic plume at below the summit crater's rim altitude. Due to its close proximity to the crater slopes, the volcanic plume was, at least partly, protected from the local wind field, a fact that reduced its atmospheric dispersion. The volcanic plume was still relatively narrow at a ~9 elevation (Figure 41c'), where the laser beam pointed just above the summit crater's rim. At even higher elevations, the volcanic plume was wider and scattered by the wind, and the returned RCS often presented multiple peaks (Figure 41 d,d').

As explained before (Section 8.2), a sequence of atmospheric profiles was acquired as the lidar vertically scanned the horizon, from a 7 to 14 (max) elevation. All CO_2 profiles (e.g., Figure 41), taken at different elevations during a single lidar rotation sequence, were combined and integrated to obtain a CO_2 scan, examples of which are illustrated in Figure 43. On 31 July 2016, the most fruitful day, 19 scans were obtained. Each scan consisted of 24 profiles, all at a 230 azimuth. These profiles covered the elevation angle interval (between 7° and 13°) with an angular resolution of about 0.25°.

The results are illustrated in the form of contour maps of excess CO_2 concentrations, plotted as a function of the range and elevation. The coloured spots correspond to areas of high excess CO_2 (the natural background is dark blue), and therefore illustrate the spatial distribution and temporal evolution of the volcanic plume (the yellow lines delimit the positions of the laser beam reflections off the rock surfaces). In all the maps we obtained (see examples in Figure 43), the structure of the plume was well resolved. The plume was tracked as a cluster of high CO_2 concentration spots, trending from about a 9° elevation and R = 2.4 km (the vent rim) to a 13° elevation and R = 2.5–2.9 km. As such, our CO_2 concentration maps were consistent with a gently lofting volcanic plume (Figure 43), with vertical and horizontal movements driven by thermal buoyancy and by the local wind field pattern. The maps indicate the plume was being dispersed away from the lidar during our observations, since the range of volcanic plume detection increased with the elevation in all the maps.

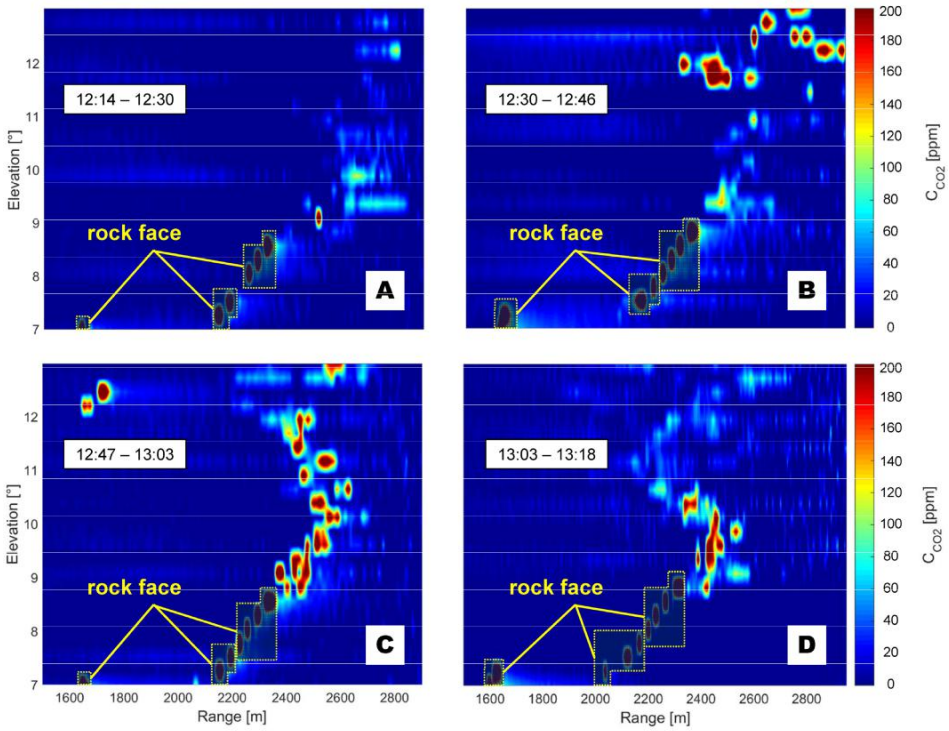

Figure 43 vertical scans (fixed azimuth: 230°) of the volcanic plume (co2 excess) acquired on 31 july 2016; (a) from 12:14 p.m. To 12:30 p.m.; (b) from 12:30 p.m. To 12:46 p.m.; (c) from 12:47 p.m. To 1:03 p.m. And (d) from 1:03 p.m. To 1:18 p.m. (local civil time). At this azimuth, in the elevation interval between 7° and 9°, the laser beam is back-scattered by rock faces, thus causing signal peaks not due to the volcanic plume (rock faces are sorted out from real co2 by the correspondence of narrow peaks with certain range values).

The maps of Figure 43 set the basis for the calculation of the volcanic CO_2 flux. In analogy with previous work (Aiuppa et al., 2015), we obtained the volcanic CO_2 flux by integrating the background-corrected (excess) CO_2 concentrations over a plume cross-section (from the maps of Figure 43), which allowed us to derive the plume CO_2 molecular

density. This was then multiplied by the plume transport speed to obtain the CO_2 flux (ΦCO_2, in Kg/s), as

$$\Phi_{CO_2} = v_p \cdot \frac{PM_{CO_2}}{10^3 N_A} \cdot N_{molCO2-total} \quad \text{(eq. 10)}$$

where vp is the plume transport speed (in m/s); $NmolCO_2$−total is the total-plume CO_2 molecular density (expressed in molecules·m^{-1}); and $1PMCO_2$ and NA are, respectively, the CO_2 molecular weight and Avogadro's constant. The term N was obtained by integrating the effective average excess $molCO_2$ total CO_2 concentrations (C_{exc} [ppm]) over the entire plume cross-section, according to:

$$N_{molCO2-total} = N_h \cdot 10^{-6} \cdot \sum_i \overline{C_{exc,i}} \cdot A_i \quad \text{(eq 11)}$$

where Nh is the atmospheric number density (molecules·m−33) at the crater's summit height, and Ai represents the ii-th effective plume area.

The plume transport speed was inferred at 9.7 ± 0.8 m/s from the processing of plume images taken on the same day by the permanent UV camera system (UV4) in use at the Pizzi Deneri observatory since 2014; see Reference (D'Aleo et al., 2016) for details on the instrument. The UV camera images were processed using an optical flow sub-routine using the Lukas/Kanade algorithm (Bruhn et al., 2005; Peters et al., 2015), integrated in the Vulcamera software (Tambuello et al., 2011) (same methodology as described in D'Aleo et al., 2016).

Our derived CO_2 fluxes are illustrated in Figure 44. The CO_2 flux varied from 1235 to 8050 tons/day during the measurement interval, and averaged at 2850 ± 1800 tons/day.

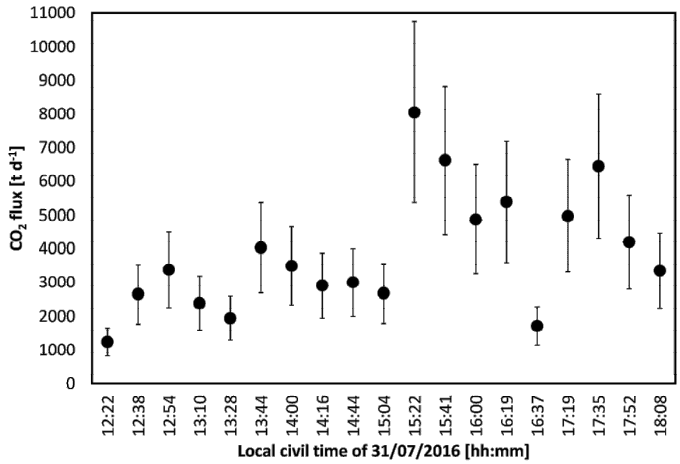

Figure 44 co2 flux from the northeast crater retrieved on 31 july 2016 from 12:22 p.m. To 6:08 p.m. (local civil time). The error bars indicate the inferred co2 flux error (±33%), as based upon the error propagation of the plume speed an in—plume integrated co_2 amounts (procedure detailed in aiuppa et al., 2017.

7.4 Discussions

As long-term volcanic gas records have increased in number and quality over the last few decades (Fisher et al., 2015) full empirical evidence has emerged for precursory increases of the volcanic CO_2 flux emissions prior to eruption of mafic to intermediate volcanoes (Aiuppa et al., 2011). However, remote direct measurements of the volcanic CO_2 flux, which are intrinsically safer for operator and more prone to provide continuous, long--term observations, have remained impossible until recently (Aiuppa et al., 2015; Queiber et al., 2016).

Our results here support the ability of the DIAL-Lidar BILLI to profile atmospheric CO_2 concentrations over large optical paths (Figures 41 and 43), and to remotely sense the CO_2 flux from distal (up to 44 km distant) sources (Figure 44). This instrument thus promises a real step ahead in the remote observation of volcanic gas emissions. Improved CO_2 flux measurements are not only vital for better gas-based volcano monitoring, but are also needed to better constrain the global volcanic CO_2 budget, which is still inaccurately known (Burton et al., 2013).

The volcanic CO_2 flux from Mt. Etna has been assessed in the past by either in -plume airborne CO_2 profiling (Allard et al., 1991) or by indirect methods involving in situ measurements of plume CO_2/SO_2 ratios, via either the Multi--GASS (Aiuppa 2015; Aiuppa et al., 2016; Pering et al., 2014) or Fourier Transform InfraRed Spectrometers (FTIR; (La Spina et al., 2010)). To the best of our knowledge, our results are the first to report, a direct, remote quantification of Etna's CO_2 flux.

Our lidar results show that, in the circa 5-h-long observational widow, the CO_2 flux from Etna's northeast crater varied from 1235 to 8050 tons/day (Figure 44). The CO_2 flux was somewhat higher, typically >4000 tons/day and up to 8050 tons/day, after 3 p.m. local time, relative to the 12–3 p.m. period (<4000 tons/day) (Figure44). No change in activity was yet observed at the northeast crater, which continued to exhibit quiescent degassing over the entire measurement interval. We therefore consider the observed variation as part of the normal fluctuations in degassing activity that occur at Etna, likely in response to temporal variations in the magma/gas transport rate in the volcano's feeding conduits (Pering et al., 2014; Allard et al., 2006). By taking the arithmetic mean of the individual CO_2 flux measurements Figure 44, we would obtain time-averaged CO_2 flux of 2850 ±1800 tons/day for31 July 2016. In view of the non- stationary CO_2 emission behaviour captured by our high-temporal resolution measurement (Figure 44), we also perform an independent exercise

in which we calculated the total CO_2 output from the northeast crater by integrating (in the time domain) the available CO_2 flux measurements, each measurement, each representative of 13–18 min of observation (the mean duration of scans was 15 min).

From this, we obtained that ≈796 tons of CO_2 were cumulatively released during 5 h of observations, implying a time-averaged CO_2 flux of 3900 tons/day. This is about 30% higher than, but within one standard deviation of, the CO_2 flux obtained above from a simple arithmetic mean approach (2850 18002 tons/day)

In the attempt to add confidence to our results, we compared our lidar-based CO2 flux with independent estimates based upon a more conventional technique that involves a combination of fluxes and plume CO_2 /SO_2 ratios (Figure 45). Our permanent UV camera system (UV4) at Pizzi Deneri indicated, for the morning of the same 31 July, a time-averaged SO_2 flux of 645 ± 125 tons/day. This the mean (±1 standard deviation) of 4 h of observations at a 0.5 Hz rate (Figure 45; same methodology as in D'Aleo et al., 2016). Our inferred northeast crater's SO_2 flux (645 ± 125 tons/day) corresponded to about 30% of the total volcano's SO_2 emissions (≈2200 tons/day). These latter emissions were inferred using the same UV camera system, and were thus primarily determined by the central craters (not targeted by our DIAL-Lidar). The northeast crater's volcanic plume was in situ measured by a portable Multi-GAS instrument (the same as in (Aiuppa et al., 2006,2008)) two days later. These in situ observations yielded a (molar CO_2/SO_2 ratio of ≈6, demonstrating the usual (Aiuppa et al., 2006; La Spina 2010) CO_2-poor composition of the northeast (the simultaneously observed CO_2/SO_2 ratio of the central crater's plume was ≈16). We consider our Multi-GAS–derived composition on 2 August as still representative of the northeast crater's emissions on 31 July, since volcanic activity at that crater did not exhibit any substantial change in between the two days. By combining the two sets of data together, we converted the SO_2 flux time- series into a 4-h-long CO_2 flux time-series (Figure 45), from which an averaged (arithmetic mean) UV-Camera + MultiGAS CO_2 flux of ≈2750 tons/day was obtained. This is close to our lidar-based estimates above (≈2850–3900 tons/day). We caution that the two independent CO_2 flux time-series (from lidar and UV-Camera + MultiGAS) are not temporally overlapping, since the UV camera system ran only in the morning, when sunlight conditions were optimal (D'Aleo et al., 2016) while our successful CO_2 flux measurement with the lidar started a few hours later in the afternoon. In addition, the UV-Camera + MultiGAS used a constant CO_2/SO_2 ratio (of six) throughout the entire UV camera temporal window, while it is valid only as a first approximation. However, the

close CO_2 flux values inferred from lidar and UV-Camera + MultiGAS provide mutual validation for the two independent techniques.

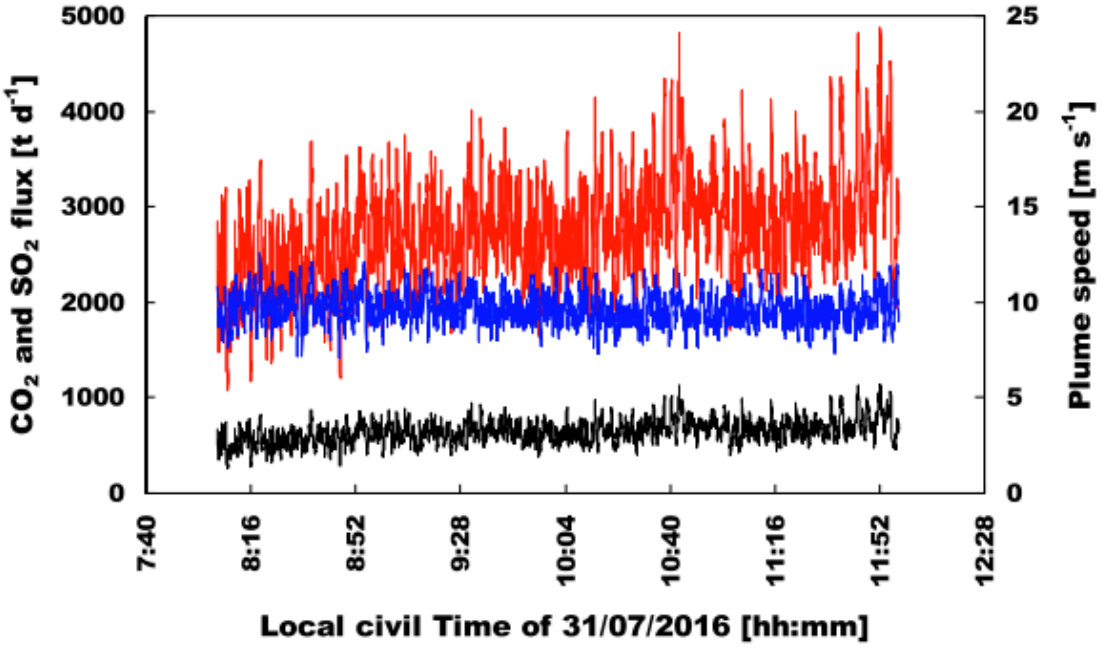

Figure 45 time-series of co2 flux emissions from the northeast crater (in red) obtained from the uv camera + multi-gas technique. These were calculated by converting the so flux time-series (in black) obtained by the uv4 permanent uv camera system on 31 july 2016 (from 8 a.m. To 12 p.m., local civil time) using a co /so ratio (molar) of six. The plume speed time-series calculated from the uv camera on the same 31 july is also shown (blue trend).

7.5. Conclusions

We have shown for the first time that the volcanic CO_2 flux can be detected with lidar from up to a 4 km distance. During our Mt. Etna field campaign, our DIAL-Lidar BILLI vertically scanned the volcanic plume while profiling CO_2 concentrations every 10 s, with a spatial resolution of 5 m. With this configuration, we successfully detected an excess volcanic CO_2 signal of a few tens of ppm, with relatively low systematic and statistical errors (5.5% and 2%, respectively). By integrating the results of the atmospheric profile taken at different heading angles, and covering a full scan of the plume, the volcanic CO_2 flux was derived (after integration, and in combination with the plume transport speed) at 2850–3900 tons/day. This lidar-based flux is close to that independently obtained by in situ observations of the volcanic plume (2750 tons/day), which combined Multi-GAS in situ sensing of the plume composition and remotely sensed (UV camera) SO_2 fluxes.

Clearly, additional field tests are required to validate our novel technique even further. Still, our results suggest BILLI is a major advance in ground-based observations of volcanic plumes. The instrument allows the remote measurements of volcanic CO_2 (and particles, if desired) from distal (safe) areas, and with unprecedented temporal resolution and high

spatial coverage. Further development is now required to make this technology an operational tool for routine volcanic gas observations. Efforts are currently being undertaken to reduce the weight and power requirements (the current prototype is ~1100 kg and requires 6.5 kW), and to implement more user-friendly operational routines and software. These implementations are required to widen the application range of the lidar, and to allow its use in remote/harsh volcanic environments.

Chapter 8
Conclusions

In this study, I have taken advantage of the much improved spatial (~5 m) and temporal (~1 Hz) resolution of UV cameras to systematically investigate SO_2 gas emissions from Etna's during 2014-2016. I have shown that vent-resolved SO_2 flux time-series can allow capturing rapid (hours/days) switch in degassing/eruptive activity from one active vent to another. The SO_2 flux time-series obtained in 2014-2016 has been successfully integrated with geophysical datasets to unravel inter-connections between individual craters (e.g., EF vs NEC; EF vs NSEC, VOR and NSEC). The different craters share a single gas source, and must be inter-connected at some level in the Etna's shallow plumbing system. In turn, the camera's high temporal resolution paves the way to measuring transition from passive degassing to explosive in a more effective way.

I have reported on the first gas flux measurements are for the Etna's NSEC, both during quiescence and eruption. These have allowed to characterize the degassing behaviour of Etna's recently most frequently erupting vent, and to investigate timescales for its transition from quiescence to eruption. SO_2 flux records indicate that the NSEC contributes little or no gas during quiescence, to become a substantial SO_2 degassing source only in the days prior to its eruptions, and during its paroxysmal phases. I conclude that UV cameras open new prospects for identifying short-term gas flux variations prior to paroxysmal NSEC eruptions.

The ground-based monitoring network I report on in this dissertation has contributed, in December 2015, the first SO_2 flux observations during an Etna paroxysmal lava fountaining episode. SO_2 flux records taken on December 4 2015 indicate peak SO_2 emissions of ~400 kg/s during a lava fountain, and constrain the total magmatic gas output during a paroxysm at ~10^9 m^3.

The complex 2016 eruptive sequence was also studied. Three different behaviours were observed: a very rapid SO_2 flux variation *during* the May paroxysmal sequence, a much slower SO_2 flux increase weeks prior to mild strombolian activity in August, and a gradual SO_2 flux decrease in October-December 2016 paralleling subsidence of the inner central crater's floor. I have concluded that different velocities of magma ascent/decompression inside the volcano produce different types of SO_2 flux variations: fast ascent of gas-rich magma prior to a lava fountain can only produce short-term precursory SO_2 signal

(timescales of hours to a day), while more slowly moving magma leading to milder strombolian activity can be preceded by SO_2 flux variations weeks in advance.

To better constrain magma dynamic, it is mandatory to use different gas species that exsolve at different depths, in order to retrieve information on the different portions of the plumbing system. While studying CO_2 is highly desirable at this aim, remotely sensing this gas has been technically challenging to date. To overcome these difficulties, a new D IAL-Lidar was developed that can scan CO_2 concentrations in a volcanic plume. These, combined with UV camera derived plume speeds, allows to directly quantifying the volcanic CO_2 flux from a remote location for the first time.

The results presented have contributed novel piece of information of SO_2 flux dynamics on Mount Etna, and have confirmed the utility of UV cameras in volcano monitoring.

References

Aiuppa, A. et al., 2017. New Advances in Dial-Lidar-Based Remote Sensing of the Volcanic CO2 Flux. *Frontiers in Earth Science*, 5(February), pp.1–13. Available at: http://journal.frontiersin.org/article/10.3389/feart.2017.00015/full.

Aiuppa, A. et al., 2015. New ground-based lidar enables volcanic CO<inf>2</inf> flux measurements. *Scientific Reports*, 5, pp.1–12. Available at: http://dx.doi.org/10.1038/srep13614.

Aiuppa, a. et al., 2011. Hydrogen in the gas plume of an open-vent volcano, Mount Etna, Italy. *Journal of Geophysical Research: Solid Earth*, 116(10), pp.1–8.

Aiuppa, a. et al., 2010. Patterns in the recent 2007-2008 activity of Mount Etna volcano investigated by integrated geophysical and geochemical observations. *Geochemistry, Geophysics, Geosystems*, 11(9), pp.1–13.

Aiuppa, a. et al., 2006. Rates of carbon dioxide plume degassing from Mount Etna volcano. *Journal of Geophysical Research: Solid Earth*, 111(9), pp.1–8.

Aiuppa, a. et al., 2008. Total volatile flux from Mount Etna. *Geophysical Research Letters*, 35(24), pp.2004–2008.

Allard, P. et al., 2016. Degassing dynamics of basaltic lava lake at a top-ranking volatile emitter: Ambrym volcano, Vanuatu arc. *Earth and Planetary Science Letters*, 448, pp.69–80. Available at: http://www.sciencedirect.com/science/article/pii/S0012821X16302230.

Allard, P., 1997. Endogenous magma degassing and storage at Mount Etna. *Geophysical Research Letters*, 24(17), pp.2219–2222. Available at: http://dx.doi.org/10.1029/97GL02101.

Allard, P. et al., 1991. Eruptive and diffuse emissions of CO2 from Mount Etna. *Nature*, 351(6325), pp.387–391.

Allard, P. et al., 2006. Mount Etna 1993-2005: Anatomy of an evolving eruptive cycle. *Earth-Science Reviews*, 78(1–2), pp.85–114.

Allard, P., Burton, M. & Muré, F., 2005. Spectroscopic evidence for a lava fountain driven by previously accumulated magmatic gas. *Nature*, 433(7024), pp.407–410.

Aloisi, M. et al., 2002. Seismic tomography of the crust underneath the Etna volcano, Sicily. *Physics of the Earth and Planetary Interiors*, 134(3), pp.139–155. Available at: http://www.sciencedirect.com/science/article/pii/S003192010200153X.

Alparone, S. et al., 2003. Relationship between tremor and volcanic activity during the Southeast Crater eruption on Mount Etna in early 2000. *Journal of Geophysical Research: Solid Earth*, 108(B5), pp.1–13. Available at: http://doi.wiley.com/10.1029/2002JB001866.

Andò, B. & Pecora, E., 2006. An advanced video-based system for monitoring active volcanoes. *Computers & geosciences*, 32(1), pp.85–91.

Andronico, D. & Corsaro, R.A., 2011. Lava fountains during the episodic eruption of South–East Crater (Mt. Etna), 2000: insights into magma-gas dynamics within the shallow volcano plumbing system. *Bulletin of volcanology*, 73(9), pp.1165–1178.

Behncke, B. et al., 2014. The 2011-2012 summit activity of Mount Etna: Birth, growth and products of the new SE crater. *Journal of Volcanology and Geothermal Research*, 270(May 1971), pp.10–21. Available at: http://dx.doi.org/10.1016/j.jvolgeores.2013.11.012.

Behncke, B. et al., 2006. The exceptional activity and growth of the Southeast Crater, Mount Etna (Italy), between 1996 and 2001. *Bulletin of Volcanology*, 69(2), pp.149–173.

Behncke, B., Falsaperla, S. & Pecora, E., 2009. Complex magma dynamics at Mount Etna

revealed by seismic, thermal, and volcanological data. *Journal of Geophysical Research: Solid Earth*, 114(B3).

De Beni, E. et al., 2005. New results of 40Ar/39Ar dating constrain the timing of transition from fissure-type to central volcanism at Mount Etna (Italy). *Terra Nova*, 17(3), pp.292–298.

De Beni, E. et al., 2015. The continuing story of Etna's New Southeast Crater (2012-2014): Evolution and volume calculations based on field surveys and aerophotogrammetry. *Journal of Volcanology and Geothermal Research*, 303(February 2013), pp.175–186. Available at: http://dx.doi.org/10.1016/j.jvolgeores.2015.07.021.

Bluth, G.J.S. et al., 2006. Development of an ultra-violet digital camera for volcanic SO2 imaging. *Journal of Volcanology and Geothermal Research*, 161(1–2), pp.47–56.

Bonaccorso, A., 2014. Eruptive processes leading to the most explosive lava fountain at Etna volcano: The 23 November 2013 episode. *Geophysical Research Letters*, (41), pp.4912–4919.

Bonaccorso, A. et al., 2004. Intrusive mechanisms at Mt. Etna forerunning the July-August 2001 eruption from seismic and ground deformation data. *Pure and Applied Geophysics*, 161(7), pp.1469–1487.

Bonaccorso, A. et al., 2011. The initial phases of the 2008-2009 Mount Etna eruption: A multidisciplinary approach for hazard assessment. *Journal of Geophysical Research: Solid Earth*, 116(3), pp.1–19.

Bonaccorso, A. & Calvari, S., 2017. A new approach to investigate an eruptive paroxysmal sequence using camera and strainmeter networks: Lessons from the 3–5 December 2015 activity at Etna volcano. *Earth and Planetary Science Letters*, 475, pp.231–241. Available at: http://linkinghub.elsevier.com/retrieve/pii/S0012821X17303989.

Bonaccorso, A. & Calvari, S., 2013. Major effusive eruptions and recent lava fountains: Balance between expected and erupted magma volumes at Etna volcano. *Geophysical Research Letters*, 40(23), pp.6069–6073.

Branca, S. et al., 2008. Geological evolution of Mount Etna volcano (Italy) from earliest products until the first central volcanism (between 500 and 100 ka ago) inferred from geochronological and stratigraphic data. *International Journal of Earth Sciences*, 97(1), pp.135–152.

Branca, S. & Del Carlo, P., 2004. Eruptions of Mt. Etna during the past 3,200 years: a revised compilation integrating the historical and stratigraphic records. *Mt. Etna: volcano laboratory*, pp.1–27.

Branca, S. & Del Carlo, P., 2005. Types of eruptions of Etna volcano AD 1670–2003: implications for short-term eruptive behaviour. *Bulletin of Volcanology*, 67(8), pp.732–742.

Bruhn, A., Weickert, J. & Schörr, C., 2005. Lucas / Kanade Meets Horn / Schunck : Combining Local and Global Optic Flow Methods. *International Journal of Computer Vision*, 61(3), pp.211–231.

Bruno, N., Caltabiano, T. & Romano, R., 1999. SO2 emissions at Mt. Etna with particular reference to the period 1993–1995. *Bulletin of Volcanology*, 60(6), pp.405–411.

Burton, M.R. et al., 2015. SO2 flux monitoring at Stromboli with the new permanent INGV SO2 camera system: A comparison with the FLAME network and seismological data. *Journal of Volcanology and Geothermal Research*, 300, pp.95–102. Available at: http://dx.doi.org/10.1016/j.jvolgeores.2015.02.006.

Burton, M.R., Sawyer, G.M. & Granieri, D., 2013. Deep carbon emissions from volcanoes. *Reviews in Mineralogy and Geochemistry*, 75(1), pp.323–354.

Caltabiano, T. et al., 2004. Volcanic Gas Emissions from the Summit Craters and Flanks of Mt. Etna, 1987–2000. In *Mt. Etna: Volcano Laboratory*. American Geophysical

Union, pp. 111–128. Available at: http://dx.doi.org/10.1029/143GM08.
Caltabiano, T., Romano, R. & Budetta, G., 1994. SO2 flux measurements at Mount Etna (Sicily). *Journal of Geophysical Research: Atmospheres*, 99(D6), pp.12809–12819.
Calvari, S. et al., 2011. An unloading foam model to constrain Etna's 11-13 January 2011 lava fountaining episode. *Journal of Geophysical Research: Solid Earth*, 116(11), pp.1–18.
Calvari, S. et al., 2004. Valle del Bove, eastern flank of Etna volcano: a comprehensive model for the opening of the depression and implications for future hazards. *Mt. Etna: volcano laboratory*, pp.65–75.
Calvari, S. & Pinkerton, H., 2004. Birth, growth and morphologic evolution of the "Laghetto"cinder cone during the 2001 Etna eruption. *Journal of Volcanology and Geothermal Research*, 132(2–3), pp.225–239.
Cannata, A. et al., 2011. Clustering and classification of infrasonic events at Mount Etna using pattern recognition techniques. *Geophysical Journal International*, 185(1), pp.253–264.
Cannata, A. et al., 2009. Long period and very long period events at Mt. Etna volcano: Characteristics, variability and causality, and implications for their sources. *Journal of Volcanology and Geothermal Research*, 187(3), pp.227–249.
Carn, S.A. et al., 2017. A decade of global volcanic SO(2) emissions measured from space. *Scientific Reports*, 7, p.44095. Available at: http://www.ncbi.nlm.nih.gov/pmc/articles/PMC5343458/.
Carn, S.A. et al., 2017. A decade of global volcanic SO2emissions measured from space. *Scientific Reports*, 7, pp.1–12.
Carn, S.A. et al., 2008. Daily monitoring of Ecuadorian volcanic degassing from space. *Journal of Volcanology and Geothermal Research*, 176(1), pp.141–150.
Carn, S.A. et al., 2015. Extending the long-term record of volcanic SO2 emissions with the Ozone Mapping and Profiler Suite nadir mapper. *Geophysical Research Letters*, 42(3), pp.925–932.
Carn, S.A. et al., 2013. Measuring global volcanic degassing with the Ozone Monitoring Instrument (OMI). *Geological Society, London, Special Publications*, 380(1), pp.229–257.
Carn, S.A., Clarisse, L. & Prata, A.J., 2016. Multi-decadal satellite measurements of global volcanic degassing. *Journal of Volcanology and Geothermal Research*, 311, pp.99–134.
Chester, D.K. et al., 2012. *Mount Etna: the anatomy of a volcano*, Springer Science & Business Media.
Chester, D.K. et al., 1985. *Mount Etna: the anatomy of a volcano*, Springer Science & Business Media.
Christopher, T. et al., 2010. Volcanic gas emissions from Soufrière Hills Volcano, Montserrat 1995-2009, with implications for mafic magma supply and degassing. *Geophysical Research Letters*, 37(3), pp.1–5.
Coltelli, M. et al., 2017. The Use of Surveillance Cameras for the Rapid Mapping of Lava Flows: An Application to Mount Etna Volcano. *Remote Sensing* , 9(3).
Coltelli, M., Carlo, P. Del & Vezzoli, L., 1998. Discovery of a Plinian basaltic eruption of Roman age at Etna volcano, Italy. *Geology*, 26(12), pp.1095–1098.
Coppola, D. et al., 2016. Enhanced volcanic hot-spot detection using MODIS IR data: results from the MIROVA system. *Geological Society, London, Special Publications*, 426(1), pp.181–205.
Coppola, D. et al., 2015. Enhanced volcanic hot-spot detection using MODIS IR data: results from the MIROVA system. *Geological Society, London, Special Publications*, p.SP426.5-. Available at:

http://sp.lyellcollection.org/content/early/2015/05/12/SP426.5.abstract.
Coppola, D. et al., 2017. Shallow system rejuvenation and magma discharge trends at Piton de la Fournaise volcano (La Réunion Island). *Earth and Planetary Science Letters*, 463, pp.13–24. Available at: http://www.sciencedirect.com/science/article/pii/S0012821X17300365.
Coppola, D. & Cigolini, C., 2013. Thermal regimes and effusive trends at Nyamuragira volcano (DRC) from MODIS infrared data. *Bulletin of volcanology*, 75(8), p.744.
Corsaro, R.A. et al., 2017. Monitoring the December 2015 summit eruptions of Mt. Etna (Italy): Implications on eruptive dynamics. *Journal of Volcanology and Geothermal Research*, (December 2015). Available at: http://linkinghub.elsevier.com/retrieve/pii/S0377027316304048.
Corsaro, R.A. et al., 2009. Petrology of lavas from the 2004–2005 flank eruption of Mt. Etna, Italy: inferences on the dynamics of magma in the shallow plumbing system. *Bulletin of Volcanology*, 71(7), pp.781–793.
Corsaro, R.A. & Cristofolini, R., 1997. Geology, geochemistry and mineral chemistry of tholeiitic to transitional Etnean magmas. *Acta Vulcanologica*, 9, pp.55–66.
Corsaro, R.A. & Cristofolini, R., 2000. Subaqueous volcanism in the Etnean area: evidence for hydromagmatic activity and regional uplift inferred from the Castle Rock of Acicastello. *Journal of volcanology and geothermal research*, 95(1–4), pp.209–225.
Corsaro, R.A. & Pompilio, M., 2004. Dynamics of Magmas at Mount Etna. In *Mt. Etna: Volcano Laboratory*. American Geophysical Union, pp. 91–110. Available at: http://dx.doi.org/10.1029/143GM07.
D'Aleo, R. et al., 2016. Spatially resolved SO2 flux emissions from Mt Etna. *Geophys. Res. Lett.*, 43, pp.7511–7519.
Daag, A.S. et al., 1996. Monitoring Sulfur Dioxide Emission at Mount Pinatubo. *Fire and mud: eruptions and lahars of Mount Pinatubo, Philippines*, (January).
Dalton, M.P. et al., 2010. Multiparameter quantification of gas release during weak Strombolian eruptions at Pacaya Volcano, Guatemala. *Geophysical Research Letters*, 37(9).
Delle Donne, D. et al., 2017. Exploring the explosive-effusive transition using permanent ultraviolet cameras. *Journal of Geophysical Research: Solid Earth*, (Figure 1), pp.4377–4394.
Dubosclard, G. et al., 2004. Doppler radar sounding of volcanic eruption dynamics at Mount Etna. *Bulletin of Volcanology*, 66(5), pp.443–456.
Eatough, D.J., Caka, F.M. & Farber, R.J., 1994. The conversion of SO2 to sulfate in the atmosphere. *Israel Journal of Chemistry*, 34(3-4), pp.301–314.
Edmonds, M. et al., 2003. Automated, high time resolution measurements of SO2 flux at Soufrière Hills Volcano, Montserrat. *Bulletin of Volcanology*, 65(8), pp.578–586.
Edmonds, M., 2008. New geochemical insights into volcanic degassing. *Philosophical transactions. Series A, Mathematical, physical, and engineering sciences*, 366(1885), pp.4559–4579.
Faloona, I. et al., 2009. Sulfur dioxide in the tropical marine boundary layer: dry deposition and heterogeneous oxidation observed during the Pacific Atmospheric Sulfur Experiment. *Journal of Atmospheric Chemistry*, 63(1), pp.13–32. Available at: https://doi.org/10.1007/s10874-010-9155-0.
Ferlito, C., Viccaro, M. & Cristofolini, R., 2009. Volatile-rich magma injection into the feeding system during the 2001 eruption of Mt. Etna (Italy): Its role on explosive activity and change in rheology of lavas. *Bulletin of Volcanology*, 71(10), pp.1149–1158.
Fioletov, V.E. et al., 2016. A global catalogue of large SO 2 sources and emissions derived from the Ozone Monitoring Instrument. *Atmospheric Chemistry and Physics*, 16(18),

p.11497.
Fiorani, L. et al., 2016. Early detection of volcanic hazard by lidar measurement of carbon dioxide. *Natural Hazards*, 83(1), pp.21–29.
Fiorani, L., 2010. Lidar application to litosphere, hydrosphere and atmosphere. *Progress in Laser and Electro-Optics Research*, pp.21–75.
Fiorani, L. et al., 2015. Lidar detection of carbon dioxide in volcanic plumes. In *Third International Conference on Remote Sensing and Geoinformation of the Environment (RSCy2015)*. International Society for Optics and Photonics, p. 95350N.
Fiorani, L. et al., 2011. LIDAR MONITORING OF ANTHROPOGENIC POLLUTION AND NATURAL PHENOMENA. *Environmental Engineering & Management Journal (EEMJ)*, 10(1).
Fiorani, L., Colao, F. & Palucci, A., 2009. Measurement of Mount Etna plume by CO 2-laser-based lidar. *Optics letters*, 34(6), pp.800–802.
Fischer, T.P. & Chiodini, G., 2015. Chapter 45 - Volcanic, Magmatic and Hydrothermal Gases A2 - Sigurdsson, Haraldur BT - The Encyclopedia of Volcanoes (Second Edition). In Amsterdam: Academic Press, pp. 779–797. Available at: https://www.sciencedirect.com/science/article/pii/B9780123859389000456.
Flower, V.J.B. & Carn, S.A., 2015. Characterising volcanic cycles at Soufriere Hills Volcano, Montserrat: Time series analysis of multi-parameter satellite data. *Journal of Volcanology and Geothermal Research*, 304(February), pp.82–93. Available at: http://dx.doi.org/10.1016/j.jvolgeores.2015.07.035.
Flower, V.J.B., Oommen, T. & Carn, S.A., 2016. Improving global detection of volcanic eruptions using the Ozone Monitoring Instrument (OMI). *Atmospheric Measurement Techniques*, 9(11), p.5487.
Galle, B. et al., 2003. A miniaturised ultraviolet spectrometer for remote sensing of SO2 fluxes: A new tool for volcano surveillance. *Journal of Volcanology and Geothermal Research*, 119(1–4), pp.241–254.
Galle, B. et al., 2010. Network for Observation of Volcanic and Atmospheric Change (NOVAC)—A global network for volcanic gas monitoring: Network layout and instrument description. *Journal of Geophysical Research: Atmospheres*, 115(D5).
Gambino, S. et al., 2016. The unusual 28 December 2014 dike-fed paroxysm at Mount Etna: Timing and mechanism from a multidisciplinary perspective. *Journal of Geophysical Research: Solid Earth*, 121(3), pp.2037–2053. Available at: http://dx.doi.org/10.1002/2015JB012379.
Ghisetti, F. & Vezzani, L., 1984. Thin-skinned deformations of the western Sicily thrust belt and relationships with crustal shortening; mesostructural data on the Mt. Kumeta-Alcantara fault zone and related structures. *Bollettino della Societa Geologica Italiana*, 103(1), pp.129–157.
Giacomoni, P.P. et al., 2012. A common feeding system of the NE and S rifts as revealed by the bilateral 2002/2003 eruptive event at Mt. Etna (Sicily, Italy). *Bulletin of volcanology*, 74(10), pp.2415–2433.
Gillot, P.-Y., Lefèvre, J.-C. & Nativel, P.-E., 1994. Model for the structural evolution of the volcanoes of Réunion Island. *Earth and Planetary Science Letters*, 122(3–4), pp.291–302.
Gonnermann, H.M. & Manga, M., 2012. Dynamics of magma ascent in the volcanic conduit. *Modeling Volcanic Processes: The Physics and Mathematics of Volcanism*, pp.55–84.
Harris, A. et al., 2011. Thirty years of satellite-derived lava discharge rates at Etna: Implications for steady volumetric output. *Journal of Geophysical Research: Solid Earth*, 116(B8).
Harris, A. & Ripepe, M., 2007. Synergy of multiple geophysical approaches to unravel

explosive eruption conduit and source dynamics - A case study from Stromboli. *Chemie der Erde - Geochemistry*, 67(1), pp.1–35.

Harris, A.J.L. et al., 1998. Calculation of lava effusion rates from Landsat TM data. *Bulletin of Volcanology*, 60(1), pp.52–71.

Harris, A.J.L. & Baloga, S.M., 2009. Lava discharge rates from satellite-measured heat flux. *Geophysical Research Letters*, 36(19).

Harris, A.J.L. & Neri, M., 2002. Volumetric observations during paroxysmal eruptions at Mount Etna: Pressurized drainage of a shallow chamber or pulsed supply? *Journal of Volcanology and Geothermal Research*, 116(1–2), pp.79–95.

Hidalgo, S. et al., 2015. SO<inf>2</inf> degassing at Tungurahua volcano (Ecuador) between 2007 and 2013: Transition from continuous to episodic activity. *Journal of Volcanology and Geothermal Research*, 298, pp.1–14. Available at: http://dx.doi.org/10.1016/j.jvolgeores.2015.03.022.

Hoff, R.M., 1992. Differential SO2 column measurements of the Mt. Pinatubo volcanic plume. *Geophysical research letters*, 19(2), pp.175–178.

Holland, A.S.P. et al., 2011. Degassing processes during lava dome growth: Insights from Santiaguito lava dome, Guatemala. *Journal of Volcanology and Geothermal Research*, 202(1–2), pp.153–166. Available at: http://dx.doi.org/10.1016/j.jvolgeores.2011.02.004.

Houghton, B.F. et al., 2004. The influence of conduit processes on changes in style of basaltic Plinian eruptions: Tarawera 1886 and Etna 122 BC. *Journal of Volcanology and Geothermal Research*, 137(1–3 SPEC. ISS.), pp.1–14.

Kahl, M. et al., 2015. Constraints on the nature and evolution of the magma plumbing system of Mt. Etna volcano (1991-2008) from a combined thermodynamic and kinetic modelling of the compositional record of minerals. *Journal of Petrology*, 56(10), pp.2025–2068.

Kantzas, E.P. et al., 2010. Protocols for UV camera volcanic SO2 measurements. *Journal of Volcanology and Geothermal Research*, 194(1–3), pp.55–60. Available at: http://dx.doi.org/10.1016/j.jvolgeores.2010.05.003.

Kazahaya, R. et al., 2016. Pre-eruptive inflation caused by gas accumulation: Insight from detailed gas flux variation at Sakurajima volcano, Japan. *Geophysical Research Letters*, 43(21), p.11,219-11,225.

Kazahaya, R. et al., 2011. Relation between single very-long-period pulses and volcanic gas emissions at Mt. Asama, Japan. *Geophysical Research Letters*, 38(11), pp.3–7.

Kern, C. et al., 2015. An SO2 camera system for continuous, real-time monitoring of gas emissions from Kilauea Volcano's Overlook Crater. *Journal of Volcanology and Geothermal Research*, 300(this issue), pp.81–94. Available at: http://dx.doi.org/10.1016/j.jvolgeores.2014.12.004.

Kern, C. et al., 2010. Theoretical description of functionality, applications, and limitations of SO 2 cameras for the remote sensing of volcanic plumes. *Atmospheric Measurement Techniques*, 3(3), pp.733–749.

Lentini, F., 1982. The geology of the Mt. *Etna basement, Mem. Soc. Geol. Ital*, 23, pp.7–25.

Leonardi, S., Gresta, S. & Mulargia, F., 1999. Cross-correlation between volcanic tremor and SO2 flux data from Mount Etna volcano, 1987–1992. *Physics and Chemistry of the Earth, Part A: Solid Earth and Geodesy*, 25(9–11), pp.737–740.

Levelt, P. et al., 2017. The Ozone Monitoring Instrument: Overview of twelve years in space. *Atmos. Chem. Phys. Discuss.*, 2017, pp.1–61. Available at: https://www.atmos-chem-phys-discuss.net/acp-2017-487/.

Levelt, P.F. et al., 2006. The ozone monitoring instrument. *IEEE Transactions on Geoscience and Remote Sensing*, 44(5), pp.1093–1101.

Li, C. et al., 2017. New-generation NASA Aura Ozone Monitoring Instrument (OMI) volcanic SO2 dataset: Algorithm description, initial results, and continuation with the Suomi-NPP Ozone Mapping and Profiler Suite (OMPS). *Atmospheric Measurement Techniques*, 10(2), pp.445–458.

Lopez, T. et al., 2013. Evaluation of Redoubt Volcano's sulfur dioxide emissions by the Ozone Monitoring Instrument. *Journal of Volcanology and Geothermal Research*, 259, pp.290–307.

Lubcke, P. et al., 2013. On the absolute calibration of SO 2 cameras. *Atmos. Meas. Tech*, 6(May), pp.677–696. Available at: www.atmos-meas-tech.net/6/677/2013/.

Lucas, B.D. & Kanade, T., 1981. An iterative image registration technique with an application to stereo vision. *Proceedings of the 7th International Joint Conference on Artificial Intelligence (IJCAI)*, 2, pp.674–679. Available at: http://www.ri.cmu.edu/pub_files/pub3/lucas_bruce_d_1981_1/lucas_bruce_d_1981_1.ps.gz.

Malinconico, L.L., 1979. Fluctuations in SO2 emission during recent eruptions of Etna. *Nature*, 278, pp.43–45.

Marchetti, E. et al., 2009. Infrasonic evidences for branched conduit dynamics at Mt. Etna volcano, Italy. *Geophysical Research Letters*, 36(19).

McCormick, B. et al., 2015. Ten years of satellite observations reveal highly variable sulphur dioxide emissions at Anatahan Volcano, Mariana Islands. *Journal of Geophysical Research*, 120(14), pp.7258–7282.

McCormick, B.T. et al., 2012. First synoptic analysis of volcanic degassing in Papua New Guinea. *Geochemistry, Geophysics, Geosystems*, 13(3), pp.1–21.

Mcgonigle, A.J.S. et al., 2017. Ultraviolet Imaging of Volcanic Plumes : A New Paradigm in Volcanology. , pp.1–14.

McGonigle, A.J.S., 2007. Measurement of volcanic SO2 fluxes with differential optical absorption spectroscopy. *Journal of Volcanology and Geothermal Research*, 162(3–4), pp.111–122.

McGonigle, A.J.S. et al., 2009. Spectroscopic capture of 1 Hz volcanic SO2 fluxes and integration with volcano geophysical data. *Geophysical Research Letters*, 36(21), pp.1–5.

McGonigle, A.J.S. et al., 2008. Unmanned aerial vehicle measurements of volcanic carbon dioxide fluxes. *Geophysical Research Letters*, 35(6), pp.3–6.

McGonigle, A.J.S. & Oppenheimer, C., 2003. Optical sensing of volcanic gas and aerosol emissions. *Geological Society, London, Special Publications*, 213(1), pp.149–168.

McGonigle, a. J.S. et al., 2005. Plume velocity determination for volcanic SO2 flux measurements. *Geophysical Research Letters*, 32(11), pp.1–4.

Métrich, N. et al., 2004. 2001 flank eruption of the alkali-and volatile-rich primitive basalt responsible for Mount Etna's evolution in the last three decades. *Earth and Planetary Science Letters*, 228(1), pp.1–17.

Métrich, N. & Mandeville, C.W., 2010. Sulfur in Magmas. *Elements*, 6(2), pp.81–86. Available at: http://dx.doi.org/10.2113/gselements.6.2.81.

Moffat, A.J. & Millan, M.M., 1971. The applications of optical correlation techniques to the remote sensing of SO2 plumes using sky light. *Atmospheric Environment (1967)*, 5(8), pp.677–690.

Moretti, R. & Papale, P., 2004. On the oxidation state and volatile behavior in multicomponent gas–melt equilibria. *Chemical Geology*, 213(1–3), pp.265–280.

Mori, T. et al., 2013. Time-averaged SO<inf>2</inf> fluxes of subduction-zone volcanoes: Example of a 32-year exhaustive survey for Japanese volcanoes. *Journal of Geophysical Research Atmospheres*, 118(15), pp.8662–8674.

Mori, T. & Burton, M., 2009. Quantification of the gas mass emitted during single

explosions on Stromboli with the SO2 imaging camera. *Journal of Volcanology and Geothermal Research*, 188(4), pp.395–400. Available at: http://dx.doi.org/10.1016/j.jvolgeores.2009.10.005.

Mori, T. & Burton, M., 2006. The SO2 camera: A simple, fast and cheap method for ground-based imaging of SO2 in volcanic plumes. *Geophysical Research Letters*, 33(24), pp.1–5.

Nadeau, P.A. et al., 2015. Using SO2 camera imagery and seismicity to examine degassing and gas accumulation at Kīlauea Volcano, May 2010. *Journal of Volcanology and Geothermal Research*, 300, pp.70–80. Available at: http://dx.doi.org/10.1016/j.jvolgeores.2014.12.005.

Nadeau, P.A., Palma, J.L. & Waite, G.P., 2011. Linking volcanic tremor, degassing, and eruption dynamics via SO <inf>2</inf> imaging. *Geophysical Research Letters*, 38(1), pp.1–5.

Neri, M. et al., 2017. Topographic Maps of Mount Etna's Summit Craters, updated to December 2015. *Journal of Maps*, 13(2), pp.674–683. Available at: https://www.tandfonline.com/doi/full/10.1080/17445647.2017.1352041.

Oppenheimer, C., 2003. Climatic, environmental and human consequences of the largest known historic eruption: Tambora volcano (Indonesia) 1815. *Progress in physical geography*, 27(2), pp.230–259.

Oppenheimer, C. et al., 1998. Remote measurement of volcanic gases by Fourier transform infrared spectroscopy. *Applied Physics B: Lasers and Optics*, 67(4), pp.505–515.

Oppenheimer, C., 2010. Ultraviolet sensing of volcanic sulfur emissions. *Elements*, 6(2), pp.87–92.

Oppenheimer, C., Fischer, T.P. & Scaillet, B., 2014. Volcanic degassing: process and impact.

Oppenheimer, C., Scaillet, B. & Martin, R.S., 2011. Sulfur Degassing From Volcanoes: Source Conditions, Surveillance, Plume Chemistry and Earth System Impacts. *Reviews in Mineralogy and Geochemistry*, 73(1), pp.363–421.

Palma, J.L., 2013. Wind reanalysis. *https://vhub.org/resources/windre.*

Parfitt, E.A., 2004. A discussion of the mechanisms of explosive basaltic eruptions. *Journal of Volcanology and Geothermal Research*, 134(1–2), pp.77–107.

Patanè, D. et al., 2013. Insights into magma and fluid transfer at Mount Etna by a multiparametric approach: A model of the events leading to the 2011 eruptive cycle. *Journal of Geophysical Research: Solid Earth*, 118(7), pp.3519–3539.

Pérez, W. et al., 2009. The Masaya Triple Layer: A 2100 year old basaltic multi-episodic Plinian eruption from the Masaya Caldera Complex (Nicaragua). *Journal of Volcanology and Geothermal Research*, 179(3–4), pp.191–205. Available at: http://dx.doi.org/10.1016/j.jvolgeores.2008.10.015.

Pering, T.D., Tamburello, G., McGonigle, a. J.S., Hanna, E., et al., 2014. Correlation of oscillatory behaviour in Matlab using wavelets. *Computers and Geosciences*, 70(August 2015), pp.206–212.

Pering, T.D. et al., 2015. Dynamics of mild strombolian activity on Mt. Etna. *Journal of Volcanology and Geothermal Research*, 300, pp.103–111. Available at: http://linkinghub.elsevier.com/retrieve/pii/S0377027314003874.

Pering, T.D., Tamburello, G., McGonigle, a. J.S., Aiuppa, a., et al., 2014. High time resolution fluctuations in volcanic carbon dioxide degassing from Mount Etna. *Journal of Volcanology and Geothermal Research*, 270, pp.115–121. Available at: http://dx.doi.org/10.1016/j.jvolgeores.2013.11.014.

Peters, N. et al., 2015. Use of motion estimation algorithms for improved flux measurements using SO2 cameras. *Journal of Volcanology and Geothermal Research*, 300, pp.58–69. Available at:

http://dx.doi.org/10.1016/j.jvolgeores.2014.08.031.
Platt, U. et al., 2015. Quantitative imaging of volcanic plumes - Results, needs, and future trends. *Journal of Volcanology and Geothermal Research*, 300, pp.7–21. Available at: http://dx.doi.org/10.1016/j.jvolgeores.2014.10.006.
Polacci, M., Corsaro, R.A. & Andronico, D., 2006. Coupled textural and compositional characterization of basaltic scoria: Insights into the transition from Strombolian to fire fountain activity at Mount Etna, Italy. *Geology*, 34(3), pp.201–204. Available at: http://dx.doi.org/10.1130/G22318.1.
Pompilio, M. et al., 2017. Magma dynamics within a basaltic conduit revealed by textural and compositional features of erupted ash: the December 2015 Mt. Etna paroxysms. *Scientific Reports*, 7(1), p.4805. Available at: http://www.nature.com/articles/s41598-017-05065-x.
Queiβer, M., Granieri, D. & Burton, M., 2016. A new frontier in CO 2 flux measurements using a highly portable DIAL laser system. *Scientific reports*, 6, p.33834.
Rasà, R. et al., 1993. Etna: sistema di alimentazione profondo, assetto geostatico locale e bimodalità di funzionamento del vulcano. *Progetto-Etna*, 1995, pp.145–150.
Ripepe, M., Marchetti, E. & Ulivieri, G., 2007. Infrasonic monitoring at Stromboli volcano during the 2003 effusive eruption: Insights on the explosive and degassing process of an open conduit system. *Journal of Geophysical Research: Solid Earth*, 112(B9).
Roggensack, K. et al., 1997. Explosive Basaltic Volcanism from Cerro Negro Volcano: Influence of Volatiles on Eruptive Style. *Science*, 277(5332), p.1639 LP-1642. Available at: http://science.sciencemag.org/content/277/5332/1639.abstract.
Rose, W.I. et al., 2013. Open-vent volcanism and related hazards: Overview. In W. I. Rose et al., eds. *Understanding Open-Vent Volcanism and Related Hazards*. Geological Society of America. Available at: https://doi.org/10.1130/2013.2498(00).
Rothery, D.A., Coppola, D. & Saunders, C., 2005. Analysis of volcanic activity patterns using MODIS thermal alerts. *Bulletin of Volcanology*, 67(6), pp.539–556. Available at: https://doi.org/10.1007/s00445-004-0393-3.
Saccorotti, G., Iguchi, M. & Aiuppa, A., 2015. In situ Volcano monitoring: present and future. *Volcanic Hazards, Risks and Disasters; Elsevier: Amsterdam, The Netherlands*, pp.169–202.
Salerno, G.G. et al., 2009. Three-years of SO2 flux measurements of Mt. Etna using an automated UV scanner array: Comparison with conventional traverses and uncertainties in flux retrieval. *Journal of Volcanology and Geothermal Research*, 183(1–2), pp.76–83. Available at: http://dx.doi.org/10.1016/j.jvolgeores.2009.02.013.
Sawyer, G.M. & Burton, M.R., 2006. Effects of a volcanic plume on thermal imaging data. *Geophysical Research Letters*, 33(14).
Sciotto, M. et al., 2013. Seismic and infrasound signals at Mt. Etna: Modeling the North-East crater conduit and its relation with the 2008–2009 eruption feeding system. *Journal of volcanology and geothermal research*, 254, pp.53–68.
Scollo, S. et al., 2012. MISR observations of Etna volcanic plumes. *Journal of Geophysical Research Atmospheres*, 117(6), pp.1–13.
Shinohara, H., 2013. Volatile flux from subduction zone volcanoes: Insights from a detailed evaluation of the fluxes from volcanoes in japan. *Journal of Volcanology and Geothermal Research*, 268, pp.46–63. Available at: http://dx.doi.org/10.1016/j.jvolgeores.2013.10.007.
Siebert, L., Simkin, T. & Kimberly, P., 2010. *Volcanoes of the World: Third Edition*, University of California Press. Available at: https://books.google.it/books?id=0DZrfpL9_DMC.
Spampinato, L. et al., 2015a. Multiparametric study of the February-April 2013 paroxysmal phase of Mt. Etna New South-East crater. *Geochemistry, Geophysics,*

Geosystems, (April 2013), pp.1932–1949.
Spampinato, L. et al., 2015b. Multiparametric study of the February-April 2013 paroxysmal phase of Mt. Etna New South-East crater. *Geochemistry, Geophysics, Geosystems*, (April 2013).
Spilliaert, N. et al., 2006. Melt inclusion record of the conditions of ascent, degassing, and extrusion of volatile-rich alkali basalt during the powerful 2002 flank eruption of Mount Etna (Italy). *Journal of Geophysical Research: Solid Earth*, 111(B4).
La Spina, A. et al., 2015. Open-path FTIR spectroscopy of magma degassing processes during eight lava fountains on Mount Etna. *Earth and Planetary Science Letters*, 413, pp.123–134. Available at: http://dx.doi.org/10.1016/j.epsl.2014.12.038.
La Spina, A., Burton, M. & Salerno, G.G., 2010. Unravelling the processes controlling gas emissions from the central and northeast craters of Mt. Etna. *Journal of Volcanology and Geothermal Research*, 198(3–4), pp.368–376. Available at: http://dx.doi.org/10.1016/j.jvolgeores.2010.09.018.
Stoiber, R.E., Malinconico, L.L. & Williams, S.N., 1983. Use of the correlation spectrometer at volcanoes, Forecasting Volcanic Events H. Tazieff, JC Sabroux, 425–444.
Tamburello, G. et al., 2012. Passive vs. active degassing modes at an open-vent volcano (Stromboli, Italy). *Earth and Planetary Science Letters*, pp.106–116.
Tamburello, G. et al., 2013. Periodic volcanic degassing behavior: The Mount Etna example. *Geophysical Research Letters*, 40(18), pp.4818–4822.
Tamburello, G. et al., 2011. Recent advances in ground-based ultraviolet remote sensing of volcanic SO2 fluxes. *Annals of Geophysics*, 54(2), pp.199–208.
Tamburello, G. et al., 2011. UV camera measurements of fumarole field degassing (La Fossa crater, Vulcano Island). *Journal of Volcanology and Geothermal Research*, 199(1–2), pp.47–52. Available at: http://dx.doi.org/10.1016/j.jvolgeores.2010.10.004.
Tanguy, J.-C., Condomines, M. & Kieffer, G., 1997. Evolution of the Mount Etna magma: constraints on the present feeding system and eruptive mechanism. *Journal of Volcanology and Geothermal research*, 75(3), pp.221–250.
Tric, E. et al., 1994. Absolute paleointensities between 60 and 160 kyear BP from Mount Etna (Sicily). *Physics of the earth and planetary interiors*, 85(1–2), pp.113–129.
Vandaele, A.C. et al., 1994. SO2 absorption cross section measurement in the UV using a Fourier transform spectrometer. *Journal of Geophysical Research: Atmospheres*, 99(D12), pp.25599–25605.
Vergniolle, S. & Ripepe, M., 2008. From Strombolian explosions to fire fountains at Etna Volcano (Italy): what do we learn from acoustic measurements? *Geological Society, London, Special Publications*, 307(1), p.103 LP-124. Available at: http://sp.lyellcollection.org/content/307/1/103.abstract.
Vulpiani, G., Ripepe, M. & Valade, S., 2016. Mass discharge rate retrieval combining weather radar and thermal camera observations. *Journal of Geophysical Research: Solid Earth*, 121(8), pp.5679–5695.
Waite, G.P., Nadeau, P.A. & Lyons, J.J., 2013. Variability in eruption style and associated very long period events at Fuego volcano, Guatemala. *Journal of Geophysical Research: Solid Earth*, 118(4), pp.1526–1533.
Wallace, P.J. et al., 2015. Chapter 7 - Volatiles in Magmas A2 - Sigurdsson, Haraldur BT - The Encyclopedia of Volcanoes (Second Edition). In Amsterdam: Academic Press, pp. 163–183. Available at: https://www.sciencedirect.com/science/article/pii/B9780123859389000079.
Wallace, P.J., 2001. Volcanic SO2 emissions and the abundance and distribution of exsolved gas in magma bodies. *Journal of Volcanology and Geothermal Research*, 108(1–4), pp.85–106.

Wang, X. et al., 2008. Volcanic dust characterization by EARLINET during Etna's eruptions in 2001–2002. *Atmospheric environment*, 42(5), pp.893–905.

Werner, C. et al., 2017. Magmatic degassing, lava dome extrusion, and explosions from Mount Cleveland volcano, Alaska, 2011–2015: Insight into the continuous nature of volcanic activity over multi-year timescales. *Journal of Volcanology and Geothermal Research*, 337, pp.98–110.

Wilkes, T. et al., 2017. A Low-Cost Smartphone Sensor-Based UV Camera for Volcanic SO2 Emission Measurements. *Remote Sensing*, 9(1), p.27. Available at: http://www.mdpi.com/2072-4292/9/1/27.

Williams-Jones, G. et al., 2000. A model of diffuse degassing at three subduction-related volcanoes. *Bulletin of Volcanology*, 62(2), pp.130–142.

Williams, S.N. & Self, S., 1983. The October 1902 plinian eruption of Santa Maria volcano, Guatemala. *Journal of Volcanology and Geothermal Research*, 16(1), pp.33–56. Available at: http://www.sciencedirect.com/science/article/pii/0377027383900835.

Wooster, M.J., Zhukov, B. & Oertel, D., 2003. Fire radiative energy for quantitative study of biomass burning: derivation from the BIRD experimental satellite and comparison to MODIS fire products. *Remote Sensing of Environment*, 86(1), pp.83–107.

Wright, R. et al., 2002. Automated volcanic eruption detection using MODIS. *Remote sensing of environment*, 82(1), pp.135–155.

Wright, R. & Flynn, L.P., 2004. Space-based estimate of the volcanic heat flux into the atmosphere during 2001 and 2002. *Geology*, 32(3), pp.189–192. Available at: http://dx.doi.org/10.1130/G20239.1.

Wright, R., Flynn, L.P. & Harris, A.J., 2001. Evolution of lava flow-fields at Mount Etna, 27–28 October 1999, observed by Landsat 7 ETM+. *Bulletin of Volcanology*, 63(1), pp.1–7.

Wright, R. & Pilger, E., 2008. Satellite observations reveal little inter-annual variability in the radiant flux from the Mount Erebus lava lake. *Journal of Volcanology and Geothermal Research*, 177(3), pp.687–694. Available at: http://dx.doi.org/10.1016/j.jvolgeores.2008.03.005.

Zuccarello, L. et al., 2013. The coupling between very long period seismic events, volcanic tremor, and degassing rates at Mount Etna volcano. *Journal of Geophysical Research: Solid Earth*, 118(9), pp.4910–4921.

Acknowledgments

I wish to thank the LabVulc Team Marcello Bitetto, Dario Delle Donne, Giancarlo Tamburello and Angelo Battaglia for all support given to me during these years of research. The teamwork was fundamental in the development of the scientific instruments and in the volcanoes fieldworks, the exchange of different scientific background has undoubtedly enriched the knowledge of each of us, much improving our point of view in the problem solving of every issue, both scientific and technical.

I wish to thank my supervisor, Prof. Alessandro Aiuppa, for his wise advices given to me during these years of studies, that with no doubt were fundamental to my scientific growth, and also thank for his patience for my countless delays.

I wish to thank E. Privitera (Director of INGV-OE) and the INGV-OE staff, Mauro Coltelli, Emilio Pecora, Filippo Greco and Filippo Murè for support to installation and maintenance of the UV3 camera system. The INGV-OE "Unità Funzionale Sismologia" is particularly acknowledged for providing seismic tremor data. Ente Parco dell'Etna is acknowledged for granting access to the volcano summit.

I wish to thank the reviewers of this PhD thesis, Diego Coppola and Andrew McGonigle for their comments that greatly improved this manuscript.